Investigations of high voltage plasma boundary sheaths in radio-frequency discharges operated with multiple frequencies

A thesis for the degree of

PHILOSOPHIAE DOCTOR

Presented to

DUBLIN CITY UNIVERSITY

By

DEBORAH O'CONNELL

School of Physical Sciences
Dublin City University

Research Supervisors:
Prof. Miles M. Turner and
Dr. Albert R. Ellingboe

External Examiner: Prof. Jürgen Meichsner
Internal Examiner: Prof. Eugene Kennedy

July 2004

Declaration

I hereby certify that this material which I now submit for assessment on the programme of study leading to the award of Philosophiae Doctor is entirely my own work and has not been taken from the work of others save and to the extent that such work has been cited and acknowledged within the text of this work.

Deborah O'Connell

Deborah O'Connell, July 2004

To my parents

Acknowledgements

A thesis is never solely an individual effort. I wish to thank the following people

- Firstly, I would like to thank Prof. Jürgen Meichsner and Prof. Eugene Kennedy for examining the thesis.
- Prof. Miles Turner, Dr. David Vender and Dr. Bert Ellingboe for giving me the opportunity to carry out my project in the Plasma Research Laboratory (PRL) and for supervision of the project. Particularly, Miles for collaborating in the simulation comparisons.
- Dr. Roberto Zorat for his invaluable contribution to my project in adapting the simulation code to the experiment; for his readiness to help even after he finished and returned to Italy.
- Dr. Timo Gans for the interest and enthusiasm he took in my project during his stay in PRL; for the important, insightful discussions in particular during the collaboration at the Ruhr University Bochum.
- Dr. Thomas Schwarz-Selinger, from the Max-Planck Institute for Plasma Physics, Garching, for his extremely helpful visit to PRL and also during the collaboration at the Ruhr University Bochum.
- Prof. Uwe Czarnetzki and Dr. Mariana Osiac for the interesting collaboration at the Ruhr University Bochum.
- Damien Kellett and Bernard Stobie for the excellent technical support, in particular during the excitment towards the end.
- Samantha Fahy, Sarah Hayes and Deirdre O'Riordan for their valuable support throughout.
- Dr. Paul Swift and the other members of PRL who contributed to my project over the years.
- Most importantly, my parents Eileen and Aidan, brother Sean and sister Kara, for their enormous support and encouragement throughout; a special thanks to Aidan for encouraging an interest in physics from an early age.

Contents

CONTENTS

Abstract

The complex nature of multi frequency high voltage rf plasma boundary sheaths is experimentally investigated. A mass resolved ion energy analyser is incorporated into the grounded electrode of a confined symmetric capacitively coupled rf discharge, operated either in single or dual frequency mode. Inherent difficulties in measuring ion energy distribution functions (IEDFs) are minimised by a procedure based on simulations of ion trajectories and extensive experimental checks. A novel simple calibration method for determining absolute ion fluxes is developed.

Discharges in hydrogen, deuterium and mixtures of both are investigated. The relatively light hydrogen ions respond to temporal variations in the sheath potential at typical technologically used radio-frequencies (e.g. 13.56 MHz), allowing for detailed investigations of the sheath dynamics. Hydrogen is also well suited for comparison to simulations. It is the simplest molecular gas with the most extensive data set for collisional cross-sections.

Experimental results of absolute ion fluxes and IEDFs are compared to 2D-PIC simulations perfectly adapted to the experimental conditions. The agreement is in general excellent. Simulations yield deeper insight into the sheath dynamics and sheath chemistry. The simulations can also be used under conditions which are difficult or impossible experimentally.

Details of the sheath dynamics and the sheath chemistry of the investigated discharges are well understood. Structures in the IEDFs caused by the complex dynamics of dual frequency sheaths can be explained and reproduced using a simple analytical model. The basic concept of separate control of ion flux and ion energy in dual frequency discharges is observed. However, the IEDFs of light ions are quite broad. This limits control and selectivity in technological processes. The concept works better for heavier ions, since the IEDFs are narrower due to more averaging over the sheath dynamics.

Time resolved investigations in the afterglow of a pulsed mode plasma, reveal that the positive space charge sheath does not fully collapse in the post discharge. This can be attributed to electron heating by vibrationally excited molecules in the afterglow.

CHAPTER 1

General introduction

Recent decades have seen a growing interest in the scientific fundamentals and innovative technical applications of low-temperature plasmas [1, 2, 3]. The unique properties of plasmas are the basis of a multitude of industrial processes, as diverse as semiconductor device manufacturing, textile, optics, lighting, aerospace, biomedical engineering and nano-technology. With progressively new plasma based technologies coming to the frontier, there is a requirement for flexible and intelligent systems for tailoring the plasma to specific technical needs. There is a desire to manipulate plasma properties easily and independently. Most plasma technologies are based on surface treatments. Fundamental understanding and tighter control of plasma surface interactions would be of enormous benefit to all technical applications of low-temperature plasmas.

The surface processes in plasmas are mainly influenced by the following factors: reactive particles approaching the surface, the ion flux onto the substrate and the ion energy distribution function (IEDF). Reactive particles approaching the surface are mainly determined by plasma chemistry. The electron energy distribution function (EEDF) drives the plasma chemistry and can be controlled

by the discharge design e.g. combinations of capacitively coupled radio frequency (CCRF) discharges and inductively coupled rf plasmas (ICP) [1, 4]. Another approach to control the EEDF, is to pulse or modulate the power input. Ion flux onto the substrate is mainly governed by the ion density. The power coupled into the plasma controls the ion density and thus, the flux onto the surface. The IEDF and impact energy of ions striking the substrate is a crucial parameter, vital for understanding and further developing the techniques used in surface processes. The type of ions and their impact energy onto the electrode surface is dependent on properties of the boundary sheath - the interface between the plasma bulk and the surface. The ability to manipulate ion transport in the sheath and thus tailor the IEDF is highly desirable.

The sheath characteristics determine important aspects of the plasma-surface interaction. RF sheaths are of particular importance for the treatment of insulators and semiconductors. However, rf sheath dynamics is complex and despite its importance, not well understood. The properties of sheaths have been extensively studied theoretically in the limit of collisionless particle dynamics [5, 6]. However, there is especially a lack of experimental studies. The main focus of this work is to gain deeper fundamental understanding of rf sheath dynamics, in particular for multi-frequency rf sheaths.

The shape of the IEDF at the electrode surface provides important information about ion formation within the plasma, ion interaction within the sheath and the sheath dynamics. To investigate rf sheath dynamics at a high voltage boundary sheath, a confined capacitively coupled rf discharge has been designed. This allows for measurements of IEDFs at a grounded electrode using a mass resolved ion energy analyser. Measurements are performed in hydrogen. Apart from the technological importance of hydrogen containing discharges, hydrogen acts as the perfect discharge gas for fundamental investigations because of two main reasons. Firstly, at typical technologically used radio-frequencies (e.g. 13.56 MHz), the relatively light hydrogen ions respond best to the time dependence of the sheath potential, allowing for detailed investigations of the sheath dynam-

ics. Secondly, hydrogen is the simplest molecular gas with the most extensive data set for collisional cross-sections, making it suitable for comparison to simulations. The experimental results are compared to 2D-particle-in-cell (2D-PIC) simulations. Special efforts are made to perfectly adapt both the experiment and simulations for direct comparison to each other. The accurate adaptation allows the experiment to benchmark the PIC simulation, which can then be used for further detailed investigations that are difficult or impossible experimentally.

1.1 RF discharges

An important characteristic of low temperature plasmas is that the charged particles and neutrals are not in thermodynamic equilibrium [7]. The electron temperature, T_e ($\approx 1-4\,eV$), greatly exceeds the ion and neutral gas temperatures, T_i and T_g ($\approx 0.05\,eV$). This arises from the fact that transfer of energy from electrons to heavy particles is rather inefficient, since the energy transfer depends on the mass ratio of the colliding species. This key property of plasmas has the facility to produce a chemical environment, characterized by a high temperature, without inducing corresponding physical damage to an object immersed in the plasma. The clever use of this non-equilibrium property of plasmas forms the basis of most applications. In particular rf discharges are frequently used in processing applications. An important advantage of rf discharges over dc discharges is that a dielectric on an electrode only acts as an additional coupling capacitor, thus allowing for plasma treatment of insulators and semiconductors [8].

Discharges in processing technology are mainly driven at 13.56 MHz. This frequency and its higher harmonics are allowed by international telecommunication laws. At these frequencies electrons oscillate in the rf electric field while the heavier, less mobile, ions cannot follow the time varying field and respond to a time-averaged field.

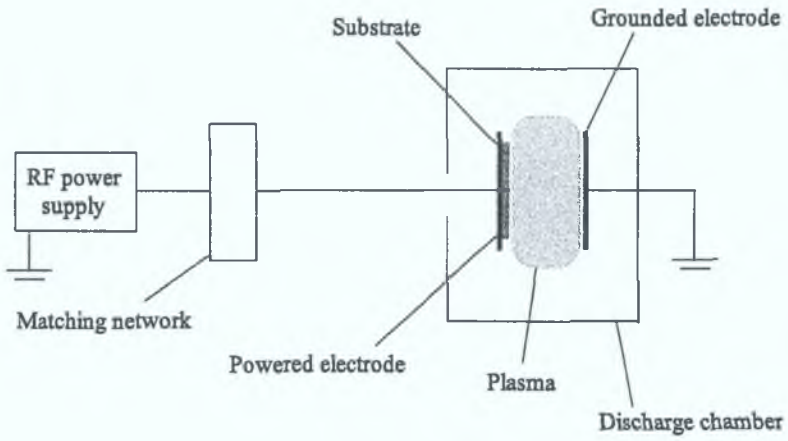

Figure 1.1: *Typical CCRF discharge set-up*

1.1.1 Capacitively coupled rf discharges

The most commonly used plasma reactor is the capacitively coupled radio frequency discharge (CCRF). CCRF discharges are extensively discussed in the literature, e.g. [1, 3, 9]. Nevertheless, for better understanding of the following chapters, some characteristics are briefly discussed here. A typical set-up of a CCRF discharge is shown in figure 1.1. The most commonly used arrangement is the parallel plate reactor with one electrode grounded and the other powered. The electrodes are usually in direct contact with the plasma and are often cooled. The powered electrode is usually driven with a high frequency sinusoidal voltage. A matching network matches the impedance of the discharge to the output impedance of the rf power supply. This provides most efficient power coupling into the discharge. The matching network typically includes a blocking capacitor providing dc isolation between the driven electrode and the rf power supply.

The random electron flux is much higher than that of the ions, due to the higher mobility of electrons than ions. Therefore more electrons than ions will initially be absorbed by the electrode. This leads to a positive space charge region between the plasma and electrode, breaking quasi neutrality in the vicinity of the electrode. The corresponding electric field repels electrons and accelerates ions towards the electrode. Under steady state conditions the electron flux balances

the ion flux [2]. In the sheaths positive ions gain energy, through acceleration by the sheath electric field, corresponding to the potential difference between the plasma and electrode. This ion bombardment of the electrode is of enormous interest for technological applications. In combination with chemical reactions it allows for complex treatment of materials placed on the electrodes. The most popular process is plasma based etching in the microchip production.

In the case of a symmetric discharge, the electrode areas are equal. This results in an equal rf voltage drop across both electrode sheaths, therefore equal ion bombardment of both electrodes. However, the ion bombardment at the electrode can be strongly enhanced in asymmetric discharge geometries with unequal electrode areas. The voltage drop at the smaller electrode is greater than the voltage drop at the larger electrode [10]. Hence ion bombardment is more concentrated at the smaller electrode. In practice grounded chamber walls usually result in a larger effective area of the grounded electrode.

The primary limitation of capacitively coupled plasma sources is that the ion flux to the substrate cannot be varied independently of the ion bombardment energy [11]. In order to obtain high ion densities required for processing applications high powers must be employed. However, this results in an increase in the voltage drop across the sheaths and simultaneously raises the ion impact energy at the surface, causing damage to the substrate. These limitations have led to the development of sources where separate mechanisms are used to control the ion flux and the ion impact energy at the substrate [1].

1.1.2 Inductively coupled rf discharges

The rf inductively coupled plasma (ICP) is an electrodless type of discharge [4]. The planar coil configuration [12], figure 7.57, is the most commonly used for material processing. The rf power is coupled into the plasma by means of an induction coil through a dielectric window so that the plasma is not in contact with the antenna. The power coupling mechanism is analogous to a transformer, whereby the antenna acts as the primary coil of the transformer and the plasma

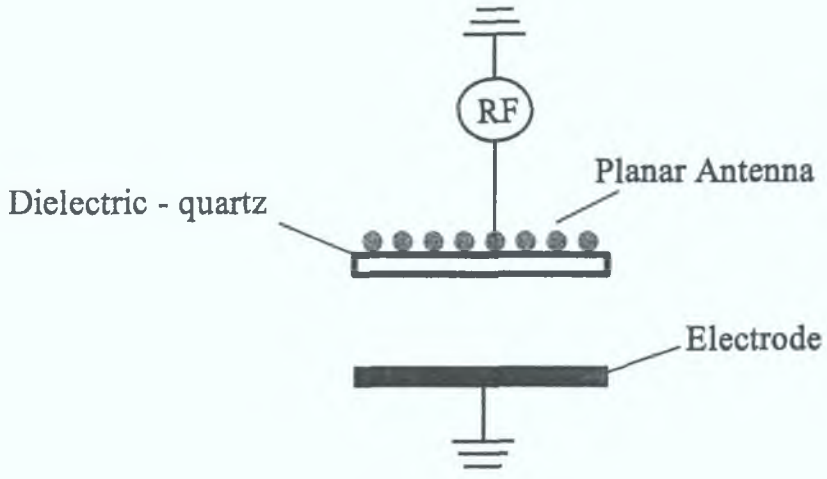

Figure 1.2: *Typical ICP discharge setup*

as the secondary coil. The oscillating currents in the antenna generate a time dependent magnetic field. This time varying magnetic field induces an electric field in the plasma, according to Faraday's law;

$$\nabla \times E = -\mu_0 \frac{\partial H}{\partial t} \tag{1.1}$$

where μ_0 is the permeability of free space, and E and H are the electric and magnetic field vectors respectively.

However, the antenna can also act as an electrode. Therefore both inductive and capacitive power coupling mechanisms can coexist in ICPs. Capacitive coupling drives the discharge at low plasma densities and is referred to as *E-mode*. At higher powers the plasma density is large enough to support the induced currents and a transition to inductive coupling occurs, referred to as *H-mode* [13, 14, 15]. There are several methods of reducing the parasitic capacitance and increasing the inductive coupling to capacitive coupling ratio [16]. Inductively coupled plasmas can achieve higher plasma densities, at lower pressure, than capacitively coupled [1]. Since inductive coupling rather than capacitive coupling transfers power into the plasma low voltages appear across the boundary sheaths [17]. Hence ion acceleration and ion energy at the surfaces is low.

For processing applications a substrate electrode can be introduced into the discharge. The energy of ions bombarding a substrate is determined by the sheath dynamics in front of the surface. By applying an independent bias voltage to the electrode the sheath voltage, in front of the substrate, can be controlled independently of the plasma production [1]. Therefore, the required high densities can be generated by the inductively coupled power and the ion impact energy by the electrode bias voltage.

1.1.3 Dual frequency rf discharges

As explained above in conventional single frequency capacitively coupled devices the ion density and ion energy cannot be independently controlled. In recent years dual frequency devices have been used to obtain an additional degree of flexibility [18, 19, 20, 21, 22, 23]. To a fair approximation the high frequency voltage can be used to control the plasma density, due to more efficient displacement current [24]. The second lower frequency voltage allows control of the sheath voltage, thus controlling the impact energy of the ions onto the electrode.

At low pressures, the ion flux, Γ_i, onto the substrate can be expressed as,

$$\Gamma_i = n_0 u_B \tag{1.2}$$

where n_0 is the plasma density at the plasma sheath boundary and u_B the Bohm velocity.

The impact energy of ions striking the electrode surface is dependent on the sheath potential, the potential ions fall through while traversing the sheath. At low pressures, the mean energy, E_i, of the ions bombarding the surface is approximated by,

$$E_i = eV_s \tag{1.3}$$

where e is the elementary electronic charge and V_s is the time-averaged sheath potential. Thus, if the plasma density and sheath voltage can be controlled separately, the ion flux and the ion impact energy onto the substrate can be

independently controlled.

1.2 Plasma boundary sheath

An important property of the plasma is the formation of the boundary sheath between the plasma and any object with which it comes in contact. The properties of the sheath have predominantly been investigated theoretically [5, 6, 95, 26, 27, 28]. In contrast to the plasma bulk the sheath region exhibits strong electric fields. These electric fields point towards the electrodes and therefore accelerate positively charged particles and repel negatively charged particles. Ions created in the plasma bulk enter into the sheath and gain energy through acceleration by the sheath electric field and lose energy through collisions. Therefore the boundary sheaths determine important aspects of plasma-surface interaction. The impact energy of ions onto the electrode surface is dependent on the sheath characteristics such as sheath potential, sheath thickness, ion-neutral mean free path, and the ion transit time through the sheath [29, 30]. To obtain deeper understanding a simple 1-D model [1] can be used to describe the behaviour of ions and electrons in the sheath. The following conditions and basic assumptions are considered.
The potential, $\Phi = 0$ at the sheath edge.
Energy conservation for ions (collisionless sheath) gives

$$\frac{1}{2}Mu^2(x) = \frac{1}{2}Mu_s^2 - e\Phi(x) \tag{1.4}$$

where M is the mass of ions, u is the drift velocity, u_s is the drift velocity of ions at the plasma sheath boundary, e is the elementary charge, and $\Phi(x)$ is the variation of potential across the sheath.
Assuming low pressure and a thin sheath, ionisation in the sheath can be ignored, and conservation of ion flux gives

$$n_i(x)\,u(x) = n_{is}u_s \tag{1.5}$$

where n_i is the ion density and n_{is} is the ion density at the sheath edge. Solving for u we obtain

$$n_i = n_{is}\left(1 - \frac{2e\Phi}{Mu_s^2}\right)^{-1/2} \tag{1.6}$$

Assuming the electrons are in Boltzmann equilibrium at a temperature, T_e, the electron density is given by the Boltzmann relation

$$n_e(x) = n_{es}e^{e\Phi(x)/kT_e} \tag{1.7}$$

where n_{es} is the electron density at the sheath edge, $n_{es} = n_{is} = n_s$.
The variation of potential, Φ, across the sheath is described by Poisson's equation

$$\frac{d^2\Phi}{dx^2} = \frac{e}{\epsilon_0}(n_e - n_i) \tag{1.8}$$

where ϵ_0 is the permittivity of free space.

This gives us a non linear equation governing the sheath potential and ion and electron densities. The complete solution of Poisson's equation for the sheath can only be found numerically. However, analytically it is apparent that the equation can only be satisfied for,

$$u_s \geq u_B = \sqrt{\frac{kT_e}{M}} \tag{1.9}$$

This is known as the *Bohm sheath criterion* for the formation of the sheath. The velocities of ions at the sheath edge must exceed the critical value of the *Bohm velocity*, u_B. Therefore a small electric field must be present between the bulk plasma and the sheath to accelerate the ions to the Bohm velocity [31, 5, 6]. This region is called the *presheath*. A small potential can have a significant influence on ions whereas not such a big effect on the already hot electrons. Quasi-neutrality still holds in the presheath region.

1.2.1 Sheath potential at a floating wall

The potential drop between a plasma and an electrically floating wall is determined by equating the ion flux, Γ_i, to the electron flux, Γ_e, at the wall. That is,

the electron current through the sheath should balance the ion current

$$\Gamma_i = \Gamma_e \tag{1.10}$$

Due to conservation of flux in the sheath, the flux of ions at the wall is assumed to be the same as the flux of ions at the sheath edge. Therefore the ion flux at the wall can be given by

$$\Gamma_i = n_s u_B \tag{1.11}$$

where n_s is the plasma density at the sheath edge.

The electron flux at the wall is given by

$$\Gamma_e = \frac{1}{4} n_s \exp\left(\frac{e\Phi}{kT_e}\right) \bar{\nu_e} \tag{1.12}$$

where $\bar{\nu_e} = \sqrt{\frac{8kT_e}{\pi m}}$ is the mean electron speed for an assumed maxwellian distribution and T_e is the electron temperature.

From this the sheath potential can be calculated to be

$$\Phi = -\frac{kT_e}{e} . \frac{1}{2} \ln\left(\frac{M}{2\pi m}\right) \tag{1.13}$$

which is dependent on, the ratio of ion mass, M, to electron mass, m, and on electron temperature, T_e.

For the case of H_3^+ ions, in a Hydrogen plasma, the energy ions gain in the presheath and sheath, can be found to be $\simeq 3.9kT_e$.

1.2.2 High voltage sheath

When an external high potential is applied to an electrode the sheath potential changes.

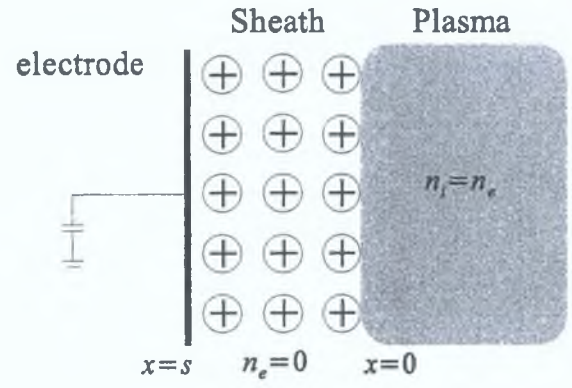

Figure 1.3: *Matrix sheath model*

Matrix sheath

A simple model describing the high voltage sheath is the Matrix Sheath model [1]. This model is not completely accurate but gives insight into the sheath formation.

It is assumed that the sheath region consists only of ions, and electrons are confined in the plasma bulk due to the large potential barrier between the biased electrode and the plasma. Since the biased electrode conducts electrical current, the zero net current requirement of the floating sheath is not required. Instead, the potential difference between the plasma and the electrode sets the sheath conditions. The ions in the space charge region are assumed to be fixed in a uniform matrix ($n_i = n_s = constant$). Figure 1.3 shows a diagram of the matrix sheath model. This is not entirely accurate since in reality the ions are not homogeneously distributed throughout the sheath.

The matrix sheath electric field, E, is calculated

$$\frac{dE}{dx} = \frac{en_i}{\varepsilon_0} \tag{1.14}$$

$$\Rightarrow E = \frac{en_i}{\varepsilon_0}x \tag{1.15}$$

where e is the elementary electronic charge, ε_0 is the permittivity of free space and n_i is the ion density in the sheath. The electric field is found to be a linear relation with distance, x. Integrating equation 1.15, the sheath potential is found

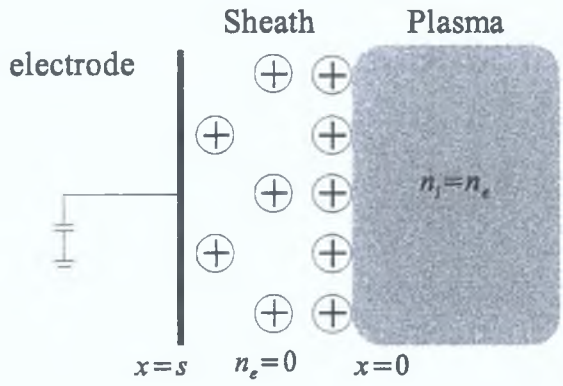

Figure 1.4: *Child Law sheath model*

to be

$$\Rightarrow \Phi = -\frac{en_s}{\varepsilon_0} \cdot \frac{x^2}{2} \tag{1.16}$$

The ion matrix sheath models can be a good approximation at high pressures in the limit of mobility limited ion motion.

Child Law sheath

As mentioned above the matrix sheath model is not entirely accurate since it does not allow for the reduced ion density due to ion acceleration towards the electrode surface. Figure 1.4 shows that as the ions are accelerated towards the electrode, by the sheath electric field, the ion density decreases.

Given that the initial ion energy on entering the sheath is small compared to the energy gained, due to the potential drop in the sheath, ion energy conservation, equation 1.4, can be approximated by

$$\frac{1}{2}Mu^2 = \frac{1}{2}Mu_B^2 - e\Phi(x) \cong -e\Phi(x) \tag{1.17}$$

and flux conservation, equation 1.5, given by

$$j_0 = en_s(x)u(x) \tag{1.18}$$

where j_0 is the current density.

The current density, j_0, can be found to be

$$j_0 = \frac{4}{9}\varepsilon_0 \left(\frac{2e}{M}\right)^{1/2} \frac{V_0^{3/2}}{s^2} \tag{1.19}$$

where V_0 is the applied electrode voltage and s is the sheath width. This is the Child-Langmuir space charge limited current equation. The potential as a function of position can be given by

$$\Phi = -V_0 \left(\frac{x}{s}\right)^{4/3} \tag{1.20}$$

the sheath width by

$$s = \frac{\sqrt{2}}{3}\lambda_{De} \left(\frac{2eV_0}{kT_e}\right)^{3/4} \gg \lambda_{De} = \sqrt{\frac{\varepsilon_0 kT_e}{e^2 n}} \tag{1.21}$$

where λ_{De} is the electron debye length at the sheath edge and the density is given by

$$n = \frac{4}{9}\frac{\varepsilon_0}{e}\frac{V_0}{s^2}\left(\frac{x}{s}\right)^{-2/3} \tag{1.22}$$

It can be seen that at the sheath edge, $x = 0$, n goes to ∞. This is a consequence of the approximation, made in equation 1.17, of neglecting the bohm velocity.

1.2.3 Collision dominated sheaths

The basic mechanisms regarding the plasma boundary sheath have been established. However the kinetics of ions through the sheath have not been considered. As the pressure increases, ions undergo collisions while travelling through the sheath. Thus, if ions lose energy through collisions their mean impact energy will decrease. For the case of collisional sheaths, ions traversing the sheath do not gain the full potential drop across the sheath. The energy of ions at the electrode surface will also be dependent on the collisions they undergo while trav-

elling through the sheath. If we consider the case where the ion mean free path, $\lambda_i \ll s$, the sheath width, then the assumption of energy conservation no longer holds. Instead the ion drift velocity, v, is friction limited and dependent on the local electric field.

$$v = v\left(E\left(x\right)\right) \tag{1.23}$$

Collision dominated sheaths are assumed for pressures $> 10\,Pa$. It is assumed that collisions do not result in ionisation, recombination, dissociation or any other chemical reactions. Therefore no particles are destroyed or created. Hence, the flux is still conserved

$$\Gamma_0 = \Gamma\left(x\right) = n\left(x\right)v\left(x\right) \tag{1.24}$$

Using Poisson's equation for the local electric field the following relates the ion velocity to the sheath electric field.

$$v\left(E\right)dE = \frac{e\Gamma_0}{\varepsilon_0}dx \tag{1.25}$$

To solve this equation we need the relationship between the velocity and local electric field. This depends on the pressure regime. For the intermediate pressure regime (10 - 100 Pa) which is relevant for this work the assumption of constant mean free path can be made. For this condition we find the following relationship between velocity and electric field [1].

$$v = 0.8\sqrt{\frac{\lambda e}{M} \mid E \mid} \tag{1.26}$$

This lets us obtain the following expression for sheath potential

$$\Phi = -V_0\left(1 - \frac{x}{s}\right)^{5/3} \tag{1.27}$$

1.2.4 Ion energy distribution function

For the case of the collisionless sheath all ions arrive at the electrode surface with energy, eV_0. However, this is not the case for a collision dominated sheath. The

effect of collisions is important since they can significantly modify the IEDF. The case of charge exchange collisions with a constant mean free path is considered. This particular case can easily be derived under the following assumptions [32]:
A constant mean free path. This is a reasonable approximation since the cross-section for charge exchange has a logarithmic velocity dependence.
$\sigma = \sigma_{ex}$.
Flux is conserved in the sheath, no ionisation.
The gas temperature is assumed to be zero.

Using the sheath potential of equation 1.27 when $\lambda \ll s$ we find the following energy distribution function of ions at the electrode [33]

$$f(E) = \frac{3}{5}\frac{s}{\lambda} exp\left(-\frac{3}{5}\frac{s}{\lambda}\frac{E}{V_0}\right) \tag{1.28}$$

1.2.5 RF sheath

When an ac potential is supplied across the sheath more complicated dynamics arises. To explain the dynamics of rf sheaths a simple qualitative model, developed by V. A. Godyak [34], provides simple analytical expressions. A symmetric discharge with sheath, a and b, is considered. It is assumed that the ion density is uniform and constant in time throughout the discharge and there are no electrons in the sheath region. These assumptions were also made for the static matrix sheath model discussed earlier.

The electric field, E_a, within sheath a is described by the integration of Poisson's equation.

$$E_a(x,t) = \frac{en}{\varepsilon_0}\left[x - s_a(t)\right] \tag{1.29}$$

where $s_a(t)$ is the position of the instantaneous sheath edge

$$s_a(t) = s\left(1 - \sin\left(\omega t\right)\right) \tag{1.30}$$

where s is the time averaged sheath width. The sheath edge is no longer static, as for the dc sheaths considered above, instead it oscillates in time.

Ions do not carry any rf current and the electron density in the sheath is assumed to be zero. Therefore, in contrast to the plasma bulk, the current through the sheath is displacement current. The displacement current is given by temporal derivative of E_a

$$I_a(t) = \varepsilon_0 A \frac{\partial E_a}{\partial t} \tag{1.31}$$

where A is the area of the electrode. Due to current continuity I_a is equal to the discharge current I_{rf}

$$I_a(t) = I_{rf}(t) = \widetilde{I_{rf}} \cos(\omega t) \tag{1.32}$$

this results in

$$I_{rf}(t) = -enA \frac{ds_a(t)}{dt} \tag{1.33}$$

with the following relationship between $\widetilde{I_{rf}}$ and s

$$s = \frac{\widetilde{I_{rf}}}{en\omega A} \tag{1.34}$$

The voltage drop across sheath a is given by

$$V_a(t) = \int_0^{s_a(t)} E(x,t)\, dx = -\frac{en}{2\varepsilon_0} \left(s_a(t)\right)^2 \tag{1.35}$$

resulting in

$$V_a(t) = -\frac{ens^2}{2\varepsilon_0} \left(1 - \sin(\omega t)\right)^2 \tag{1.36}$$

Similarly the sheath voltage across sheath b is given by

$$V_b(t) = -\frac{ens^2}{2\varepsilon_0} \left(1 + \sin(\omega t)\right)^2 \tag{1.37}$$

Neglecting a voltage drop across the plasma bulk we obtain the total voltage drop across the discharge V_{rf} by combining the sheath voltages V_a and V_b

$$V_{rf}(t) = V_a(t) - V_b(t) = \frac{2ens^2}{\varepsilon_0} \sin(\omega t) \tag{1.38}$$

There is second harmonic generation for the individual sheath voltages while the

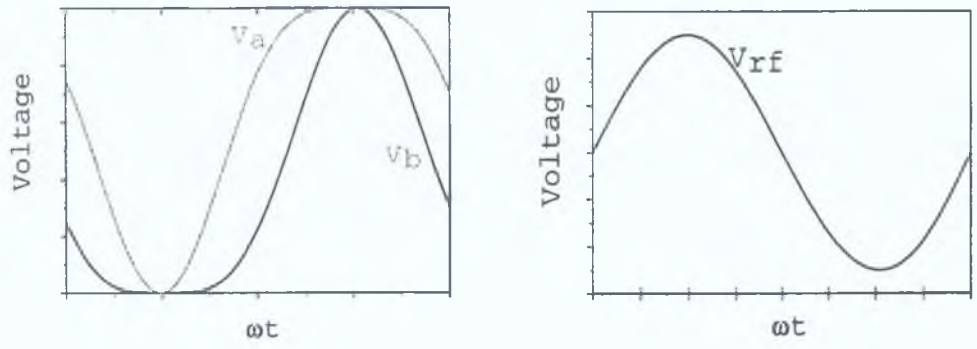

Figure 1.5: *Sheath voltages, V_a and V_b, as a function of time for a symmetric CCRF discharge*

total voltage drop across the discharge is free of harmonic generation. This can be observed in figure 1.5, where the individual sheath voltage waveforms and the total applied sheath voltage waveform is shown. Taking an applied rf voltage V_{rf}

$$V_{rf}(t) = \widetilde{V_{rf}} \sin(\omega t) \tag{1.39}$$

the sheath voltages a and b are given by

$$V_a(t) = -\frac{\widetilde{V_{rf}}}{4}(1 - \sin(\omega t))^2 \tag{1.40}$$

and

$$V_b(t) = -\frac{\widetilde{V_{rf}}}{4}(1 + \sin(\omega t))^2 \tag{1.41}$$

The relationship between the applied rf voltage, $\widetilde{V_{rf}}$, and the sheath width, s, is

$$s = \sqrt{\frac{\varepsilon_0 \widetilde{V_{rf}}}{2en}} \tag{1.42}$$

In reality the sheath dynamics are more complicated than this and more complex analytical models are available [25], however, this simple model amply illustrates the basic phenomena of rf sheaths. The dynamics of rf sheaths in Hydrogen discharges can be particularly complex. Under certain conditions a so

called field reversal is observed [35, 36]. The electric field in the sheath region reverses for a short phase during the rf cycle. During this phase electrons are accelerated towards the electrode. The reversal is caused by the combination of a comparatively high mobility of hydrogen ions and a relatively low mobility of electrons in hydrogen gas. The field reversal arranges for compensation of the positive ion flux and the negative electron flux to the electrode.

1.3 Ion transport in the sheath

The plasma potential of the bulk discharge and the positive ion sheaths are spatially and temporally rf modulated [10, 82]. Ions travelling through the sheath of an rf discharge arrive at the electrode with a distribution of energies [37]. This IEDF will reflect the acceleration of ions by the electric field of the oscillating plasma sheath. The ion energy is determined by the potential difference that the ion passes during its transit through the sheath. There are two main factors influencing this energy distribution; transit time of ions through the sheath and collisions the ions undergo in the sheath. In the case investigated here the ion transit time is comparable to the rf period (intermediate frequency regime). Thus, the IEDF depends on the external voltage phase in which the ions enter the sheath since this defines the potential difference they can cross [38]. Most ions enter the sheath when the sheath potential is at its maximum or minimum since these values of the sheath potential are experienced for longer than other values. Consequently, the IEDF, at the surface, will be characterised by the well-known saddle-shaped structure consisting of two peaks corresponding to the maximum and minimum sheath potentials respectively [10, 34, 39].

1.3.1 Collisionless sheath

If the sheath is collisionless, ions do not suffer energy losses, and their energy at the surface will be determined by the potential of the sheath edge with respect to the electrode potential.

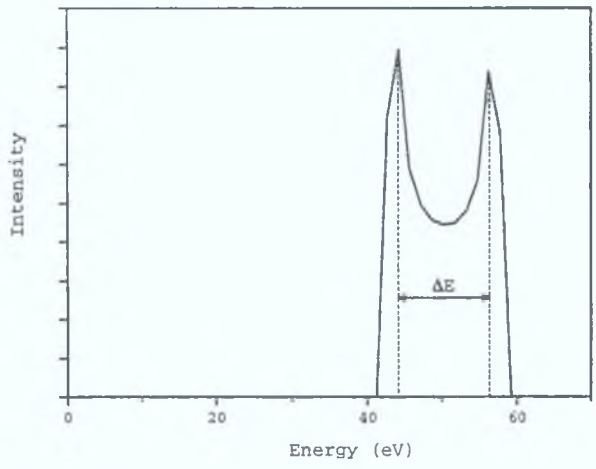

Figure 1.6: *Typical bi-modal IEDF structure*

In a collisionless sheath, the crucial parameter in determining the shape of the IEDF is the ratio of the ion transit time (τ_{ion}) to the rf period (τ_{rf}) [37].

$$\frac{\tau_{ion}}{\tau_{rf}} = \frac{3\overline{s}\omega}{2\pi}\left(\frac{M}{2e\overline{V_s}}\right)^{\frac{1}{2}} \tag{1.43}$$

where $\overline{s}$ is the time-averaged sheath thickness, ω is the rf frequency, M is the ion mass, $\overline{V_s}$ is the time-averaged sheath potential, and e is the elementary charge.

When $\frac{\tau_{ion}}{\tau_{rf}} \ll 1$, ions traverse the sheath in a short time compared to the field oscillations. Under this condition an ion traversing the sheath experiences the instantaneous sheath voltage and the phase of the rf cycle in which the ion enters into the sheath is important. In this low-frequency regime rf modulation of the IEDF can be observed due to the time-varying electric field and the ions' response to the electric field. The resultant IEDF has a double peak structure, the higher energy peak corresponding to the ions entering the sheath at the maximum sheath voltage and the lower peak is due to the ions entering at the minimum sheath voltage. The double peak structure is centered at the time-averaged plasma potential.

As the frequency increases, the fraction of the rf cycle the ions take to cross

the sheath increases and they no longer experience a constant potential but a range of potentials. Ions which enter the sheath at the maximum will be in the sheath for long enough to also experience lower potentials and ions which enter at the minimum will experience a higher potential average. Hence, the peaks in the saddle-shaped structure come closer together and the separation decreases.

If the ion transit time is long compared to one rf period, $\frac{\tau_{ion}}{\tau_{rf}} \gg 1$, the ions will experience many rf cycles while crossing the sheath. Thus, the oscillating rf sheath will be averaged out and ions will respond to the time-averaged sheath potential. The phase in which they first enter into the sheath becomes irrelevant. In this high-frequency regime, as the ion transit time, compared to the rf period increases, the width of the saddle-shaped structure decreases and the two peaks approach each other, until eventually they cannot be resolved. The IEDF is characterised by a single peak centered at the time-averaged sheath potential.

The case where the ion transit time is comparable to the rf period is not well understood [40]. This intermediate-frequency regime, $\frac{\tau_{ion}}{\tau_{rf}} \simeq 1$, lies between the two regimes discussed above and ions take only a few rf cycles to traverse the sheath. Ions move at velocities less than the velocity of the sheath boundary. Thus, ions taking a few rf cycles to reach the electrode, will spend part of their time in a low electric field, behind the sheath edge, and part of their time in the high field of the sheath. Thus, ions experience alternating sequence of constant velocity and varied acceleration as they travel towards the electrode. The IEDF depends on the phase in which the ion enters into the sheath and also the number rf cycles it takes to cross the sheath. In this regime, the two peaks in the double-peak structure can usually be observed close together with variations in the peak heights.

An analytical expression for the energy separation between the maximum and minimum energy peaks in the IEDF in the case of a collisionless sheath was first

calculated by Benoit-Cattin and Bernard [41]:

$$\Delta E_i = \frac{8e\widetilde{V}_s}{3\overline{s}\omega}\left(\frac{2e\overline{V_s}}{M}\right)^{\frac{1}{2}} \tag{1.44}$$

$$= \frac{4e\widetilde{V}_s}{\pi}\left(\frac{\tau_{rf}}{\tau_{ion}}\right) \tag{1.45}$$

This expression predicts that the peak separation, ΔE_i, depends on frequency, ion mass, applied rf voltage and sheath width.

1.3.2 Collisions in the sheath

An ion arriving at the plasma sheath boundary entering into the sheath gains energy through acceleration by the sheath potential. In the absence of collisions the ion would accelerate across the sheath and hit the electrode with an energy equivalent to the sheath potential. However, if the ion mean free path becomes smaller than the sheath thickness, then the ion is very likely to undergo collisions while traversing the sheath. As the pressure increases, and ion-neutral collisions in the sheath become more probable, the shape of the ion energy distribution changes significantly. The IEDF structure becomes more complicated, broadens and moves to lower energies. The type and probability of collisions in the sheath affects the shape of the IEDF. Two kinds of collisions, elastic collisions and symmetric charge exchange, are important and how they effect the energy distribution functions are discussed.

Elastic collisions Elastic collisions will lead to a deviation from the perpendicular incidence of ions on the electrode and to a loss of kinetic energy. When an ion traverses the sheath, only its velocity component normal to the surface is accelerated. Thus, if the ion does not undergo a collision in the sheath it would arrive at the surface with a large perpendicular component and small parallel component. If an ion interacts with a neutral particle the ion will lose energy and be scattered. Subsequently the ion will continue to be accelerated perpendicular to the electrode by the sheath electric field and will arrive at the electrode with an

incident angle, smaller than the scattering angle. The effect of elastic scattering will thus lead to a broader angular distribution of the velocity of ions and also a low energy tail in the energy distribution. Ions that are scattered over large angles modify the angular distribution greatly. Lighter ions are scattered over larger angles than heavier ions.

Symmetric charge exchange The influence of symmetric charge exchange is visible through a number of additional peaks at distinct energies. When such a charge exchange collision occurs, the newly created ion is almost at rest and has to restart its acceleration toward the surface. Multiple peaks are generated by the effect of the rf modulated electron density in the sheath [38, 42]. In a time varying sheath, the sheath periodically expands and retracts. If an ion is created through charge exchange in the quasi-neutral part of the plasma, where the local electric field is zero, when the electron density front is between it and the electrode, it will remain at rest. When the electron front moves back and the field rises again the ion will be accelerated towards the electrode. All ions which have been created at the same time and distance from the electrode will thus be accelerated together and contribute to a secondary low energy peak in the IEDF. Thus, ions are grouped together and each successive rf cycle creates a new group. The group with the lowest energy was created one cycle before arrival at the electrode. The average energy of each group corresponds to the average potential drop the ions have experienced. The number of peaks in the distribution is then characteristic of the number of rf cycles it takes an ion to cross the sheath.

1.4 Hydrogen chemistry

In Hydrogen discharges, three different positive ion species can coexist, H^+, H_2^+, H_3^+ and can inter-convert by collisions with the background H_2 molecules [43, 44]. In the plasma bulk, electron impact ionisation produces mainly H_2^+ thermal ions. These H_2^+ ions, through collisions with the background gas, can be converted into

H_3^+ by the very efficient exothermic conversion reaction

$$H_2^+ + H_2 \rightarrow H_3^+ + H + 1.71\,eV \tag{1.46}$$

which has a large cross section. H_3^+ ions can be destroyed through collisions with the background gas, at energies in excess of about 10 eV. Thermal H_3^+ ions only interact with the background gas through elastic collisions where the momentum-transfer cross-section dominates. Therefore, in the low electric field region of the plasma bulk the dominant ion is H_3^+. The ions entering into the boundary sheath from the plasma bulk are, therefore, predominantly H_3^+. After acceleration by the sheath electric field, H_3^+ ions can then undergo collisions with the background gas and convert into H^+ and H_2^+. Beyond about 10 eV, H_3^+ ions can be destroyed through collision-induced dissociation and asymmetric charge transfer producing both $H^+$and H_2^+ ions. The collision induced dissociation reactions

$$H_3^+ + H_2 \rightarrow H^+ + H_2 + H_2 \tag{1.47}$$

$$H_3^+ + H_2 \rightarrow H_2^+ + H + H_2 \tag{1.48}$$

result in the dissociation of H_3^+ ions producing fast H^+ or H_2^+ ions and neutral particles. These processes often involve no energy transfer to the target H_2 molecule. The asymmetric charge transfer reactions

$$H_3^+ + H_2 \rightarrow H_2 + H + H + H^+(slow) \tag{1.49}$$

$$H_3^+ + H_2 \rightarrow H_2 + H + H_2^+(slow) \tag{1.50}$$

result in exchange of the charge on the H_3^+ ion to a neutral. This leads to a complete loss of energy of the H_3^+ ion, which is taken over by the neutral producing either slow H^+ or H_2^+ ions and energetic neutrals. Above about 20 eV, the elastic cross section decreases dramatically and it can be assumed that H_3^+ ions are either in free fall or are destroyed, by either collision induced dissociation or asymmetric charge transfer, mechanisms discussed above. All other possible

collision processes of H_3^+ have an order of magnitude smaller cross-sections for the conditions considered here and therefore do not play a significant role.

The predominant collision process that determines the ion velocity distribution of H_2^+ ions in the boundary sheath is resonant symmetric charge exchange

$$H_2^+(fast) + H_2(slow) \rightarrow H_2(fast) + H_2^+(slow) \tag{1.51}$$

Above a few eV charge exchange of H_2^+ takes over, from the exothermic conversion reaction (equation 1.46) described above, as the dominant ion-neutral interaction. After acceleration by the sheath electric field the collision of H_2^+ with background gas molecules will result in a transfer of charge from the H_2^+ ion to the H_2 neutral, thus, producing a fast H_2 neutral and the newly created H_2^+ ion will start acceleration from rest.

Most H^+ ions are formed in the sheath. The chemistry for H^+ in the sheath is rather complex and governed by several processes discussed in the literature.

1.5 Mass resolved ion energy analyser

Mass resolved ion energy analysers are versatile diagnostics for the analysis of neutral particles, in particular radicals [46, 47], and positive [48, 49, 50, 51] and negative [53] ions. The principles of operation of commercial mass resolved ion energy analysers are discussed, paying particular attention to the Hiden EQP [54].

The IEDFs were measured using a Hiden EQP 2000 plasma probe, consisting of ion optics, an electrostatic energy analyser (ESA), a quadrupole mass spectrometer (QMS), and finally a secondary electron multiplier (SEM) for ion detection. The main sections of the Hiden EQP are shown in figure 1.7. The EQP can perform ion energy scans at a particular mass to charge ratio by sweeping the various electrode voltages on the EQP. The entire plasma probe is mounted on the grounded electrode of the plasma system and housed in a two-stage differentially pumped vacuum chamber. A base pressure of less than 10^{-6} Pa is maintained

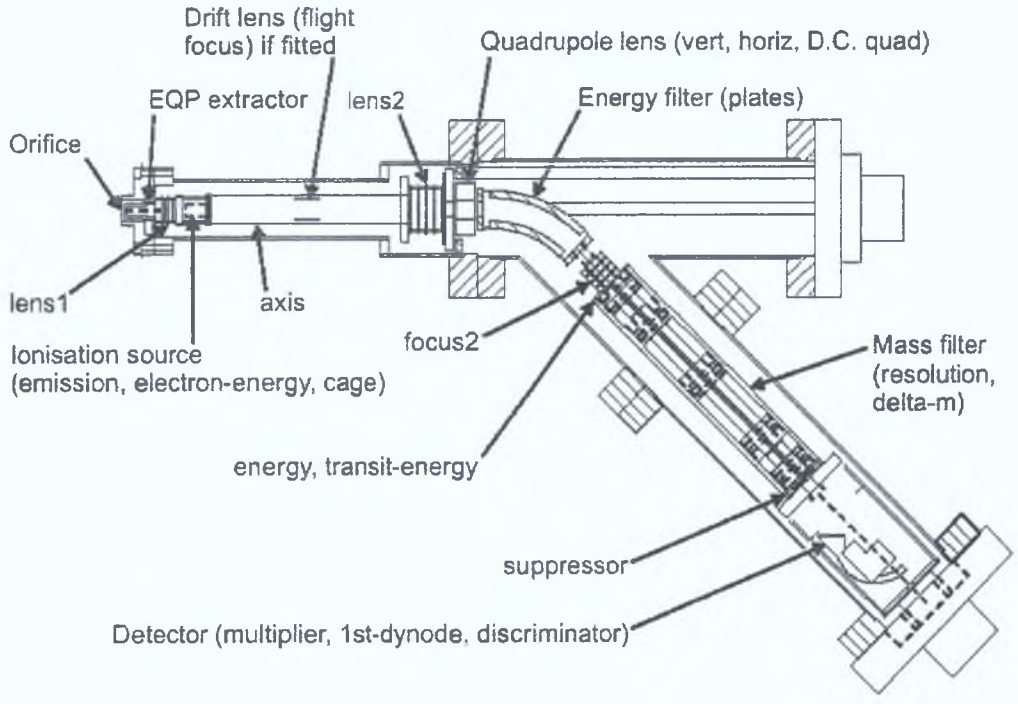

Figure 1.7: *Hiden EQP*

inside the EQP, irrespective of the pressure within the plasma chamber. This provides a collision free environment for ions as they traverse the EQP (section 3.3.1) and also correct uniform performance of the SEM detector.

Orifice When extracting particles from the plasma, a distinction must be made between neutrals and charged particles. Neutrals will simply drift into the mass resolved ion energy analyser whereas positive or negative ions may require specific arrangements. Positive ions leaving the plasma bulk are accelerated towards the surface of the grounded electrode by the sheath electric field. A small fraction of these ions can enter the 10 μm aperture positioned at the center of the grounded electrode. Negatively charged particles are usually efficiently trapped inside the discharge but can reach the walls; for example, the most energetic electrons can overcome the sheath potential and also reach the walls during the collapse of the sheath potential once in the rf cycle. When analysing positive ions to avoid interference with results these negatively charged particles need to be prevented

from entering the EQP. A negative voltage, *extractor*, is applied just after the entrance aperture to repel any negatively charged particles. This negative voltage will also help to accelerate and focus the positive ions inside the instrument. Negative ions can be detected by modulating the discharge, forcing the sheath potential to collapse, enabling the ions to reach the surface [55].

Ionisation Source The electron impact ionisation source is used for analysing neutrals. Since the energy analyser and mass filter exploit electric fields to analyse the particles neutrals cannot be directly detected and must first be converted to either positive or negative ions. Two filaments can emit electrons of controllable electron energy which bombard neutrals entering from the plasma. Positive or negative ions can be produced through ionisation or electron attachment [56], respectively. These ions can then be analysed using the energy analyser and mass filter in the same way as ions created, outside the instrument, in the plasma. The ionisation source is switched off when detecting ions.

Extraction Ions which have passed through the orifice are focused onto the exit aperture of the ionisation source by an electrostatic lens. This first lens consists of three electrodes; *extractor*, *lens 1* and *axis.* This lens also serves the purpose of accelerating or decelerating the entire ion energy distribution.

Drift Region This region transmits ions from the extractor and focuses them into the energy analyser. The particular EQP model used in this work has an extra long drift tube and therefore has an additional electrode fitted in the drift tube. The extra long drift tube allows additional freedom in positioning the EQP. The function of this additional electrode, *flight-focus*, is to transmit ions more efficiently through the tube, increasing sensitivity, by reducing the number of ions which are lost to the walls of the tube. Ions which have passed through the drift tube are then efficiently focused into the energy analyser by *lens 2* which creates a parallel beam at the entrance of the energy analyser.

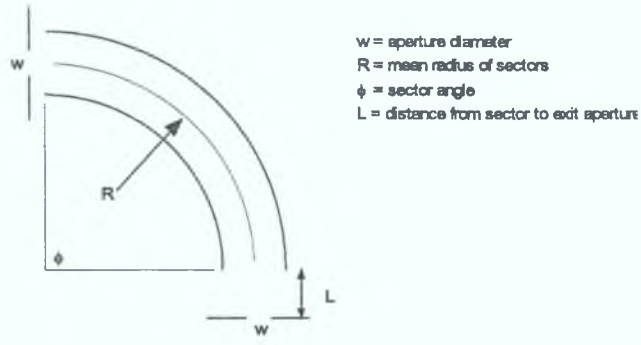

Figure 1.8: *Sector Field Energy Analyser*

Energy Analysis The energy analyser is a 45^0 sector field energy analyser. Ions entering the sector field are deflected according to their kinetic energy, so that only ions which have the pass energy of the analyser can pass the 45^0 bend. The pass energy is the energy ions need to pass the 45^0 bend of the electrostatic energy analyser. This, pass energy, can be set by the operator and for all measurements taken in this work it was set to 40 eV. 40 eV is the value recommended by the manufacturer, Hiden. Ions with the selected energy have previously been accelerated or decelerated to the pass energy of the ESA. The transit energy through the ESA is set by the potential, *axis*. The *plates* potential is used to tune the ESA to transmit particles, of *axis* energy. Alignment adjustments of the ion beam before entering the energy analyser can be made by variation of the voltages, *vert*, *horiz* and *D.C. quad.*

The energy resolution, ΔE, of the ESA is given by:

$$\Delta E = \frac{w.TE}{R(1-\cos\phi) + L\sin\phi} \tag{1.52}$$

where w is the aperture diameter, TE is the transmission energy, R is the sector mean radius, ϕ is the sector angle, and L is the distance to the exit aperture (see figure 1.8). In the EQP the following values are used: $w = 3$ mm, $R = 75$ mm, $\phi = 45$ degrees, $L = 35.4$ mm, $TE = 40$ eV (*axis* potential). The calculated energy resolution for a pass energy of 40 eV is 2.55 eV, which is small compared to the ion energies of interest.

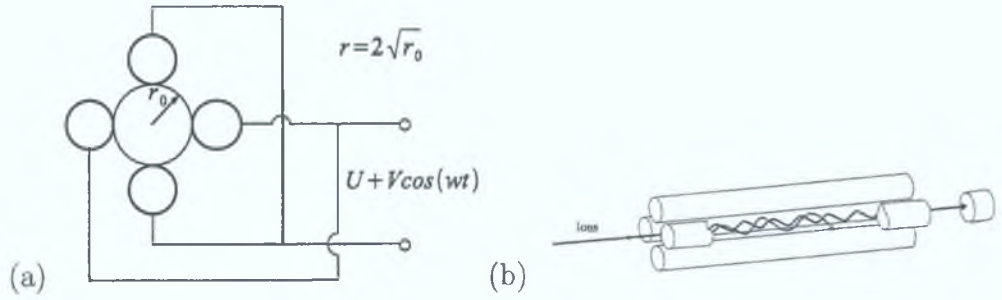

Figure 1.9: *Quadrupole mass filter (a) field generating potentials (b) trajectory of ions through quadrupole mass filter*

Mass filter Ions leaving the ESA all have the same energy but different masses since ion trajectories in constant electrostatic fields do not depend on ion mass [57]. An rf quadrupole mass filter is used to differentiate between ions according to their mass-to-charge ratio. A diagram of a quadrupole mass filter is shown in figure 1.9. It consists of 2 pairs of parallel, equidistant metal rods. Two opposing rods are connected electrically and have a positive potential while the other pair of opposite rods are at a negative potential of the same value. The applied potentials are a superposition of fixed dc and alternating radio-frequency components. These time-varying electric fields effect the trajectories of ions according to their mass-to-charge ratio [58, 59]. Any ions entering the quadrupole field will experience potential differences deflecting them from their original trajectory. The extent of deflection of any ion entering the field is related to its mass-to-charge (m/z) ratio. Mass selection can be acquired by varying the rf voltage. Ions of a prescribed mass/charge can describe a stable path allowing the ion to pass through the quadrupole. All other ions are excluded due to their unstable paths. They strike the rods, are neutralised by impact and pumped away as gas. Only ions which have a stable trajectory can exit the quadrupole and be detected. Ions must remain long enough in the quadrupole mass filter to achieve a good mass resolution. Consequently the entrance energy should be low, in the order of a few eV, to achieve this ions are previously decelerated using the lens *focus 2*. The mass resolution can be controlled by the two variable voltages, *delta-m* and *resolution*.

The mass filter used here is a triple quadrupole mass filter and separates ions according to their mass-to-charge ratio up to a maximum of 2000 amu. This type of mass filter as opposed to a single quadrupole has additional pre and post filters, placed in front and at the rear of the main quadrupole. The resolution of the quadrupole increases in proportion to ion mass. Therefore, it is generally more difficult to achieve good mass separation for low masses, such as hydrogen ions. The cylindrical rods in the quadrupole are of large diameter, 9 mm. The larger the diameter of the rods the better the mass separation that can be achieved. With this large quadrupole improved mass separation can be obtained. This is especially beneficial in the low mass region when investigating hydrogen ions.

Ion detection Finally, ions of selected energy and mass are detected. Filtered ions strike the detector resulting in an ion current which is measured by a sensitive amplifier. There are two detector options available on the EQP.

The *Faraday Cup* is an earthed passive conducting surface with a suppressor electrode to avoid false measurement. Fast moving ions strike the cup and cause a shower of secondary electrons. The use of the cup rather than a plate, makes it improbable for ions to escape after they have entered the cup, and also allows all electrons to be collected. Hence, one ion arriving at the Faraday needs one electron for neutralisation but causes several electrons to be emitted; this provides an amplification of several electrons for each ion.

The *Secondary Electron Multiplier (SEM)* consists of a surface designed to generate secondary electrons. When an ion impacts the surface it generates 2 or 3 electrons, each of which undergo further collisions with a second surface generating more electrons, and so on forming an avalanche. Power for this cascade is provided by an applied voltage to the first surface, *1st-dynode*, and another voltage on the other surfaces, *multiplier*. A much higher amplification is obtained using an SEM and makes it far more sensitive than the Faraday cup.

For the measurements taken in this work the SEM detector is used since it is more sensitive and the Faraday cup detector produces a large background signal. However, extreme care has to be taken when using SEMs, the surface deteriorates

in time, which causes the gain to decrease. Also, the SEM was not operated above a base pressure of 10^{-6} Pa to ensure correct and uniform performance of the detector.

1.6 PIC simulations

Experiments can provide the basis for exploring new phenomena and validating current theoretical models in plasma physics. However, used in combination with simulations they can have synergistic effects. Simulations can be used to compare directly to experimental results and also as an extension to experiments providing results which can be difficult to obtain experimentally. There are various techniques used in modelling plasmas, for example, global models [60, 61, 62, 63, 64, 65], fluid models [66, 67, 68], circuit models, kinetic models [69, 70, 71, 72].

A kinetic scheme proved to be the most useful approach for comparison to the experimental investigations in this work. The Particle-In-Cell (PIC) simulation method and its implementation is discussed briefly. A more detailed description of the particular PIC simulations used can be found in [73, 74].

To obtain an exact description of a plasma, the position and velocity of each particle must be known. Each species of electron, ion and neutral has a distribution function described by the Boltzmann equation.

PIC simulations have the advantage that the fields and energy distributions can be obtained self-consistently from first principles. No assumptions about the electric field or the bulk plasma velocity distributions need to be made. The plasma is simulated as electrons and ions moving under the influence of electric fields. Neutrals are not simulated. Figure 1.10 shows the main steps involved in the PIC cycle. In PIC simulations super-particles are used to simulate the plasma. Each of these super-particles represents a large number of real particles (ions or electrons), typically on the order of $10^6 - 10^8$ real particles. The simulation region is divided into cells creating a spatial grid. The particles are loaded

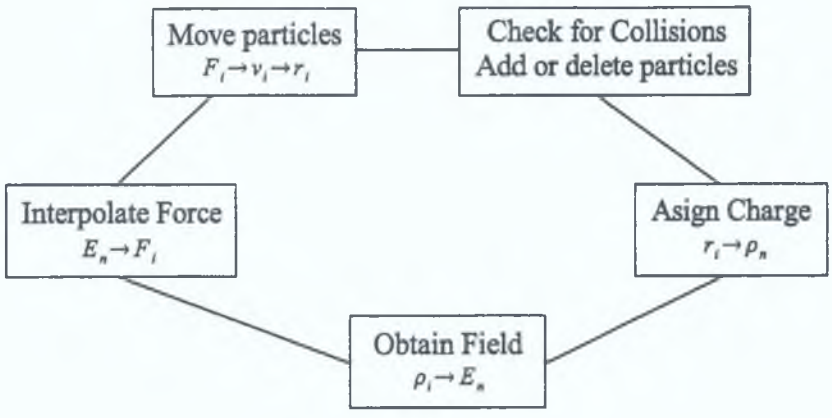

Figure 1.10: *Schematic of steps in Particle-in-Cell (PIC) simulation*

randomly into the simulation with a uniform density and Maxwellian velocity distribution. Each particle has a position and velocity recorded. From the positions and velocities of the particles the charge and current densities are obtained. The charge and current densities are used to calculate the electric field on the cells. The electrostatic field generated by a certain charge distribution can be obtained by solving Poisson's equation. The force acting on each particle can be obtained by interpolating the field, on the spatial grid, back to the particle position. The particles are then allowed to move in response to these fields. Particles pushed outside the spatial grid are removed. A Monte-Carlo collision handler is used to subject the particles to collisions [75]. The effects of collisions can be a change in particle velocity, particle loss and particle production. Input data of collision cross-sections are included in the model.

The main disadvantage of PIC simulations is the huge computational cost especially in 2D or 3D geometries. The time for the models to reach steady state can often be quite long. They can also be limited due to complex plasma chemistry and surface processes. Nevertheless, PIC simulations are a powerful tool for investigating low pressure discharge physics. It is useful in exploring new phenomena and validating current theoretical models. Effective way to model chemistry is to couple PIC simulations to global chemistry model.

CHAPTER 2

Design of the confined capacitively coupled rf discharge system

A detailed description of the experimental system designed for this work is presented in this chapter. The experimental system was designed to facilitate the measurement of ion energy distribution functions (IEDF) at a large boundary sheath potential using a mass resolved ion energy analyser. The other main objective of the design was to allow direct comparison to a 2D PIC simulation [62]. Large sheath potentials usually exist at biased electrodes. However, this is incompatible with the intention of using a mass resolved ion energy analyser which should be incorporated into a grounded electrode. Therefore, to achieve both these objectives a confined capacitively coupled rf (CCRF) discharge is the most suitable.

The final system configuration is shown in figure 2.1 and figure 2.2 shows a photograph of the experimental setup. Figure 2.3 shows a photograph of the CCRF plasma. The discharge system consists of two flat, parallel-plate electrodes. One electrode is grounded and the other powered. The electrodes are of equal area, diameter 140 mm, and separated by a 50 mm gap. The powered electrode is

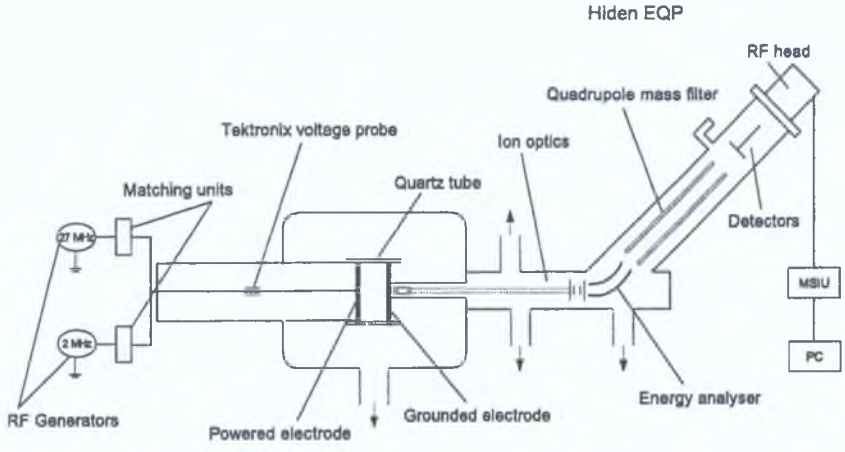

Figure 2.1: *CCRF Discharge Experimental Setup*

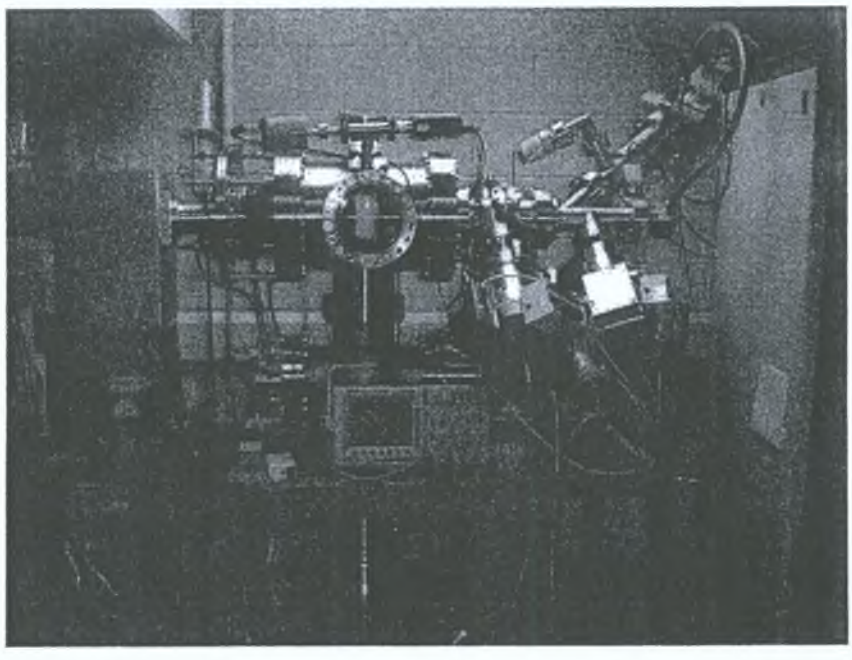

Figure 2.2: *Photograph of CCRF Discharge Experimental Setup*

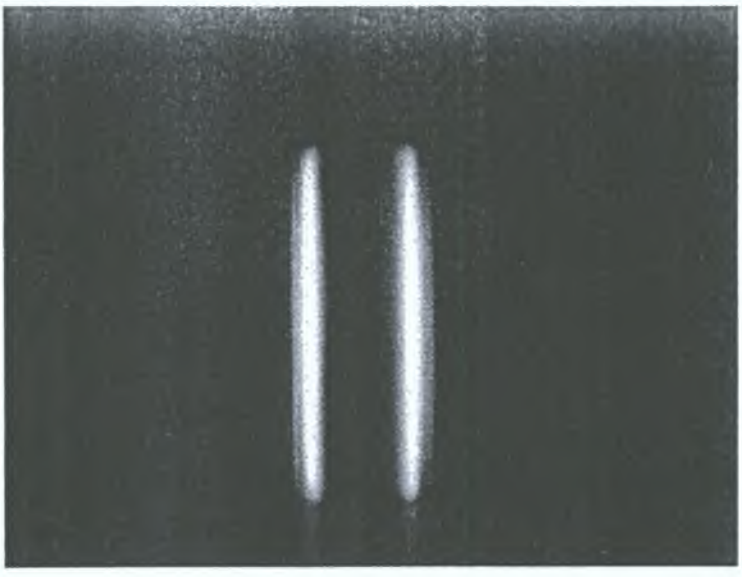

Figure 2.3: *Photograph of CCRF plasma*

water cooled. The grounded electrode is mounted on the Hiden EQP, which is in turn mounted to the chamber. A 10 μm orifice at the centre of the grounded electrode plate allows for mass resolved energy analysis of plasma species impinging on its surface. A two-stage differentially pumped vacuum system was designed to house the Hiden EQP, providing a collision free environment for particles as they traverse the probe. Gas is introduced to the chamber through a shower-head in the grounded electrode. The plasma is confined to the volume between the powered and grounded electrodes by a quartz tube, of wall thickness 5 mm. The quartz tube both shields the plasma from the grounded chamber walls, and creates a pressure differential between the inside and the outside of the tube. If the pressure on the outside of the tube is too low a discharge will not be sustained. The chamber is pumped from outside the quartz tube by turbo-molecular pumps. The gas pressure in the system is regulated using mass flow controllers.

Due to difficulties in installing a pressure gauge to measure the pressure inside the quartz tube without disturbing the plasma the Hiden EQP was calibrated to a Baratron pressure gauge and used to measure the pressure inside the quartz tube. Without the quartz tube in place the EQP was calibrated to the baratron pressure gauge for a given gas. With the quartz tube in place the EQP was used

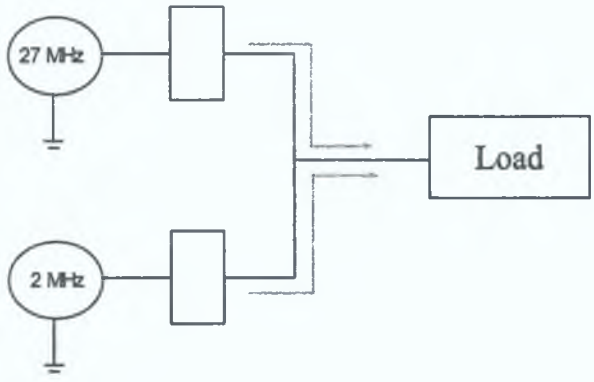

Figure 2.4: *Dual Frequency*

to measure the signal corresponding to the pressure inside the quartz tube and the baratron measured the pressure outside the tube.

Both single frequency and dual frequency plasmas can be ignited. Two different power sources are used on the system: a single frequency 13.56 MHz, and a second dual frequency system enabling frequencies of 1.94 MHz and 27.12 MHz to be supplied both separately and simultaneously as a true summation.

Single frequency 13.56 MHz An L-type matching unit couples the 13.56 MHz power signal to the powered electrode of the discharge. It comprises of a fixed coil and a series tuning capacitor and load capacitor. Both capacitors are motor driven and can be tuned manually or automatically. A Tektronix high voltage probe (Tektronix P6015A) is installed between the matching network and the powered electrode allowing voltage measurements.

Dual frequency 1.94 MHz & 27.12 MHz Two separate rf generators (1.94 MHz and 27.12 MHz) are interfaced to the plasma chamber using matching networks in the configuration shown in figure 2.4. The 1.94 MHz matching system uses rf relay-switching capacitors and a fixed inductor. The 1.94 MHz matching network allows 1.94 MHz power transmission to the plasma and rejection of 27.12 MHz signals. The 27.12 MHz matching unit consists of two vacuum-variable capacitors and a fixed inductor. It is designed to reject 1.94 MHz signals and

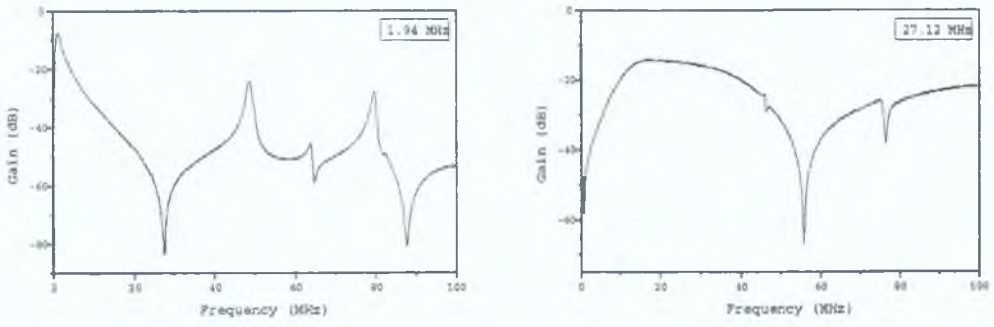

Figure 2.5: *Frequency response of (a) 1.94 MHz and (b) 27.12 MHz matching networks [76]*

transmit 27.12 MHz signals to the plasma. The 1.94 MHz and 27.12 MHz signals are summed after both matching networks prior to connection to the electrode. Figure 2.5 shows the frequency response of both the 1.94 MHz and 27.12 MHz matching networks. For the 1.94 MHz matching network, the minimum loss is at 1.94 MHz and there is a dip in the curve at 27.12 MHz and its harmonics. The 1.94 MHz matching network transmits 1.94 MHz signals to the plasma and at the same time acts as an rf filter to 27.12 MHz and its harmonics, blocking 27.12 MHz signals damaging the 1.94 MHz rf generator. The same applies to the 27.12 MHz matching network, which shows its minimum loss around 27.12 MHz and dips at 1.94 MHz. Figure 2.6 shows a voltage waveform measured at the powered electrode, showing the superposition of the 1.94 MHz and 27.12 MHz voltage. The voltage waveform does not show any second harmonic generation. The PIC simulation is driven using a voltage source so the voltage measurement and also the shape of its waveform is important for accurate comparisons.

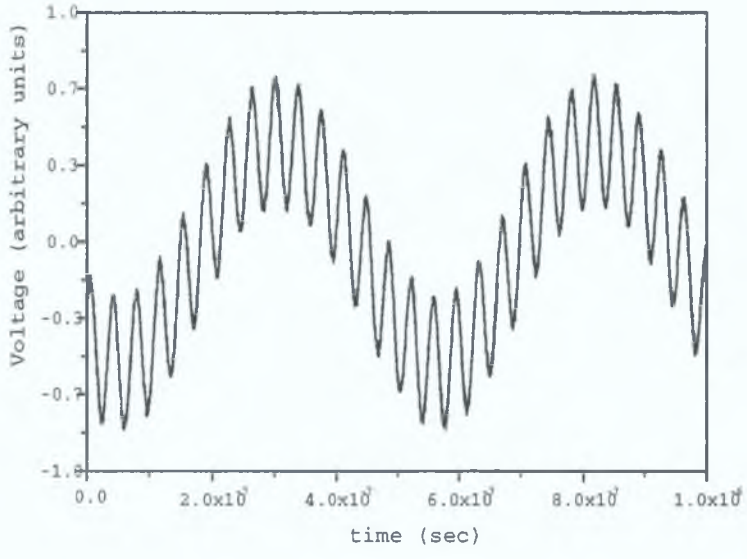

Figure 2.6: *Applied voltage waveform for the dual frequency plasma*

CHAPTER 3

Technique for measuring IEDFs

A mass resolved ion energy analyser was employed to measure ion energy distribution functions (IEDF) in the discharge. The basic principles of this diagnostic technique were discussed in section 1.5. Proper operation of such a system is challenging [16, 77, 78]. The ion transmission of the instrument can be affected by the ion optics settings selected. Ensuring uniform transmission becomes more difficult as the energy range of the measured distributions becomes larger. A technique for reducing energy discrimination was developed and is discussed.

3.1 Ion optics

The Hiden EQP consists of several electrostatic lenses which direct the incoming ions into the energy and mass filter. The functions of the different sections of the EQP were discussed in section 1.5. The ion optics section consists of a number of electrodes and focusing lenses, to each of which a voltage may be applied. The potentials are applied to the lenses in the configuration shown in figure 3.1. Understanding the operation of the electrode potentials is essential for correct operation of the EQP. To measure the IEDF of incoming ions from the

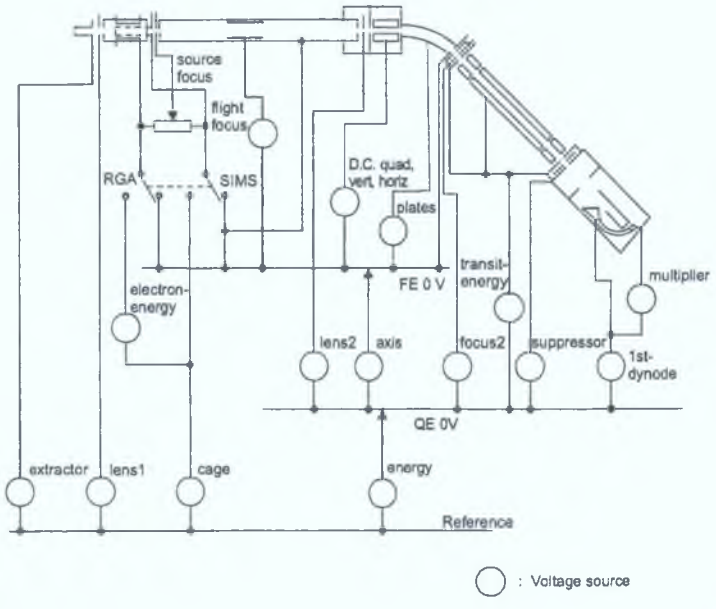

Figure 3.1: *Hiden EQP Potentials*

plasma the electrode voltages are varied in a specific manner. When some control voltages are scanned numerous electrode potentials may be varied as a result. For example, scanning *Energy,* scans not only the *axis* potential but also the potential on *lens 2*, *focus 2*, *suppressor*, and 1^{st} *dynode*. There is a big degree of freedom in choosing the values of the electrode voltages. Improper voltage settings on the electrostatic lenses can result in energy discrimination consequently distorting the measured IEDF. It is necessary to optimise the signal to noise ratio while taking precautions not to distort the shape of the actual distribution function.

Electrostatic lenses are subject to the same aberrations as optical lenses [79]. In this instrument the effect of chromatic aberration is the most problematic. Chromatic aberration is inherent to all lenses. This aberration effect is where the focal length of a lens is dependent on the ion energy. Therefore incoming ions of different energies will be focused at different positions. This can result in superior acceptance at certain ion energies. The following section discusses this energy discrimination and how to obtain voltage settings which reduce the aberration effects to a minimum.

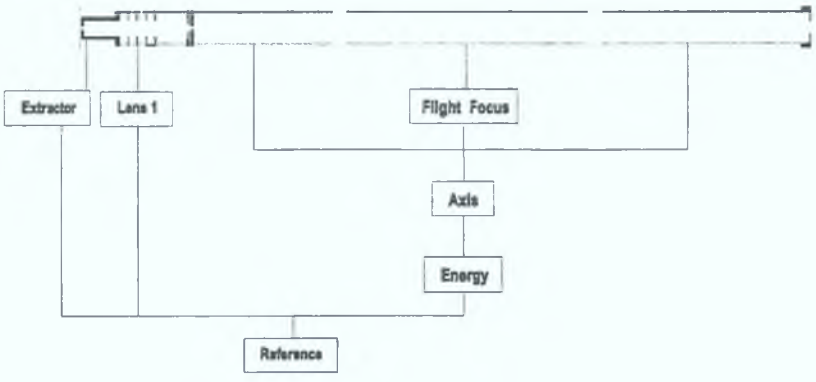

Figure 3.2: *Ion optics section simulated using SIMION*

3.2 Electrode voltage settings

A computer simulation package SIMION [80] was used to simulate the ion trajectories through the ion optics. SIMION models the electrostatic fields and forces created by the electrodes. When the electric fields have been obtained, the trajectories of charged particles in these fields can be calculated. SIMION was used to find settings for the voltages on the lenses which optimise the signal to noise ratio while ensuring that the aberration effects are kept to a minimum. Figure 3.2 shows the ion optics section simulated in SIMION. There are several more electrodes not shown in figure 3.2 but these are not of importance to the energy dependent transmission.

The first lens consists of three electrodes: *extractor*, *lens 1*, *axis*. The function of this first lens is to shape the ion beam, and simultaneously accelerate or decelerate the preselected ions to the pass energy of the energy analyser. This lens (*extractor, lens 1, axis*) focuses the incoming ions into the entrance region of the drift tube. The last electrode, at potential *axis*, is involved in the energy selection and is therefore fixed (section 1.5). However, the potentials on *extractor* and *lens 1* can both be varied. The electric field strength determines the extent to which ions are deflected and collected. Therefore, the voltage settings on the electrodes of this lens greatly influence the acceptance angle of the instrument.

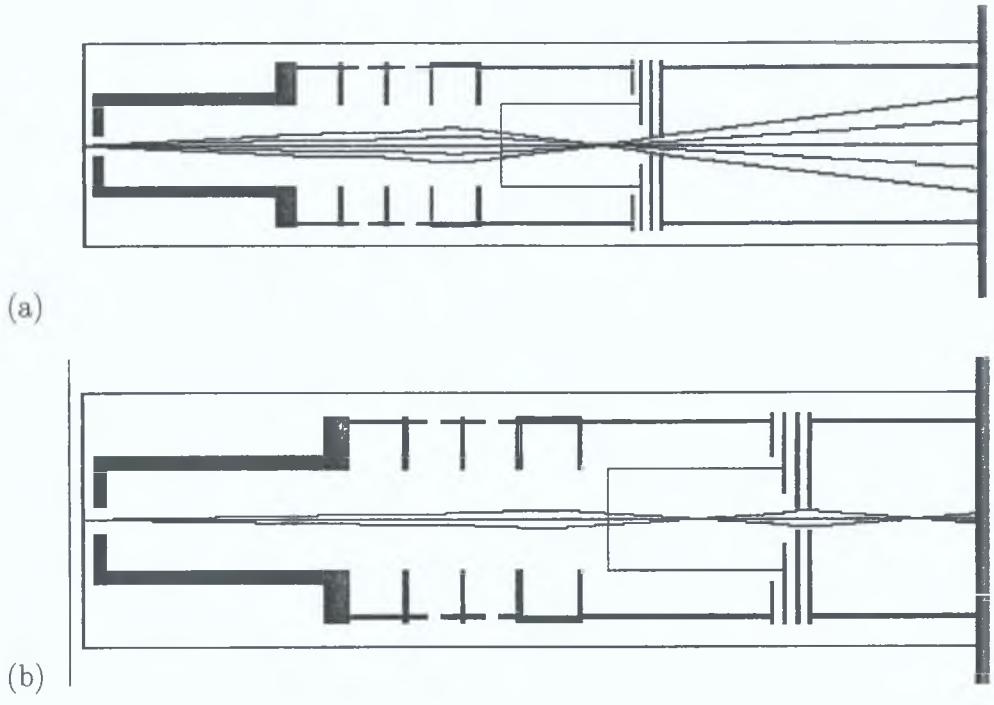

Figure 3.3: *Ion trajectories for (a) ions of energy 100 eV (b) ions of energy 300 eV*

As discussed in the previous section the focal length of the lens is dependent on the energy of the incoming ion. Therefore care must be taken to keep chromatic aberration effects to a minimum. After entering into the drift tube all ions, that can pass the energy filter, have the same energy. Therefore, chromatic aberration effects will not be present in any of the lenses behind the drift tube. The drift tube consists of three tubes; two outside tubes at a potential of *axis* and a center tube at an additional potential, *flight-focus*, that increases sensitivity of the instrument. *Flight-focus* is used to direct ions out of the long drift tube.

Ion trajectories, simulated using SIMION, at two different ion energies, 100 eV and 300 eV, are plotted in figure 3.3. The ions originate at a point source representing the orifice. The voltage settings on the lens are *extractor* = -40 V, *lens 1* = -190 V, *axis* = -40 V. The 300 eV ion beam is focused into the entrance of the drift tube while the 100 eV ion beam is unfocused after the first lens. This clearly illustrates chromatic aberration when the focal length of the lens is dependent on ion energy. Figure 3.4 is a plot of acceptance angle of the instrument as a function

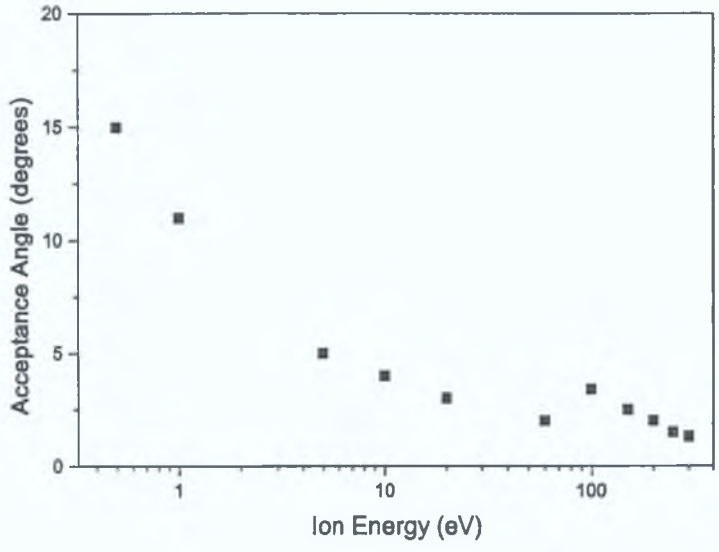

Figure 3.4: *Acceptance angle as a function of Ion Energy showing chromatic aberration (at the same electrode settings of figure 3.3)*

of ion energy for the same settings used in figure 3.3. There is a large acceptance angle for low energy ions, reflecting the fact that low energy ions are more easily deflected and focused in an electric field. However, the superior acceptance at 100 eV is clearly evident. This will result in more efficient transmission of 100 eV ions through the instrument resulting in a false peak at 100 eV in the measured IEDF.

Lens settings for the first lens in the system (*extractor*, *lens 1*, and *axis*) which reduce chromatic aberration effects were found by Hamers [77] and are presented in figure 3.5. He obtained the settings by simulating the ion trajectories through the ion optics using SIMION. He found combinations of *extractor* and *lens 1* which reduce the chromatic aberrations effects to a minimum. Using this information it is possible to experimentally determine values for the voltages. The electrode *lens 2* follows the drift tube, and since all the ions have the same energy after the drift tube *lens 2* should not exhibit chromatic aberration effects, provided correct voltage settings are used in the first lens. If chromatic aberration

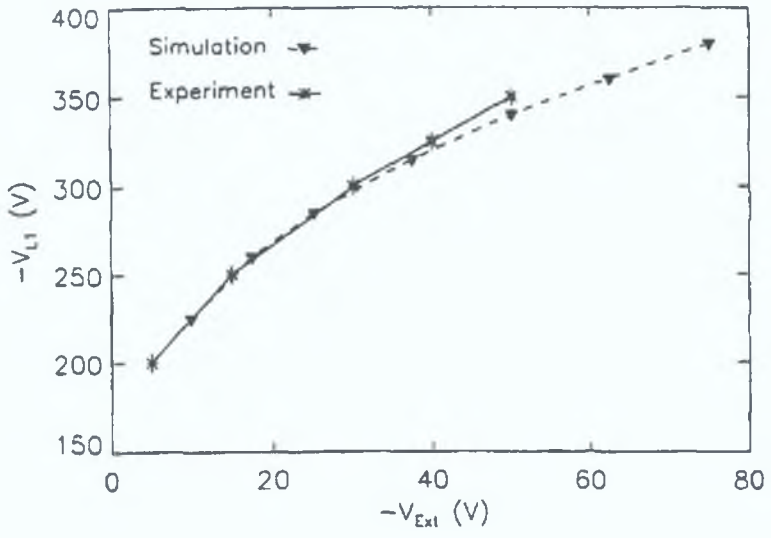

Figure 3.5: *Settings for extractor and lens 1 with reduced chromatic aberration taken from Hamers [77]*

is present in the first lens the focal length of *lens 2* will shift with ion energy. This can be checked experimentally by applying voltage settings to the first lens and scanning the voltage on *lens 2*. If the position of maximum intensity of the *lens 2* voltage scan moves with ion energy chromatic aberration is present in the first lens. However, if the position does not change the first lens is free from aberration effects.

The instrument used in this work is slightly different including an extra long drift tube and additional *flight-focus* electrode (as described above). Based on the method of Hamers, combinations for voltages on the electrodes were found by simulating the ion trajectories through the ion optics section, shown in figure 3.2, using SIMION. Settings were found which first focus the ion beam into the entrance of the drift tube and then from the entrance of the drift tube into the energy analyser behind the drift tube. A plot of maximum acceptance angle as a function of ion energy for the settings used is shown in figure 3.6. The acceptance angle will depend on the electric field just inside the orifice and hence on the settings of the first lens (*extractor*, *lens 1* and *axis*). The larger the extractor voltage the larger the acceptance angle. The values used provide the maximum

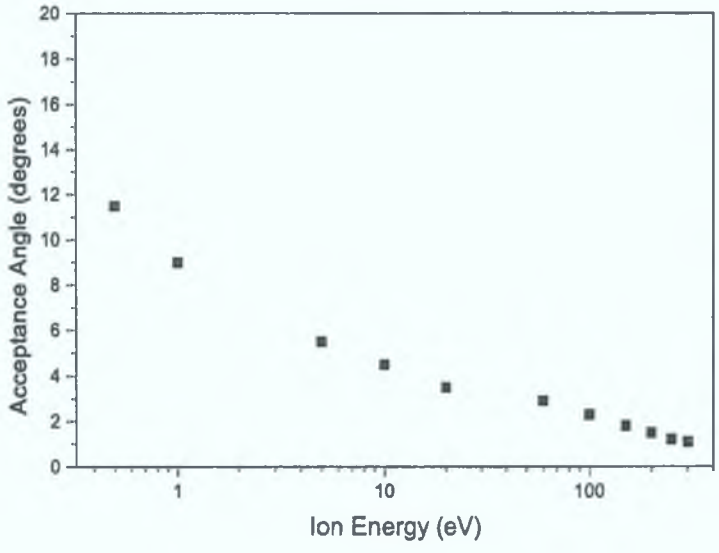

Figure 3.6: *Acceptance Angle as a function of Ion Energy (Scanning Energy)*

acceptance angle possible. The voltage on *lens 1* is limited to -375 V by the instrument, therefore the largest values that could be used were *extractor* = -40 V, *lens 1* = -315 V, *axis* = -40 V and *flight-focus* = -89 V. As before, the acceptance angle is larger for lower energy ions reflecting the fact that lower energy ions are deflected more towards the optical axis. However, the curve is a smooth function. There are no extra peaks as in figure 3.4. This illustrates that for these settings no chromatic aberration effects are present in the instrument.

In order to ascertain the reliability of the method another check was made. All the electrodes in the system were set to the same voltage, the pass energy of the energy analyser, -40 V, and the energy distribution measured. For this case, only ions within some geometrical acceptance angle are detected. There are no focusing effects and hence no distortion of the IEDF can occur. There will be a dramatic loss in the signal intensity as only a very small fraction of the ions entering the EQP will be detected. However a true representation of the IEDF in the forward direction will be obtained. Figure 3.7 shows two measured distributions of the H_3^+ ion. The black line is the measured IEDF with all electrode voltages

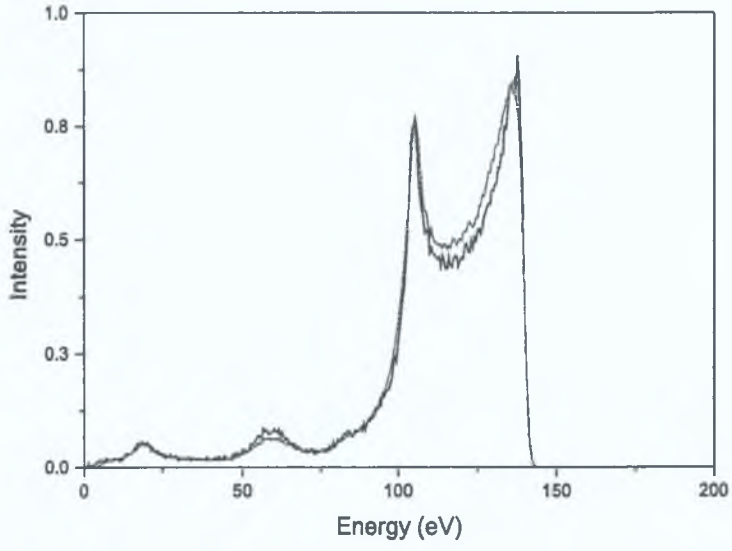

Figure 3.7: *Comparison of normalised IEDFs for H_3^+ ion with (gray line) and without (black line) focusing effects*

set to -40 V with no focusing effects. The gray line shows the case when the voltage settings, which do not exhibit chromatic aberration effects, found using SIMION are applied to the electrodes. The H_3^+ ion is the most dominant in the hydrogen discharge and also has the narrowest angular distribution. It can therefore be detected even without focusing using electrostatic lenses. The shapes of the distributions compare very well. This gives reassurance in the SIMION simulations and the technique used.

As discussed in the previous section 1.5 there are also several other electrodes in the EQP not causing energy discrimination. The values of the potentials on these electrodes were chosen so as to increase the signal to noise ratio while ensuring that the shape of the distribution function did not change.

Scanning options

In order to make an ion energy scan the voltages on each of the electrodes are scanned in a specific manner. This was briefly described above. The Hiden recom-

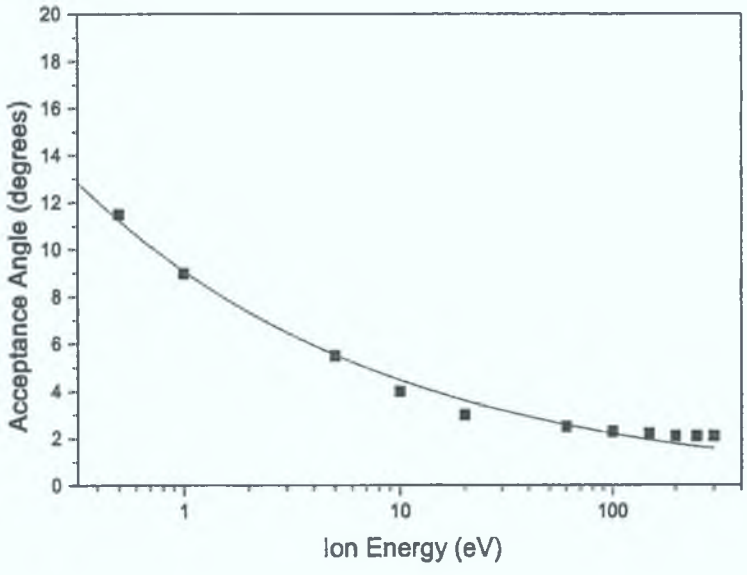

Figure 3.8: *Acceptance Angle as a function of Ion Energy (Scanning Reference)*

mended scanning option is scanning the parameter *Energy* (see figure 3.1). This is equivalent to a simultaneous scan of the *axis* and *lens 2* electrodes. However, it was found that this is not the best scanning option. While the effects of chromatic aberration could be avoided it was not possible to sustain a uniform transmission (figure 3.6). Another scanning option available is scanning the parameter *Reference* while keeping *energy* at constant 0 V. All the electrodes of the system float on the *Reference* potential and this is therefore equivalent to scanning *Energy*, *extractor*, and *lens 1*. Figure 3.8, illustrates that *Reference* scanning results in a uniform acceptance angle above 50 eV. The acceptance angle is larger for lower energy ions reflecting the fact that lower energy ions are deflected more towards the optical axis. Scanning *Reference* also results in a slightly larger acceptance angle than *Energy* scanning (figure 3.6). Thus, the scanning option, *Reference*, was chosen. Another advantage of using the *Reference* scanning is that the power supply for *Energy* is limited to a range of 200 V. Therefore, when scanning *Energy* for ion energy scans broader than 200 eV the scan must be split into two separate scans.

3.3 Comparison to PIC simulations

Results are compared to a 2-Dimensional Particle-In-Cell (2D PIC) simulation taking the specific geometry of the experiment into account [62]. It is crucial that both the simulation and experiment sample the same quantities.

The signal detected by the EQP is proportional to the ion flux emanating from the sampling aperture therefore the simulation samples the ion flux impacting on the grounded electrode. The EQP actually measures the velocity distribution and thus experimental results are compared to the velocity distribution in the simulation.

In order to make accurate comparisons to the PIC simulations several affects must be accounted for. The affect of collisions in the EQP is considered and discussed below. Also, knowledge of the acceptance angle in the experiment is important. Not all ions arriving at the grounded electrode can be detected by the EQP. The angle of incidence at the electrode determines whether an ion can reach the detector. Two limiting factors are the orifice geometry (section 3.3.2) and also the voltage settings on the electrostatic lenses in the EQP (section 3.3.3).

The effect of collisions after ions pass the sampling orifice as they traverse the EQP is discussed in section 3.3.1. Other affects of the instrument which influence the results are the transmission functions caused by the sampling orifice and the ion optics. These result in the EQP only measuring a very narrow angular distribution. From this measured distribution the total angular distribution can not be interpreted. However, using the angular energy distribution computed in the simulation and knowing the transmission functions of the instrument the experimentally measured distribution function can be determined from the simulation results. The transmission functions applied to the PIC simulations results are presented below. Two transmission functions are considered; that due to the sampling orifice geometry and due to the ion optics. The sampling orifice in the electrode, due to its finite thickness, will result in a transmission function. This function is calculated and presented below. Also, the settings on the ion optics will produce an energy dependent transmission. The strength of the electric field,

thus the settings on the electrostatic lenses, just inside the EQP will effect the acceptance angle of the instrument. This transmission function is also determined below (section 3.3.3).

3.3.1 Extraction effects

Ions can undergo collisions after passing through the sampling orifice due to either the static background pressure in the ion analyser or the expanding gas, from the plasma chamber, through the orifice. Based on the work of Coburn and Kay [81, 83], the attenuation of the ion beam downstream of the orifice is calculated. The static background pressure, due to efficient pumping in the EQP, is sufficiently low that the mean free path is of the order of several meters. Therefore, scattering of the ions by collisions with the neutral species which constitute the background gas is insignificant. However, the expanding gas from the orifice forms a localised high gas density downstream of the orifice, which varies significantly with the chamber pressure and orifice diameter, and is independent of the pumping speed in the low-pressure region. According to Coburn and Kay [81], the fraction of ions reaching the detector without collisions can be expressed by

$$\frac{I(l)}{I_0} = exp\left[-\frac{\sigma n_0 R}{2}\tan^{-1}\left(\frac{l}{R}\right)\right] \tag{3.1}$$

where $I(l)$ is the ion current at a distance l from the orifice, I_0 is the current at the orifice, σ is the collision cross section, n_0 is the neutral density on the upstream side of the orifice, and R is the orifice radius.

For $R_{orifice} = 5\,\mu m$, $l = 5cm$, $\sigma = 1.0{\cdot}10^{-15}\,cm^{-2}$ (H_2 charge exchange, 20 eV) it was calculated for the 10 μm orifice used that, even at a high chamber pressure of 70 Pa, less than 1 % of the ions undergo collisions due to the neutral species which effuse through the orifice. Thus, it is anticipated that ion-neutral collisions downstream of the orifice do not significantly distort the IEDF.

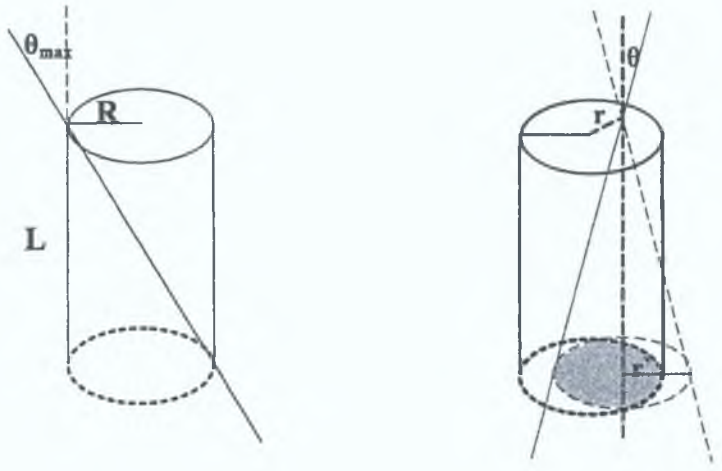

Figure 3.9: *Orifice Geometry*

3.3.2 Orifice transmission function

The finite thickness of the sampling orifice requires correction of the IEDF. Not all ions impacting on the orifice will reach the opposite side and be sampled by the ion optics of the EQP. A cylindrical aperture, such as a pinhole, of radius R and length L is considered (figure 3.9). The probability that a particle will pass through the aperature will depend on the angle it arrives and the arrival position. Consider a flux of particles evenly distributed over one entrance of the aperture. The fraction of ions which passes through the cylinder without colliding with the walls was calculated. The angle between the particle trajectory and the axis of the orifice is defined as θ, and the arrival position is defined by the radial coordinate, r. There is a maximum value of θ beyond which transmission is impossible, which is given by

$$\tan\theta_{max} = \frac{2R}{L} \tag{3.2}$$

A particle that arrives at the entrance of the aperture at angle, θ and radial coordinate, r is considered. The particle trajectory lies in the surface of a cone, which at the exit aperture has radius $r' = L\tan\theta$. The fraction of the incoming particles that are transmitted will be the fraction of the circumference of the cone

that lies within the exit aperture of the orifice (figure 3.9(b)). This is given by

$$\frac{\phi}{\pi} = \cos^{-1}\left(\frac{r^2 + L^2\tan^2\theta - R^2}{2rL\tan\theta}\right)/\pi \tag{3.3}$$

$$= \cos^{-1}\left(\frac{\rho^2 + \psi^2 - 1}{2\rho\psi}\right)/\pi \tag{3.4}$$

where $\rho = r/R$ and $\psi = 2\tan\theta/\tan\theta_{max}$. The transmission probability can now be defined by

$$T(\psi) = \int_0^{1-\psi} 2\rho d\rho + \int_{1-\psi}^{1} 2\rho d\rho \frac{\phi}{\pi} \quad \psi < 1 \tag{3.5}$$

$$= \int_{\psi-1}^{1} 2\rho d\rho \frac{\phi}{\pi} \quad \psi \geq 1 \tag{3.6}$$

Calculating these integrals numerically gives an approximation of

$$T(\psi) = 1 - \frac{1}{2}\psi \tag{3.7}$$

$$T(\theta) = 1 - \frac{L}{2R}\theta \tag{3.8}$$

The orifice dimensions considered are diameter, 10 μm and length, 25 μm. Figure 3.10 shows the transmission of the 10 μm sampling orifice used as a function of incidence angle. The ions sampled in the simulation are weighted, according to incident angle, using this function.

3.3.3 Energy transmission function

The ion optics of the EQP causes an energy-dependent transmission. The strength of the electric field, thus the settings on the electrostatic lenses, just inside the EQP affect the acceptance angle of the instrument. As discussed in section 3.2 the acceptance angle of the instrument is energy dependent. This arises due to the narrow acceptance angle of the ion optics. This acceptance angle is a good approximation of the energy dependence of the instrument. Figure 3.8 shows the

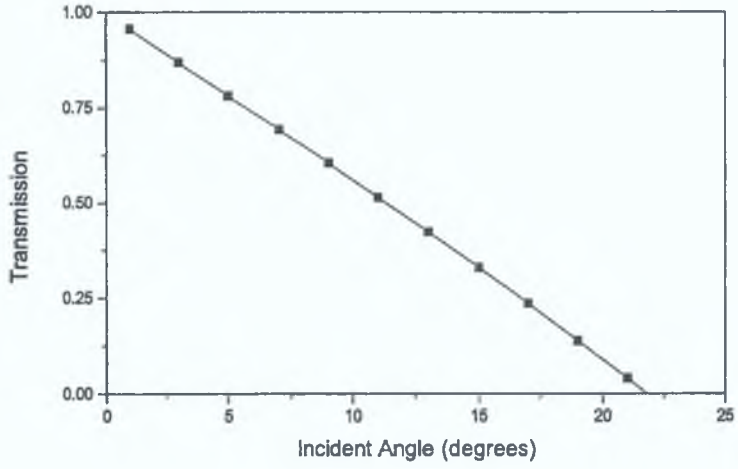

Figure 3.10: *Orifice transmission probability as a function of incidence angle*

acceptance angle calculated using SIMION for the lens settings used and also a fit to the data. The acceptance angle decreases with energy and is quite narrow ($\sim 2.5^0$) for ion energies above approximately 50 eV. This reflects the fact that low energy ions are easier to deflect and focus. The energy dependence will contribute to an artificial distortion of the IEDF especially in the low-energy region. The energy dependent transmission function, $T(E)$, for the settings used is found to be

$$T(E) = 9.1 \left(\frac{E}{eV} \right)^{-0.3} \tag{3.9}$$

where E is the ion energy. This function is also applied to the simulation results for comparison to the experimental data. The bottom line is, that for ion energies below ~ 20 eV it is difficult to compare the measured IEDF to the simulated IEDFs. For the IEDF measurements made here the high ion energy range is of most interest. However the low energy range is also important for comparing the total ion fluxes. In this case where the total ion fluxes are required all ions are important irrespective of energy. However, for comparing the total fluxes another aspect must be considered that is the mass transmission function for the instrument. Both the quadrupole mass filter and the SEM detector will contribute

to a mass transmission function. This function is difficult to determine but is possible by calibrating the ion resolved mass spectrometer to a retarding field analyser using nobel gases. This however is difficult for the case of light ions and can only be approximated for ions of mass less than 3 amu.

In this work an alternative approach has been developed to calibrate the EQP for measuring absolute fluxes. This calibration procedure is described in detail in section 4.2.

CHAPTER 4

Single frequency rf sheath results

Understanding the dynamics of the sheath formed at a substrate immersed in an rf plasma is important from both a fundamental and technological point of view. Ion energy distribution functions provide important information about the ion dynamics within the sheath. There have been previous experimental and numerical investigations of IEDFs in rf discharges. However, most of these have been restricted to discharges with heavier ions, such as Argon [84, 85, 86, 51, 88, 89, 90]. In order to probe the dynamics of rf sheaths at typical processing frequencies (eg. 13.56 MHz) light ions, such as hydrogen ions, are better suited. The ions can respond to the oscillations of the sheath electric field and the IEDFs will thus reflect the time-dependent sheath potential. The experimental set-up is a confined symmetric plasma with approximately equal sheath voltages on both electrodes (chapter 2). A comparison to the experimental results is made with a 2D PIC simulation[1] [62] which exactly simulates the experimental system (chapter 3). The experiment is used to benchmark the simulation which can then be used for further detailed investigations under conditions which are difficult or impossible experimentally. Hydrogen is also a very suitable discharge gas for

[1] 2D PIC simulation code was developed by R. Zorat

comparing to simulations, since it is the simplest molecular gas and has the most extensive collision cross-sectional data set available. Deuterium and its mixtures with hydrogen are investigated for deeper insight into the complex chemistry in the plasma and the sheath.

Determining the absolute flux using mass resolved ion energy analyser is an important but complicated task. A satisfactory method is highly sought after. To date, retarding field analysers have been used to calibrate mass resolved ion energy analysers for flux determination. A much simpler novel approach for the estimation of the absolute flux from the IEDFs measured has been developed and is discussed.

The most interesting results for hydrogen and deuterium single frequency discharges and their mixtures are presented and discussed in this chapter. Additional results are shown in the appendix.

4.1 Sheath voltage

The ion impact energy at the electrode is determined by the potential difference ions fall through on traversing the sheath. Thus, the sheath potential is a crucial parameter influencing the IEDF. A description of an rf sheath model [34], in a symmetric discharge, was described in section 1.2.5 and the sheath voltage waveform, as determined from the model, was shown in figure 1.6. A typical result for an IEDF of ions coming from the plasma bulk, traversing a collisionless sheath in the intermediate frequency regime is shown in figure 4.1. The IEDF reflects the acceleration of ions by the electric field of the oscillating plasma sheath and thus the time dependence of the sheath potential. Therefore, peaks in the energy distribution can be expected where the time derivative of the potential is zero. Consequently, the IEDF at the electrode, will be characterised by a saddle-shaped structure consisting of two peaks centered around the time-averaged sheath potential [37]. When an ion can perfectly respond to the rf field, the two peaks correspond to the maximum and minimum sheath potential. However, as the

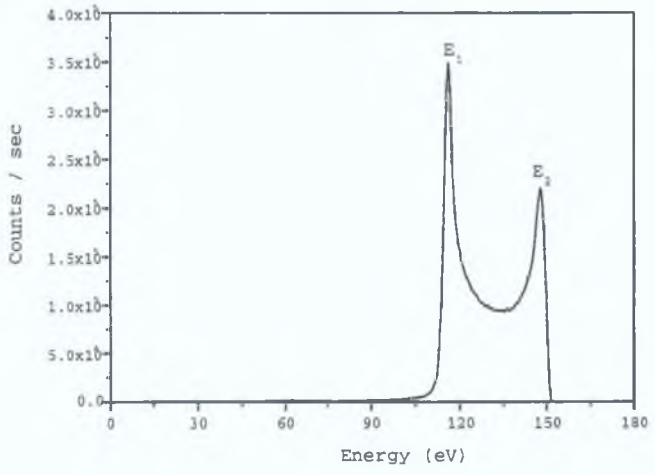

Figure 4.1: *A typical IEDF for ions coming from the bulk plasma traversing a collisionless sheath in the intermediate frequency regime*

ion transit time across the sheath increases, the peaks of the IEDF are no longer located at the maximum and minimum voltage. The peaks corresponding to the extrema move closer together and the separation decreases. The peak separation depends on time averaged sheath voltage, sheath width, frequency and mass [41].

The time-averaged sheath voltage, V_{sheath}, can be determined from the center of the two peaks in the IEDF

$$eV_{sheath} = \frac{E_1 + E_2}{2} \tag{4.1}$$

where E_1, is the energy of the low energy peak and E_2, the energy of the high energy peak. The peak separation, ΔE, is defined as $\Delta E = E_2 - E_1$.

The discharge is a confined symmetric discharge with approximately equal potential drops on both the powered and grounded electrode. Therefore, the time-averaged sheath potential, V^*_{sheath} , for a purely sinusoidal sheath voltage waveform, on the grounded electrode can be approximated by

$$V^*_{sheath} = \frac{V_{p-p}}{4} \tag{4.2}$$

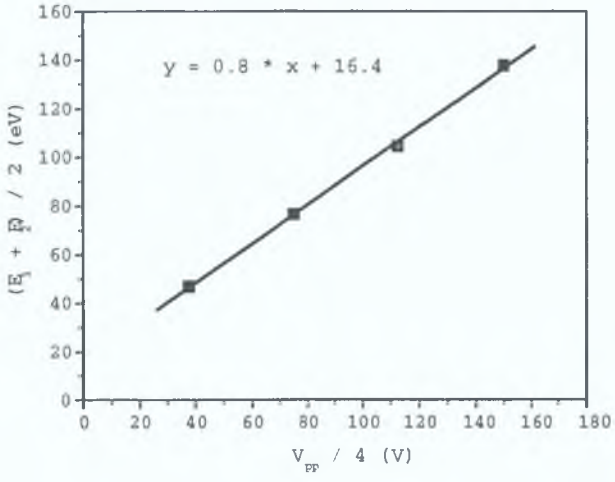

Figure 4.2: *Sheath potential*

where V_{p-p} is the applied peak-to-peak voltage at the powered electrode. The rf sheath potential, at the grounded electrode, thus oscillates between a minimum potential equal to zero and a maximum potential equal to $\frac{V_{p-p}}{2}$. Since hydrogen ions only partially follow this oscillation, at the frequency of 13.56 MHz and 27.12 MHz investigated, the peaks in the bi-modal structure corresponding to the extrema of the sheath voltage move closer to each other. Figure 4.2 shows a plot of the sheath potential determined from the IEDF, using equation 4.1, as a function of the sheath potential determined from the applied peak-to-peak voltage, using equation 4.2.

The slope of the graph is just below 1. However several things affect accurately calculating the sheath potential on the grounded electrode from the measured voltage on the powered electrode, such as, a non-purely capacitive sheath, dc-bias, field reversal and losses in the transmission line between the point of measurement and the electrode. Therefore measuring the sheath potential using the IEDF is more accurate and this method will be used in the following.

4.2 Calibration for measuring absolute fluxes

The task of determining absolute fluxes using mass resolved ion energy analysers is an important but very complicated one. This section describes a novel technique which has been developed for estimating absolute fluxes. An estimation of the absolute flux of ions impacting on the electrode is possible from, the variation of peak splitting, in the bi-modal structure of the IEDF, as a function of sheath voltage. As discussed above the separation increases with increasing time-averaged sheath voltage.

The separation of the peaks, ΔE, can be characterised using the following equation [41].

$$\Delta E = \frac{8e\widetilde{V_s}}{3s\omega}\sqrt{\frac{2e\overline{V_s}}{M}} \tag{4.3}$$

where V_s is the time-averaged sheath voltage, s the sheath width, ω the frequency and M the ion mass. The scaling of peak separation with sheath voltage was checked in the simulation and the agreement with equation 4.3 is very good.

The simple rf sheath model [34], described in section 1.2.5, is good for explaining the basic phenomena. However, for a quantitative calculation the sheath thickness from a more realistic rf sheath model is used [25]. The rf sheath thickness is larger than the Child law sheath thickness by a factor of $\sqrt{\frac{50}{27}}$. This increase is due to the reduction of space charge within the sheath due to the nonzero, time-average electron density. Taking the Child law sheath thickness, equation 1.21, the rf sheath thickness becomes

$$s = \sqrt{\frac{50}{27}}\frac{\sqrt{2}}{3}\lambda_{De}\left(\frac{2eV_0}{kT_e}\right)^{3/4} \tag{4.4}$$

with the Debye length, $\lambda_{De} = \sqrt{\frac{\varepsilon_0 kT_e}{e^2 n}}$. Equation 4.4 compares well to the results of the 2D PIC simulations. Inserting the sheath width, s, into equation 4.3 gives the following

$$\Delta E = 3.496\frac{e^2\widetilde{V_s}}{\omega}\left(\frac{n}{\varepsilon_0 M}\right)^{1/2}\left(\frac{kT_e}{e\overline{V_s}}\right)^{1/4} \tag{4.5}$$

Due to flux conservation within the sheath, the flux at the electrode is equal to the flux at the sheath edge, which is given by

$$\Gamma = u_B n \tag{4.6}$$

where n is the density at the sheath edge and $u_B = \sqrt{\frac{kT_e}{M}}$ is the Bohm velocity. From this the density is obtained

$$n = \Gamma \left(\frac{M}{kT_e} \right)^{1/2} \tag{4.7}$$

Inserting the density into equation 4.5 gives the following relationship for the absolute flux

$$\Gamma = \frac{\varepsilon_0 \omega^2}{12.22} \sqrt{\frac{M}{(eV)^3}} \left(\frac{\Delta E}{e} \right)^2 \tag{4.8}$$

The electron temperature cancels out and the absolute flux impacting on the electrode can now be determined. Using the following relationship between the absolute flux, Γ, and the measured flux, $\Gamma_{measured}$,

$$\Gamma = C\Gamma_{measured} \tag{4.9}$$

the calibration factor, C dependent on the instrument, can be determined.

The above method assumes a single ion species plasma boundary sheath. Hydrogen discharges consists of three ion species, H^+, H_2^+ and H_3^+. Later it will be observed that the H_3^+ ion flux, at the electrode, dominates at low sheath voltages. It will also be shown that the H_3^+ ion flux, at the electrode, is more dominant in discharges excited at 27.12 MHz than at 13.56 MHz. The conditions under which equation 4.3 is best fulfilled is for small peak separation of the bi-modal structure [7, 41]. From equation 4.3, small peak separation also occurs for low sheath voltages. However, at the lowest sheath voltage the peak separation cannot be accurately resolved. Therefore, the conditions under which the calibration is performed are, 27.12 MHz discharge at 5 Pa and time-averaged sheath voltage of 77 V. Using these conditions the calibration factor for hydrogen is determined

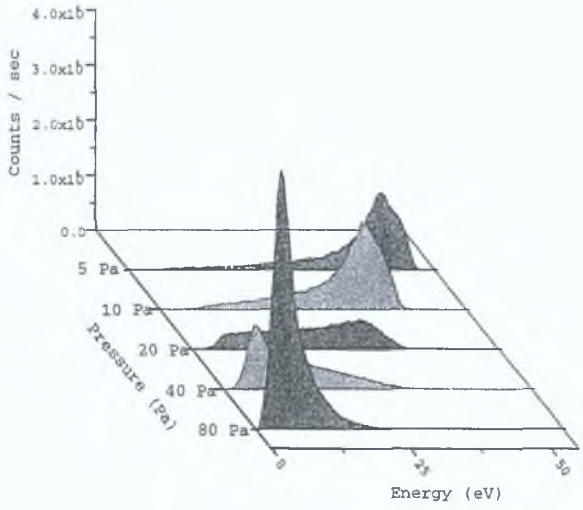

Figure 4.3: *H_3^+ IEDF in a 13.56 MHz hydrogen discharge, $V_{sheath} = 47\,V$ for various pressures*

to be $8.12 \cdot 10^{11} m^{-2} counts^{-1}$. Since both the quadrupole and the detector in the mass resolved ion energy analyser are mass dependent a separate calibration factor is determined for deuterium (section 4.5).

4.3 Hydrogen discharge at 13.56 MHz

Pressure Variation

In a hydrogen discharge three ion species are investigated, H^+, H_2^+ and H_3^+. Figure 4.3 shows a pressure variation of the H_3^+ IEDF at a time averaged sheath voltage of 47 V. In the bulk plasma H_2^+ ions are created by electron impact ionisation of neutral gas molecules. These are readily converted into H_3^+ ions through collisions with the background gas. Most ions entering into the sheath region from the bulk plasma are H_3^+ ions. At 5 Pa, the sheath is essentially collisionless, ions enter the sheath directly from the bulk plasma and are accelerated through the entire sheath potential. This is apparent from the single peak positioned at the time-averaged sheath potential. The splitting of this peak, discussed in the previous section, cannot be clearly observed as the voltage is too low, this is dis-

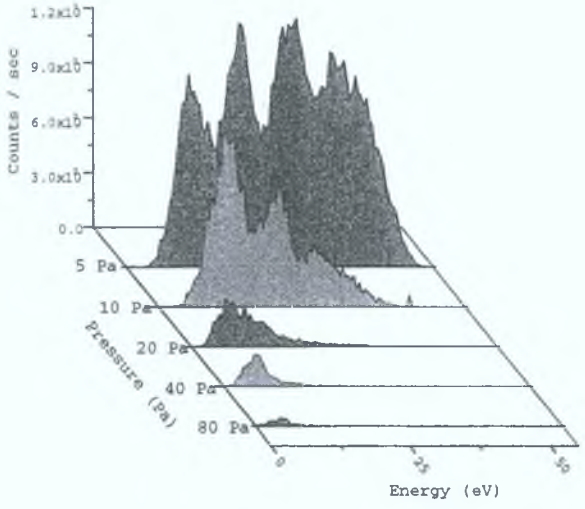

Figure 4.4: *H_2^+ IEDF in a 13.56 MHz hydrogen discharge, $V_{sheath} = 47\,V$, for various pressures*

cussed in more detail below. As the pressure increases and the sheath becomes more collisional ions travelling through the sheath will collide mainly with the background neutral gas. Ion-neutral collisions in the sheath result in momentum and energy transfer both broadening and moving the distribution to lower energies. At 80 Pa the IEDF takes on an exponential function as discussed in chapter 1.

Figures 4.4 and 4.5 show the IEDFs of H_2^+ and H^+, respectively, with varying pressure at a time-averaged sheath voltage of 47 V. Unlike H_3^+ ions at 5 Pa, which mainly enter the sheath from the bulk plasma, H^+ and H_2^+ ions impacting on the electrode, are mainly created in the sheath. H_3^+ ions can be destroyed in collisions with background gas molecules at energies in excess of about 10 eV. Therefore, after acceleration by the sheath electric field H_3^+ can be converted into H^+ and H_2^+. The average energy of H^+ and H_2^+ ions, in figure 4.4 and 4.5, is significantly lower than the time-averaged sheath voltage, indicating that they are not accelerated through the entire sheath potential but are created in the sheath experiencing only a fraction of the maximum sheath potential. The H_2^+ IEDF is strongly influenced by symmetric charge-exchange collisions. Fast H_2^+

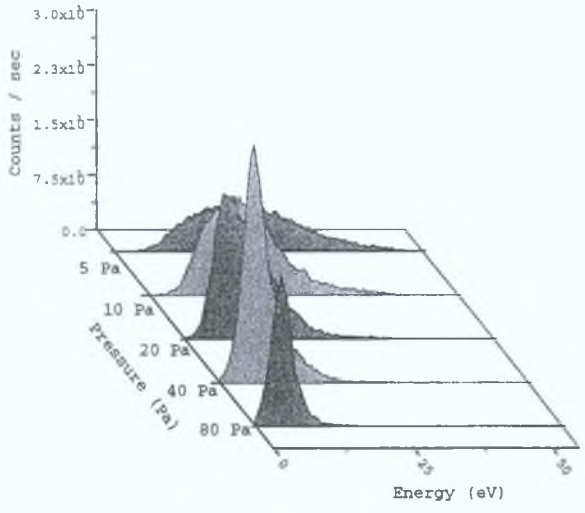

Figure 4.5: *H^+ IEDF in a 13.56 MHz hydrogen discharge, $V_{sheath} = 47\,V$, for various pressures*

ions collide with the background gas and produce slow H_2^+ ions and fast neutrals. The newly created thermal H_2^+ ions are accelerated toward the electrode by the sheath electric field. These ions do not experience the full potential drop of the sheath and appear as structures in the IEDF at lower energies than the time-averaged sheath potential. The energies of the secondary peaks depend on the sheath position at which the slow ions were formed [38]. The number of peaks in the distribution corresponds to the number of rf cycles it takes the ions to cross the sheath. The H^+ IEDF at high pressures goes into the exponential function described in section 1.2.4.

As mentioned earlier in order to obtain more details about the ion dynamics in the sheath a comparison to a simulation is made. The experiment is used to benchmark a 2D PIC simulation which can then be used for further detailed investigations. Benchmarking in this pressure regime is not possible for H^+ and H_2^+ since the signal to noise ratio is too low. However for the dominant H_3^+ ion it is possible. Figure 4.6 shows that even under the most complicated conditions, of 20 Pa, the experiment and simulation agree very well. At 20 Pa, the sheath is not completely collisionless but not completely collision dominated either. In this

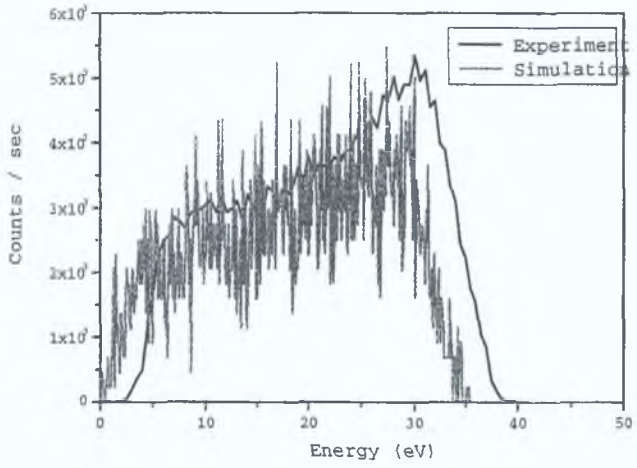

Figure 4.6: *H_3^+ IEDF in 13.56 MHz hydrogen discharge at 20 Pa and $V_{sheath} = 47\,V$; experiment and simulation*

transition regime both experiment and simulation show similar effects of elastic scattering of H_3^+. The IEDF resulting from the simulation is at slightly lower mean energy. This arises since the applied voltage in the simulation is twice the time-averaged sheath voltage at the grounded electrode in the experiment. Since the simulation is a 2D PIC it shows a dc bias on the powered electrode, and the potential drop across the grounded electrode is slightly less than across the powered electrode.

Figure 4.7 shows the flux of each of the three ion species, H^+, H_2^+ and H_3^+, relative to the total flux as a function of pressure. Due to the unknown mass transmission function, an accurate comparison between each of the three ions cannot be made. However, an approximate comparison shows that the main flux contribution is H_3^+. From 5 Pa to 10 Pa there is a sharp rise in the H_3^+ relative flux with a corresponding drop in the H_2^+ relative flux, and at 20 Pa the flux contribution of H_2^+ is negligible. With increased pressure, and neutral gas density, it might be expected that H_3^+ ions entering from the plasma bulk are more efficiently converted to H^+ and H_2^+ through collisions with the background gas. However, as can be observed in figure 4.7, this is not the case. H_2^+ formation

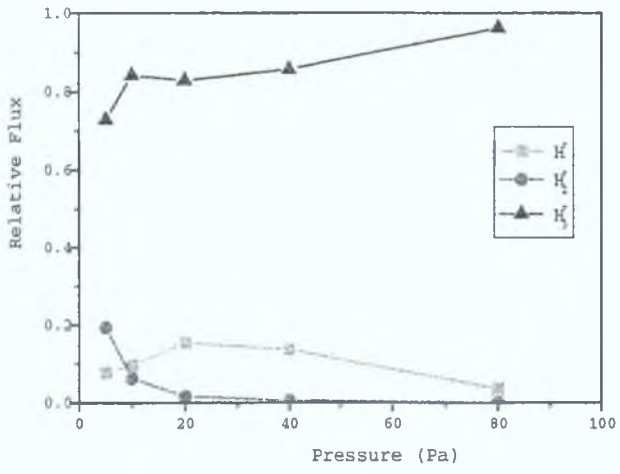

Figure 4.7: *Relative Fluxes of H^+, H_2^+ and H_3^+ in a 13.56 MHz hydrogen discharge, $V_{sheath} = 47\,V$, as a function of pressure in experiment*

in the sheath is mainly from H_3^+ ions, with energies greater than $8\,eV$, undergoing either collision induced dissociation (CID) or asymmetric charge transfer (ACT) with the background neutral gas. At 5 Pa, H_3^+ ions have an energy in the range 35 eV - 52 eV, where the cross-section for both CID and ACT to H_2^+ is of the order of $0.5 \cdot 10^{-20} m^2$, and H_3^+ ions are efficiently converted into H_2^+. The cross-sections for both CID and ACT processes sharply decrease as H_3^+ energy decreases. As the pressure increases, the mean energy of H_3^+ ions decreases leaving less H_3^+ ions eligible for conversion to H_2^+. At 40 Pa most H_3^+ ions have shifted to an energy below the threshold energy, 8 eV, for conversion to H_2^+. Therefore as pressure increases, and H_3^+ energy decreases they can no longer be converted into H_2^+. This results in an increase in the H_3^+ ion flux and a decrease in the H_2^+ ion flux.

H^+ ion flux increases from 5 Pa to 20 Pa and a further increase in pressure, to 80 Pa, results in a drop in H^+ ion flux. The dominant H^+ formation process in the sheath is CID of H_3^+ with the background gas. The cross-section for CID to H^+ is greatest for H_3^+ ions of $\sim 20\,eV$. From figure 4.3, at 5 Pa, the mean H_3^+ energy is at $\sim 40\,eV$. As discussed above, as the pressure increases, H_3^+ ion energies decrease and the greatest flux of 20 eV H_3^+ ions occurs at 20 Pa. Therefore the

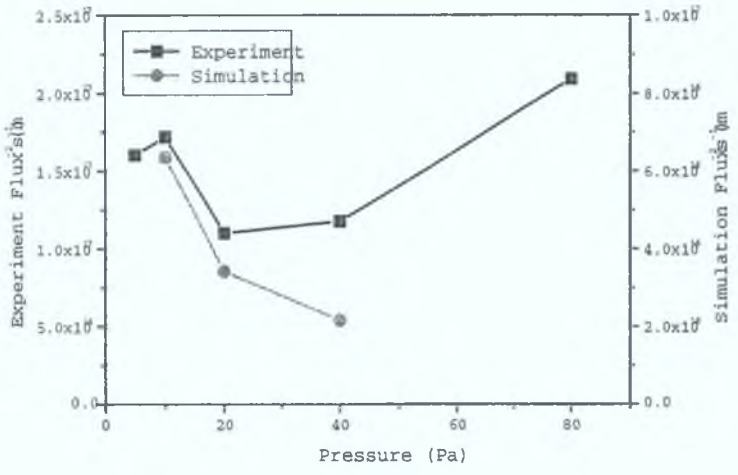

Figure 4.8: *Total ion flux in experiment and simulation, at grounded electrode surface, in a hydrogen discharge at 13.56 MHz and* $V_{sheath} = 47\,V$ *as a function of pressure*

conversion of H_3^+ into H^+ will be the most efficient at 20 Pa corresponding to the peak in H^+ ion flux at 20 Pa. At 80 Pa, H_3^+ IEDF has shifted to lower energies with a peak energy at 4.5 eV, below the threshold for CID to H^+, of 5 eV. At 80 Pa, H_3^+ ions have gone below the threshold for conversion to both H^+ and H_2^+ and can only undergo momentum transfer with the background gas. This is reflected in the negligible H^+ and H_2^+ flux in figure 4.7.

The absolute fluxes, impacting on the grounded electrode, in both the experiment and simulation are shown in figure 4.8, for the same conditions as figure 4.7. The calibration technique for determining the absolute fluxes in the experiment is discussed in section 4.2. The trend in relation to pressure agrees very well in the experiment and simulation. The absolute flux in the experiment is slightly greater than in the simulation. These discrepancies indicate lower plasma density in the simulation. Variations in flux can be due to either velocity or density at the sheath edge. At low pressures the mean energy and thus velocity is higher than at high pressures. This gives rise to higher fluxes at low pressures.

In order to distinguish between effects due to the mean energy of the distribution function and densities an estimation of the density at the surface of the

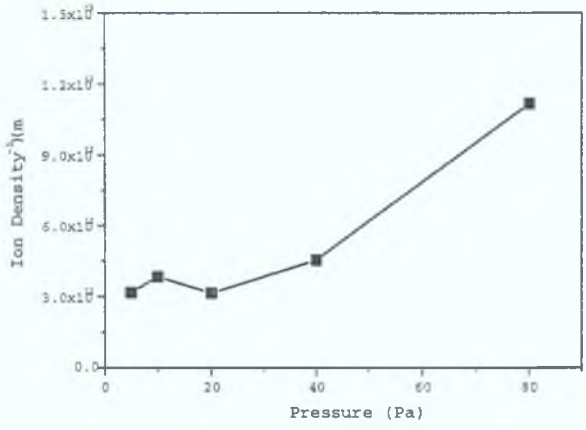

Figure 4.9: *Ion density at electrode surface in a hydrogen discharge at 13.56 MHz and* $V_{sheath} = 47\,V$ *as a function of pressure in experiment*

grounded electrode is made. To compare densities the flux distribution is divided by $\sqrt{\frac{2E}{M}}$. Figure 4.9 shows a plot of the total density at the grounded electrode, at 47 V, as a function of pressure. As the pressure increases the density increases. This signifies more efficient ohmic heating at increased pressures [1].

Voltage variation

Figure 4.10 shows the H_3^+ IEDF, at 5 Pa, for varying sheath voltages. As already discussed above the contribution due to collisions can be assumed to be minimal at this pressure. Equation 1.44 predicts that, as the sheath potential increases, the separation of the peaks in the saddle structure increases. This is reflected in figure 4.10. At a time-average sheath voltage of 47 V the two peaks cannot be resolved and the splitting is not observed. As the sheath voltage increases the bi-modal structure of the IEDF becomes noticeable. This is explained in detail in section 1.3. The lower energy peak of the bi-modal structure is preferred. This is due to the non-sinusoidal nature of the sheath voltage. In figure 1.5 it was observed that the minimum of the sheath potential on the grounded electrode is slower varying than the maximum. Thus more ions enter into the sheath during this voltage phase and contribute to the low energy peak of the bi-modal structure.

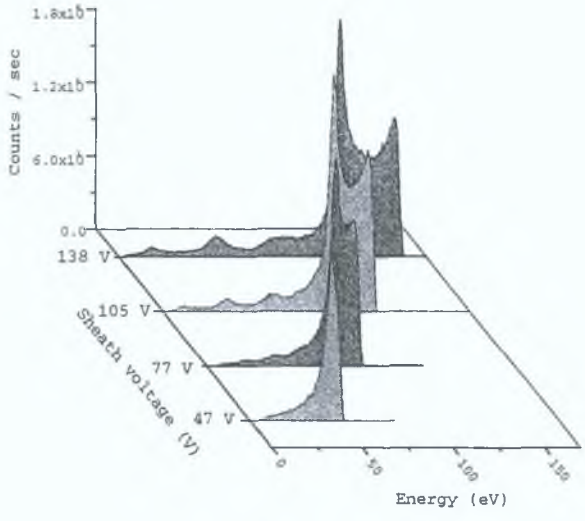

Figure 4.10: *H_3^+ IEDF in a 13.56 MHz hydrogen discharge at 5 Pa for varying sheath voltages in experiment*

At higher sheath voltages some contribution due to collisions becomes noticeable through structures at low energies in the distribution. These are produced from the exothermic conversion reaction of slow H_2^+ ions and H_2 neutrals. This is the same process which readily converts H_2^+ into H_3^+ in the plasma bulk. The cross-section for this process is high ($\sim 10 \cdot 10^{-20}\, m^2$) for thermal H_2^+ ions. Therefore the collision probability is high after symmetric charge exchange between H_2 and H_2^+ has taken place.

The H_2^+ IEDF, for the same conditions as in figure 4.10, is shown in figure 4.11. The IEDF exhibits typical secondary structure indicative of ion formation in the sheath through symmetric charge-exchange. The separation of the secondary peaks increases with increasing sheath voltage, as with the peaks in the bi-modal structure of the H_3^+ IEDF.

The H^+ IEDF, for the same conditions as in figure 4.10, is shown in figure 4.12. The H^+ mean energy is at lower energies than the time-averaged sheath voltage indicating that they are not accelerated through the entire sheath potential but created in the sheath and thus only experience a fraction of the maximum sheath potential. As discussed in section 1.4, H^+ and H_2^+ are mainly created in the

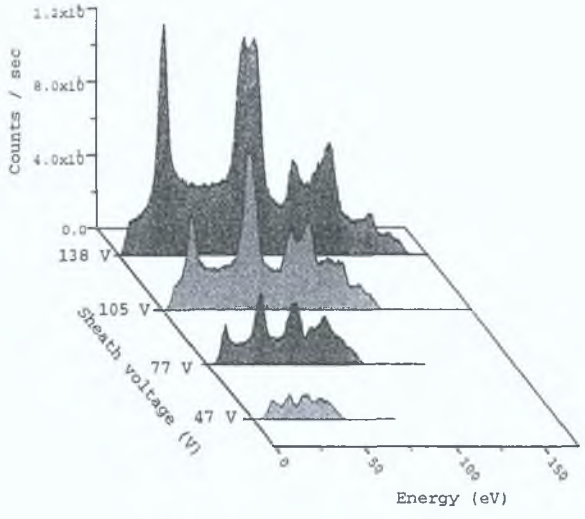

Figure 4.11: *H_2^+ IEDF in a 13.56 MHz hydrogen discharge at 5 Pa for varying sheath voltages in experiment*

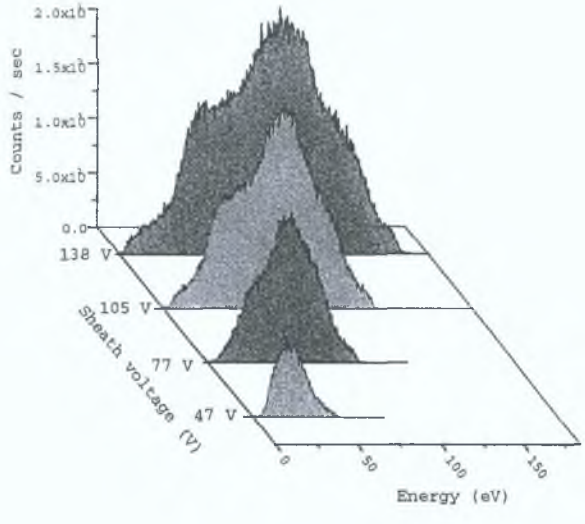

Figure 4.12: *H^+ IEDF in a 13.56 MHz hydrogen discharge at 5 Pa for varying sheath voltages in experiment*

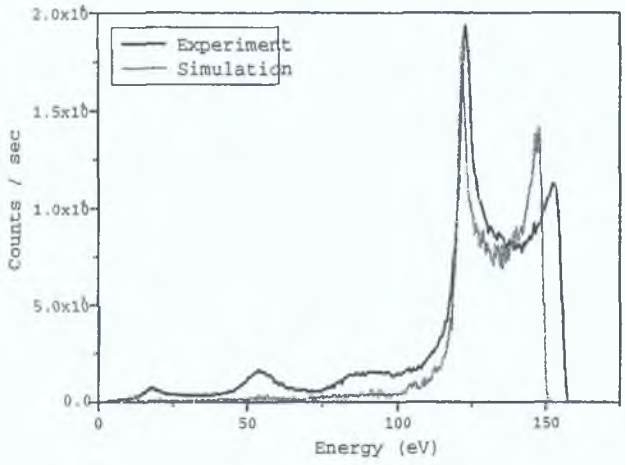

Figure 4.13: *H_3^+ IEDF in 13.56 MHz hydrogen discharge at 5 Pa and $V_{sheath} = 138\,V$; experiment and simulation*

sheath from H_3^+ ions undergoing collisions with the background gas.

For the conditions considered here at higher voltages and thus higher densities it is possible to benchmark the H_3^+ and H_2^+ IEDF with the simulation. However, as the case in the pressure variation the signal to noise ratio in the H^+ IEDF is still poor. A comparison of experiment and simulation, at 5 Pa, for a time averaged sheath voltage of 138 V for H_3^+ and H_2^+ is shown in figures 4.13 and 4.14, respectively. The simulation data is normalised to the experimental data. The agreement between experiment and simulation is generally very good. However, there are slight discrepancies. The H_3^+ IEDF from the simulation is at slightly lower mean energy due to the dc-bias as explained earlier. Also, the splitting in the simulation is smaller than in the experiment. This is partly due to the lower sheath voltage, but also hints to a wider sheath which corresponds to a lower density. This smaller density in the simulation was also observed in figure 4.8. The number of secondary peaks in the H_2^+ IEDF corresponds to the number of rf cycles it takes to cross the sheath [38] and is thus proportional to the sheath width. There are more secondary peaks in the H_2^+ IEDF of the simulation, signifying a larger sheath width and thus lower density.

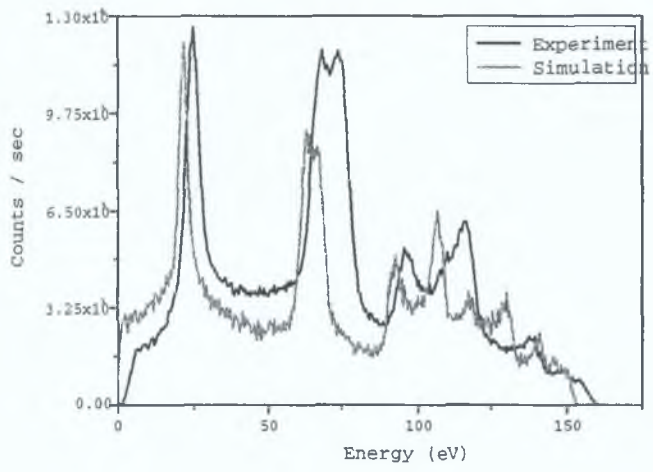

Figure 4.14: *H_2^+ IEDF in 13.56 MHz hydrogen discharge at 5 Pa and $V_{sheath} = 138\,V$; experiment and simulation*

Figure 4.15 shows the ratio of the flux of each ion relative to the total flux, in a 13.56 MHz hydrogen discharge at 5 Pa, as the time-averaged sheath voltage increases. It is clearly evident that the relative H_3^+ ion flux decreases with increasing voltage and a simultaneous increase in the relative H_2^+ ion flux occurs with increasing voltage.

As the time-averaged sheath voltage increases, in figure 4.10, the mean H_3^+ energy increases from $\sim\ 50\,eV$ to $\sim\ 140\,eV$. In this energy range, two main processes are responsible for the conversion of H_3^+ to H_2^+, CID and ACT. The cross-section of CID remains relatively constant ($\sim 4 \cdot 10^{-20} m^2$) in the relevant energy range. However, the cross-section for ACT from H_3^+ to H_2^+ increases from $\sim\ 0.4 \cdot 0^{-20}\ m^2$ to $\sim\ 1 \cdot 10^{-20}\, m^2$ resulting in an increase in H_2^+ relative ion flux and a decrease in H_3^+ flux.

Figure 4.16 shows the absolute fluxes as a function of the time-averaged sheath voltage for the same conditions as in figure 4.15. As expected, increasing the sheath voltage increases the plasma density and the mean ion energy and thus the absolute flux impinging on the electrode increases.

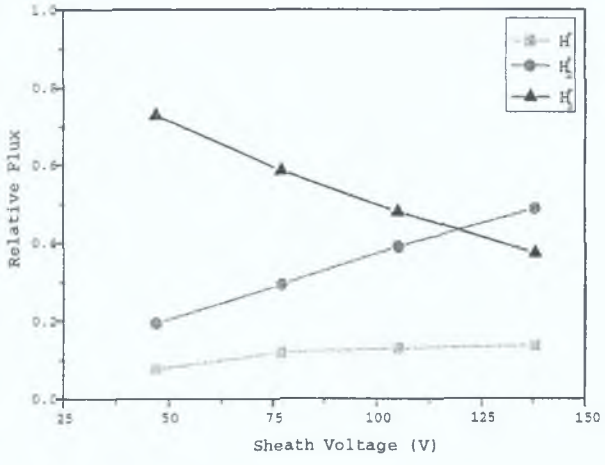

Figure 4.15: *Relative fluxes of H^+, H_2^+ and H_3^+ in a 13.56 MHz hydrogen discharge at 5 Pa, as a function of sheath voltage in experiment*

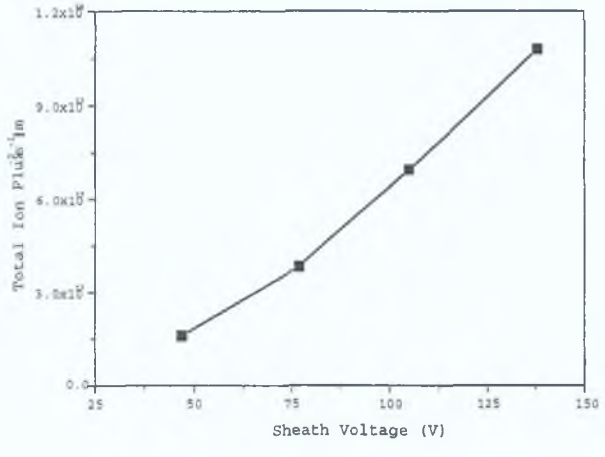

Figure 4.16: *Total ion flux as a function of time-averaged sheath voltage for a hydrogen discharge at 13.56 MHz and 5 Pa in experiment*

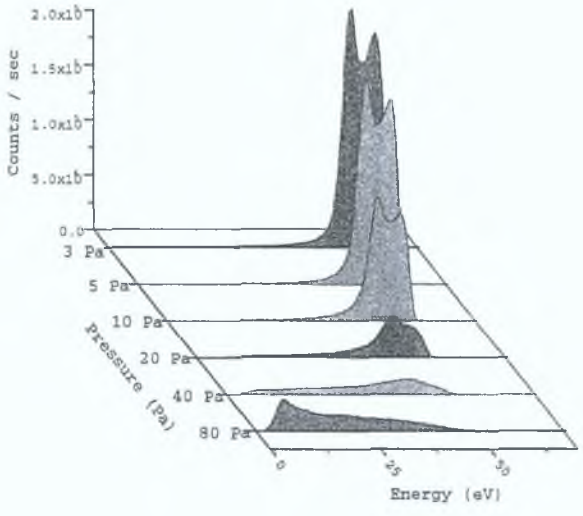

Figure 4.17: *H_3^+ IEDF in 27.12 MHz hydrogen discharge at $V_{sheath} = 54\,V$, for various pressures in experiment*

4.4 Hydrogen discharge at 27.12 MHz

Pressure variation

The influence of pressure on IEDFs of the three ion species in hydrogen at 27.12 MHz is very similar to the influence at 13.56 MHz. The figures for the distributions of H_2^+ and H^+ are shown in Appendix A. Figure 4.17 shows the H_3^+ IEDF in a hydrogen 27.12 MHz discharge, at a time-averaged sheath potential of 54 V, for various pressures. Comparing the distributions to those in the 13.56 MHz discharge, it can be observed that the mean ion impact energy is greater at all pressures in the 27.12 MHz discharge. This is a consequence of a smaller sheath width at 27.12 MHz. The displacement current, and hence density, is greater with higher frequency. This higher density leads to a smaller sheath. Thus ions lose less energy while travelling through the sheath.

Figure 4.18 shows a plot of relative fluxes, at a time-averaged sheath voltage of 36 V, as a function of pressure for each of the three ion species. Similar influences of the cross-sections, for conversion of H_3^+ to H_2^+ and H^+, are noticeable as in the 13.56 MHz discharge. When the energy of the H_3^+ ion energy decreases, with

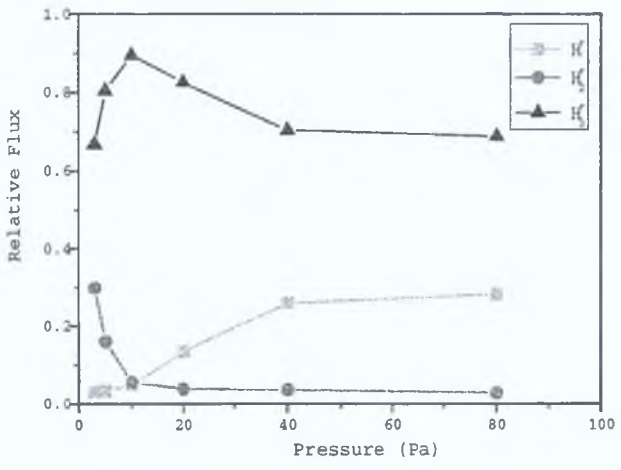

Figure 4.18: *Relative Fluxes of H^+, H_2^+ and H_3^+ at 27.12 MHz and $V_{sheath} = 36\,V$ as a function of pressure in experiment*

increasing pressure, they go below the threshold for CID to H_2^+, thus destroying the source for H_2^+ production. This results in an increase in H_3^+ ion flux and a corresponding decrease in H_2^+ flux. As the H_3^+ energy decreases with increasing pressure, the H_3^+ ions can no longer be converted to H_2^+ but they are still above the threshold energy for CID to H^+. Therefore, in combination with the increased neutral density, H_3^+ ions can be efficiently converted to H^+. This is reflected in figure 4.18 through the increased H^+ flux from 3 Pa to 40 Pa. In figure 4.7 for the 13.56 MHz discharge the relative H^+ flux decreases above 40 Pa whereas it remains constant for the 27.12 MHz discharge. This is due to the smaller sheath width in the 27.12 MHz discharge. There are still H_3^+ ions at 80 Pa above the threshold for CID to H^+ in 27.12 MHz whereas at 13.56 MHz H_3^+ ions have moved to below the threshold.

Using the calibration factor determined in section 4.2, the absolute fluxes are estimated. Figure 4.19 shows the absolute flux as a function of pressure for the same conditions as in figure 4.18 for both experiment and 2D PIC simulation. The trend in the experiment and simulation is similar with a decrease in flux from 5 Pa to 40 Pa. However, as before a slightly lower flux can be observed in

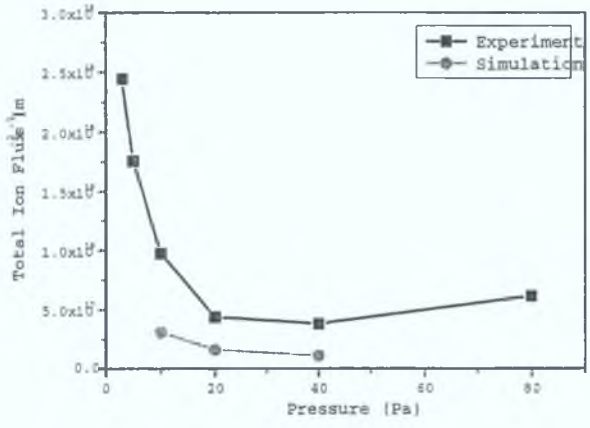

Figure 4.19: *Total ion flux at 27.12 MHz and $V_{sheath} = 36\,V$ as a function of pressure for experiment and simulation*

the simulation. The higher flux at low pressures can be partially due to a higher mean energy at low pressures.

Figure 4.19 shows the total density at the electrode surface as a function of pressure for the same conditions as figure 4.18. As in figure 4.9 at 13.56 MHz the total density increases from 20 Pa to 80 Pa. This is due to more efficient ohmic heating at high pressures. However, the density also increases for decreasing pressure which is not obvious at 13.56 MHz, in figure 4.9. This can be attributed to more efficient stochastic heating [95, 96, 97, 98, 99, 100] at 27.12 MHz than 13.56 MHz. At high pressure, the plasma can be sustained by power being deposited to electrons through collisions. However, at low pressure, when the electron mean free path is large enough so that electrons are essentially collisionless, a collisionless heating mechanism exists. At low pressures electrons travel freely through the bulk discharge until they reach the sheath regions where they are reflected back due to the sheath electric fields. Here the particles either lose or gain energy depending on whether they move in the opposite or same direction as the sheath front. When the sheath moves towards the electron, then the energy increases; when the sheath moves away, then the energy decreases. On average, over one period, a net energy gain can be expected. Since the sheath

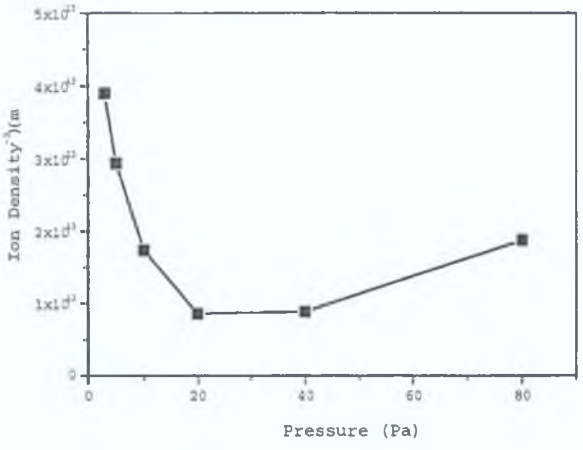

Figure 4.20: *Ion density in front of electrode at 27.12 MHz and* $V_{sheath} = 36\,V$ *as a function of pressure in experiment*

edge oscillates faster at 27.12 MHz than at 13.56 MHz power deposition can be expected to be greater at 27.12 MHz, thus, leading to increased plasma density. Stochastic heating is only prominent at pressures below $\sim 10\,Pa$. Therefore this mechanism does not explain the increase in density from 20 Pa to 10 Pa. Another mechanism prominent in CCRF discharges is ionisation by γ or secondary electrons [34, 92, 91]. This results from increased secondary emission from the electrodes at high ion impact energies. The secondary electrons are accelerated across the sheath to the bulk plasma and perform ionisation. The energy of secondary electrons from the electrode is sufficiently greater than the mean energy of the plasma electrons. This mechanism is usually more efficient in the intermediate pressure regime when conditions are favorable for a cascade of ionising collisions. However, as can be observed from figure 4.17, the mean ion impact energy is greater at lower pressures. Therefore, it is most likely that ionisation by γ electrons is most efficient in the 10 Pa to 20 Pa pressure range, where the mean ion impact energy is high and there is also probability of collision. This mechanism could not be observed at 13.56 MHz, since the mean ion impact energy is lower, again a consequence of the wider sheath in 13.56 MHz discharges.

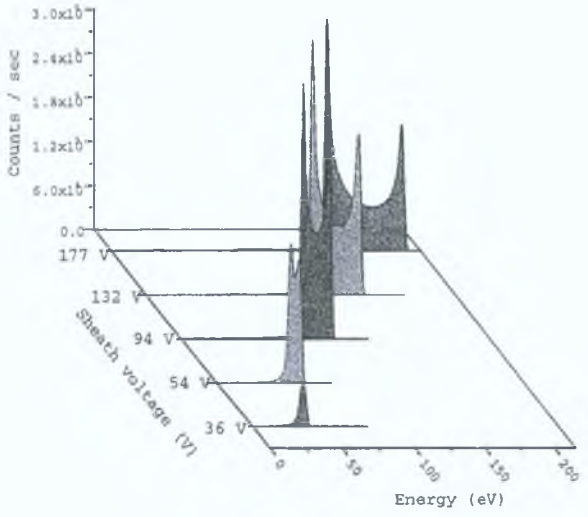

Figure 4.21: *H_3^+ IEDF in a 27.12 MHz hydrogen discharge at 5 Pa for various sheath voltages in experiment*

Sheath Voltage variation

Figure 4.21 shows the H_3^+ IEDF, at 27.12 MHz and 5 Pa, for varying sheath voltages. As observed at 13.56 MHz the peak separation increases with increasing sheath potential and at a sheath potential of 36 V the peak splitting cannot be resolved. The low energy contribution due to exothermic conversion reaction of H_2^+ ions which was noticeable, at higher sheath voltages, at 13.56 MHz is not obvious at 27.12 MHz. The displacement current is larger at 27.12 MHz than at 13.56 MHz, therefore the density will be greater at 27.12 MHz. The greater the density, the smaller the sheath width. Thus, at 27.12 MHz ions cross the sheath in a shorter time thus, undergoing less collisions.

Figure 4.22 shows H_3^+ IEDFs from the 2D PIC simulations for the same conditions as in figure 4.21 . The agreement is very good. However, there are still differences between the IEDFs in the experiment and the simulation. The separation of the peaks in the bi-modal structure is greater in the experiment than in the simulations. As shown in equation 4.3 this separation depends on sheath voltage, frequency, mass and sheath width. All quantities, except the sheath width are defined the same in both the experiment and simulation. Therefore, the differ-

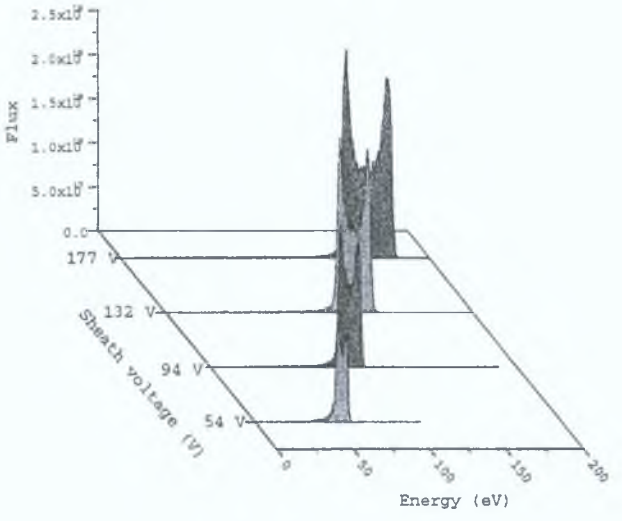

Figure 4.22: *H_3^+ IEDF from simulation in a 27.12 MHz hydrogen discharge at 5 Pa for various sheath voltages*

ence must be due to a larger sheath width in the simulation. The sheath width is dependent on electron temperature and density. It was already observed in 4.19 that the fluxes in the simulation are lower than in the experiment thus leading to a larger sheath width. The plasma density is an important parameter in defining the sheath properties. Therefore, it does not suffice to have an accurate sheath model, the entire plasma needs to be accurately simulated. However, this is a rather difficult task. Production and loss processes in the plasma bulk govern the electron temperature and plasma density. Due to limited cross-sections available it can be difficult to obtain an accurate model of the plasma bulk chemistry. Ion neutralisation at the electrode and production of fast neutrals and secondary electrons can be very important in capacitively coupled rf discharges [93]. Fast neutrals lead to increased vibrational excitation [43] and thus easier ionisation in the bulk plasma. and secondary electrons lead to direct ionisation [94]. However, in the simulation fast neutrals are not taken into account. In capacitively coupled rf discharges most of the power coupled into the discharge is dissipated in the sheaths. A large fraction of this power is reflected back into the plasma through fast neutrals. However, in the simulation most of this power is absorbed by the

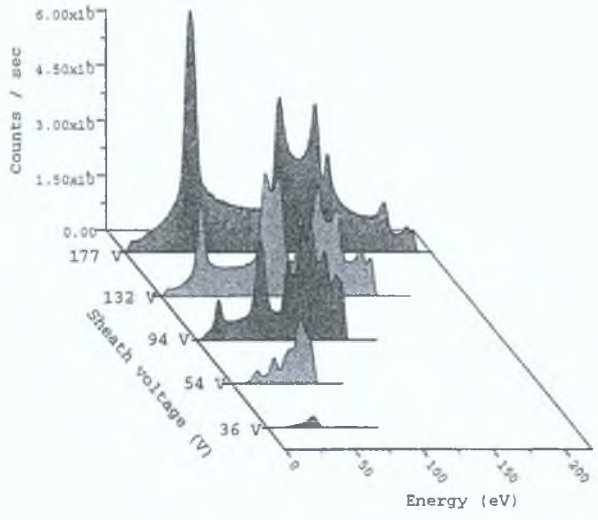

Figure 4.23: *H_2^+ IEDF in a 27.12 MHz hydrogen discharge at 5 Pa for various sheath voltages in experiment*

electrodes.

Figure 4.23 and 4.24, show the experimental and simulation IEDFs of H_2^+, for the same conditions as in figure 4.21. The agreement between experiment and simulation is again very good. However, there are discrepancies. There are more secondary peaks in the simulation IEDFs, a sign that the ions in the simulation take more rf cycles to cross the sheath.

Figure 4.25 shows the H^+ IEDF at the same conditions as figure 4.21. A large fraction of ions can be observed to enter the sheath from the bulk plasma. This is apparent from the bi-modal structure centered about the time-averaged sheath potential. In the H^+ IEDF, at 13.56 MHz (figure 4.12), this could not be observed, the main portion of the IEDF is at energies lower than the sheath potential. This difference can again be attributed to the smaller sheath width at 27.12 MHz. At 13.56 MHz, more H_3^+ ions are converted to H^+ ions appearing at lower energies in the H^+ IEDF. Also, at 13.56 MHz most of the H^+ ions which enter the sheath from the plasma bulk undergo collisions before they reach the electrode and also appear at lower energies. The remaining contribution from the bulk plasma that reaches the electrode is very small and is not distinguishable in

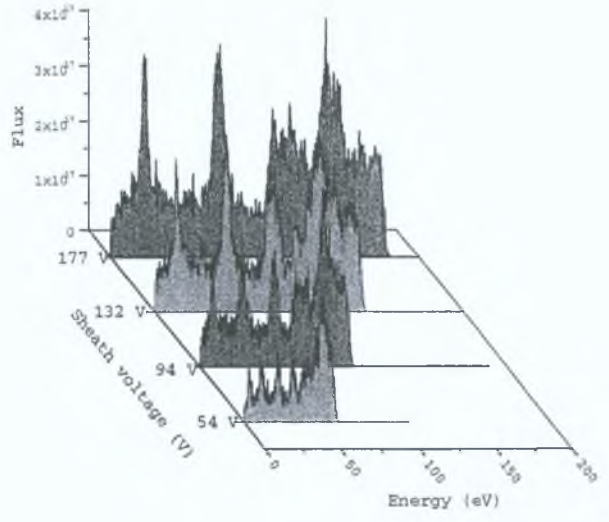

Figure 4.24: *H_2^+ IEDF from simulation in a 27.12 MHz hydrogen discharge at 5 Pa for various sheath voltages*

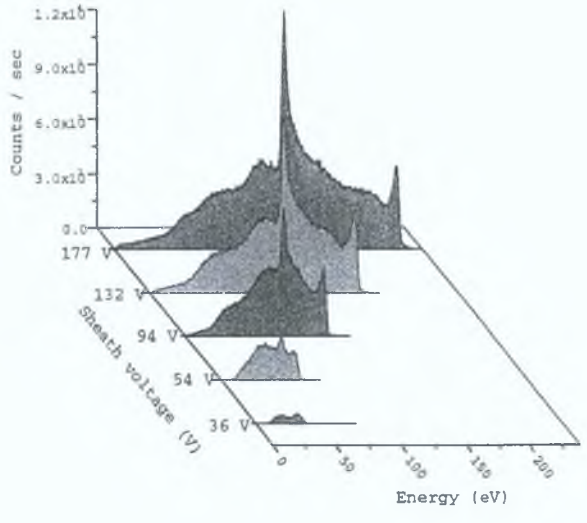

Figure 4.25: *H^+ IEDF in a 27.12 MHz hydrogen discharge, at 5 Pa for various sheath voltages in experiment*

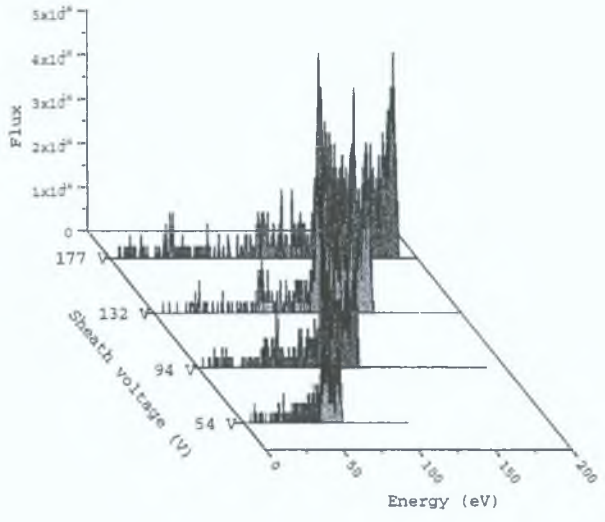

Figure 4.26: *H^+ IEDF from simulation in a 27.12 MHz hydrogen discharge, at 5 Pa for various sheath voltages*

the IEDF. At 27.12 MHz, H^+ ions entering from the plasma bulk can cross the smaller sheath without collision. In combination with a lower contribution, due to less H_3^+ ions converting to H^+, the higher energy plasma bulk contribution is now distinguishable.

The H^+ IEDF from the simulation for the same conditions as figure 4.25 is shown in figure 4.26. As was the case for the H_3^+ IEDF, the separation of the peaks in the bi-modal structure of the H^+ IEDF in the experiment is larger than in the simulation.

Comparing figure 4.21 to 4.25, the peak separation of the H^+ bi-modal IEDF is greater than the peak separation of the H_3^+ IEDF. The heavier ion, H_3^+, takes longer to traverse the sheath. Therefore H_3^+ ions experience more averaging and the peaks in the saddle structure are closer together compared to H^+. The lighter, H^+ ion, can follow the rf sheath modulation better and therefore the IEDF will better reflect the time dependent sheath voltage.

A plot of the relative ion fluxes as a function of sheath potential, at 5 Pa, is shown in figure 4.27. The H_3^+ ion flux decreases as the H_2^+ ion flux increases. As in the 13.56 MHz discharge, the cross-section for conversion of H_3^+ to H_2^+ in

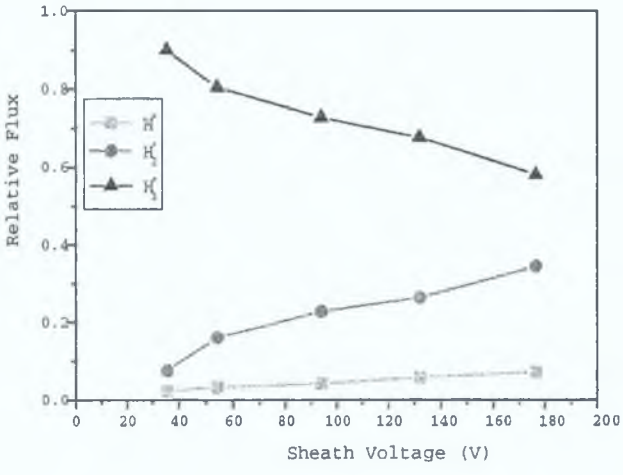

Figure 4.27: *Relative Fluxes of H^+, H_2^+ and H_3^+ at 27.12 MHz and 5 Pa as a function of sheath voltage in experiment*

this energy range increases thus resulting in an increase in H_2^+ relative flux and a simultaneous decrease in H_3^+ relative flux. However, the relative increase in H_2^+ flux at 13.56 MHz is greater than at 27.12 MHz. This is again due to the smaller sheath width, and therefore less H_3^+ is converted to H_2^+, at 27.12 MHz.

The absolute flux plotted as a function of sheath voltage, for 27.12 MHz hydrogen discharge at 5 Pa, is shown in figure 4.28. As expected, an increase in voltage results in an increase in the plasma density and the mean ion energy. This is reflected in an increase in absolute flux impinging on the electrode. The trends with sheath voltage in the experiment and simulation agree very well. The absolute flux in the experiment is generally higher than in the simulation. This is in agreement with the argument made earlier of a lower density in the simulations leading to larger sheath width. The fluxes in the simulation are lower due to additional ionisation processes, discussed above, in the experiment which are neglected in the simulation.

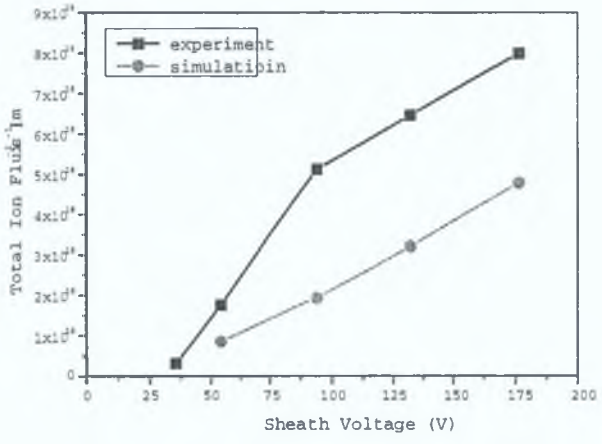

Figure 4.28: *Total ion flux at 27.12 MHz and 5 Pa as a function of sheath voltage, in experiment and simulation*

4.5 Deuterium discharges

IEDFs in pure deuterium discharges were measured for each of the three ion species D^+, D_2^+ and D_3^+. The structures of the IEDFs are similar to IEDFs in hydrogen discharges shown in the previous sections. The plots are shown in appendix A. A calibration factor for determination of absolute fluxes in deuterium, was determined as described earlier in section 4.2, to be $7.17 \cdot 10^{11}\, m^{-2} counts^{-1}$. This value is very close to the calibration factor of hydrogen. The calibration factor was applied to the measured fluxes and the absolute fluxes estimated. Figure 4.29 shows the absolute flux plotted as a function of time-averaged sheath voltage in both a 13.56 MHz and 27.12 MHz discharge. The flux in the 27.12 MHz discharge is greater than in the 13.56 MHz discharge as was also observed in hydrogen discharges. This is due to larger displacement current and thus plasma density at 27.12 MHz. The absolute flux in deuterium is less than that in hydrogen. Deuterium is twice as heavy as Hydrogen. Therefore the spacing between vibrational levels in deuterium is smaller. In deuterium there are more vibrational levels between the ground state and first ionisation level. This allows more losses into vibrational excitation and thus a lower plasma density in deuterium.

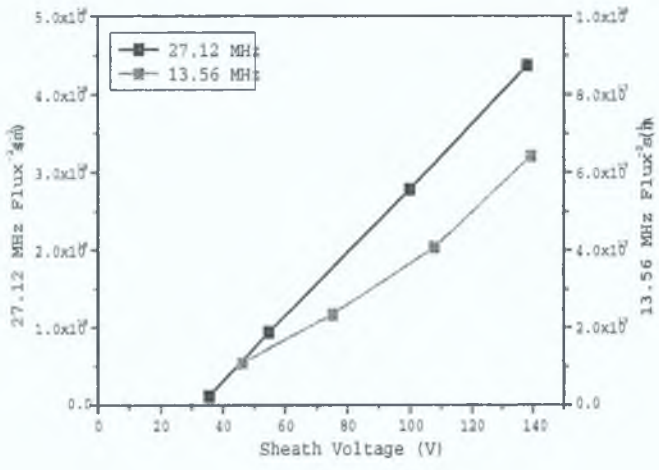

Figure 4.29: *Total ion flux in deuterium discharge as a function of time-averaged sheath voltage at 5 Pa in both 13.56 MHz and 27.12 MHz discharges*

Figure 4.30 shows the density, as a function of pressure, for the deuterium discharge at 13.56 MHz and 27.12 MHz. The total density at the electrode surface was found by dividing the flux distribution functions by $\sqrt{\frac{2E}{M}}$. The total densities are plotted as a function of pressure for 13.56 MHz and 27.12 MHz. As in the hydrogen discharge at 13.56 MHz, the density increases with increasing pressure indicating more efficient ohmic heating at high pressure. At 27.12 MHz this increase in density with increasing pressure is also evident. However, there is an additional increase in density for low pressures ($< 20\,Pa$). This indicates the stochastic heating mechanism. This was also observed in the 27.12 MHz hydrogen discharge.

4.6 Hydrogen and deuterium mixtures

Mixtures of hydrogen and deuterium offer the opportunity to investigate the IEDF of different ion species traversing the same rf sheath. This can give more detailed insight into the sheath chemistry. Nine positive ion species can co-exist at six different masses, these are given in table 4.1. The most interesting results for mixtures of 50 % hydrogen 50 % deuterium are shown and discussed below,

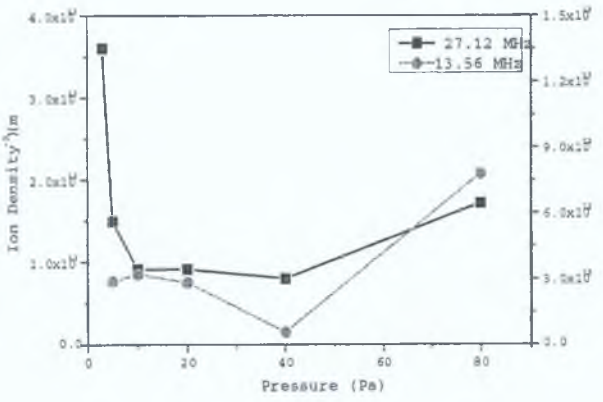

Figure 4.30: *Ion density in front of electrode in deuterium discharge, at 13.56 MHz and 27.12 MHz*

Mass (amu)	Ions
1	H^+
2	H_2^+, D^+
3	H_3^+, HD^+
4	H_2D^+, D_2^+
5	D_2H^+
6	D_3^+

Table 4.1: *Ions in hydrogen - deuterium discharge mixtures*

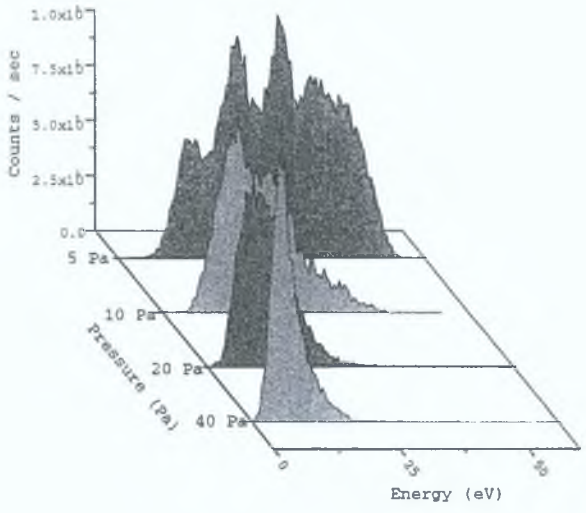

Figure 4.31: *IEDF of mass 2 at 13.56 MHz in 50 % hydrogen 50 % deuterium mixture;* $V_{sheath} = 50\,V$*, for varying pressures*

the rest are in appendix A.

Variation of pressure in the 13.56 MHz discharge

Figure 4.31 shows the IEDF of mass two in a 50 % hydrogen and 50 % deuterium mixture at 13.56 MHz at a time-averaged sheath voltage of 50 V for various pressures. This distribution function has a contribution of two different ion species, D^+ and H_2^+. The D^+ contribution is not very obvious at low pressures. However, the distinct peaks of H_2^+ having undergone symmetric charge exchange, with background H_2 molecules, in the sheath can be observed. As the pressure increases the IEDF resembles an exponential function. It can be assumed that at low pressures H_2^+ dominates and at high pressures D^+ is the dominant ion. As was observed in the pure discharges, as pressure increases H_3^+ IEDF moves to lower energies below the thresholds for conversion to H_2^+. However, at these high pressures the D_3^+ IEDF is above the threshold for conversion to D^+. Thus D^+ dominates the IEDF at high pressures.

Figure 4.32 shows the IEDF of mass one, H^+. This distribution is the same as could be expected for the D^+ contribution in the previous distribution. The

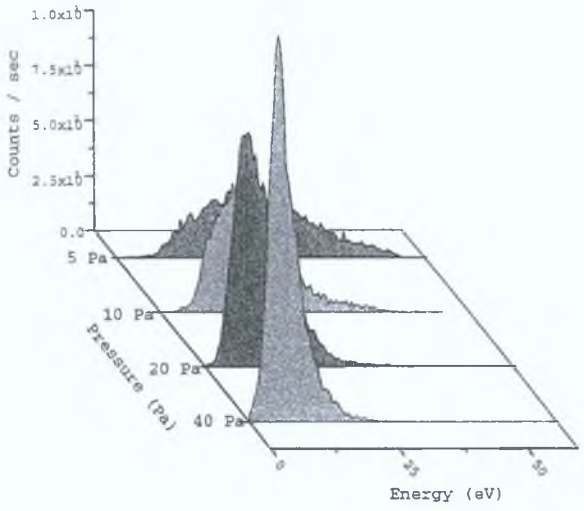

Figure 4.32: *IEDF of mass 1 at 13.56 MHz in 50 % hydrogen 50 % deuterium mixture;* $V_{sheath} = 50\,V$*, for varying pressures*

flux is greater at higher pressures, in agreement with figure 4.31.

Figure 4.33 shows the relative fluxes of each of the ion species in the mixture of hydrogen and deuterium, at a time-averaged sheath voltage of 50 V, as a function of pressure. The trends are obvious and similar to the pure discharges. The most interesting point is that as pressure increases H^+ flux increases in agreement with the argument made above that H^+ and D^+ flux increase with increasing pressure.

Variation of sheath voltage in the 13.56 MHz discharge

Figure 4.34 shows the IEDF of mass 6 in a 13.56 MHz discharge, at 5 Pa, for variation of the sheath voltage. From table 4.1 the only ion species of mass 6 is D_3^+. D_3^+ ions enter into the sheath from the bulk plasma and experience the entire potential drop of the sheath voltage, appearing at the time-averaged sheath potential. The peak separation becomes more noticeable for increasing sheath voltage. There is a small contribution at lower energies, from D_2^+ ions colliding with D_2 background gas molecules in the sheath producing thermal D_3^+ ions which are in turn accelerated towards the electrode. The distribution is similar to the H_3^+ IEDFs in a pure hydrogen discharge at 13.56 MHz (figure

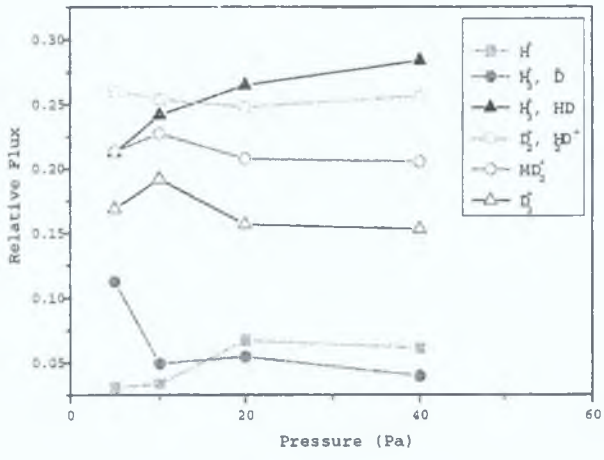

Figure 4.33: *Relative fluxes of ion species in 50 % hydrogen 50 % deuterium 13.56 MHz discharge at* $V_{sheath} = 50\,V$*, as a function of pressure*

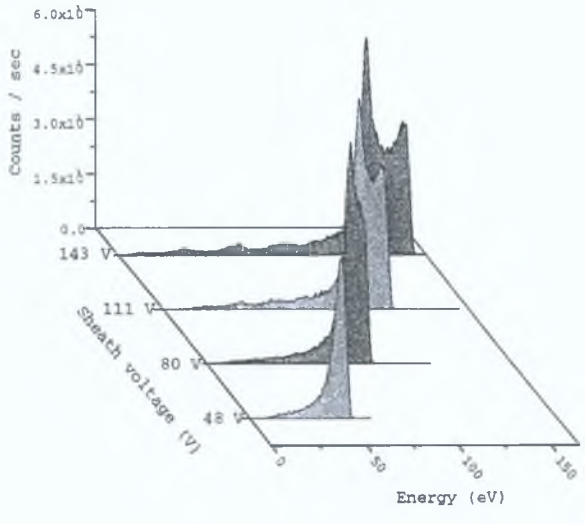

Figure 4.34: *IEDF of mass 6 at 13.56 MHz in 50 % hydrogen 50 % deuterium mixture at 5 Pa for varying sheath voltages*

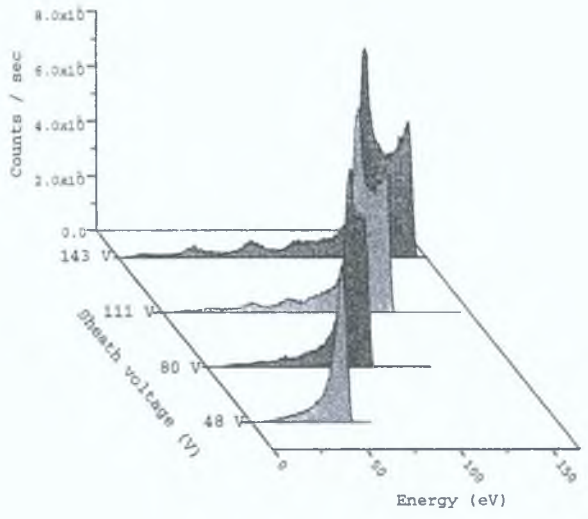

Figure 4.35: *IEDF of mass 5 at 13.56 MHz in 50 % hydrogen 50 % deuterium mixture at 5 Pa for varying sheath voltages*

4.10).

The IEDF of mass 5, HD_2^+ for the same conditions as in figure 4.34, is shown in figure 4.35. The structure is very similar to the D_3^+ IEDF, indicating most ions enter from the bulk plasma experiencing the entire potential drop of the sheath. The low energy contribution is due to collisions of thermal HD^+ ions with HD background gas molecules in the sheath. A similar collision process produces low energy contribution in H_3^+ and D_3^+ IEDFs.

The IEDF of mass 4, figure 4.36, incorporates a contribution of two ion species, H_2D^+ and D_2^+ . The H_2D^+ distribution can be expected to be very similar to the distribution of HD_2^+ in figure 4.35. Therefore, higher energy, saddle structure centered around the time-averaged sheath potential, is due to H_2D^+ ions entering the sheath from the bulk plasma and crossing the sheath without collision. Superimposed on the H_2D^+ IEDF is a D_2^+ distribution. The lower energy secondary peaks are due to D_2^+ ions created in the sheath. These are typical symmetric charge exchange peaks observed for D_2^+ ions and H_2^+ ions in pure discharges (figure 4.11).

Figure 4.37 shows the IEDF of mass 3, again it includes a contribution of

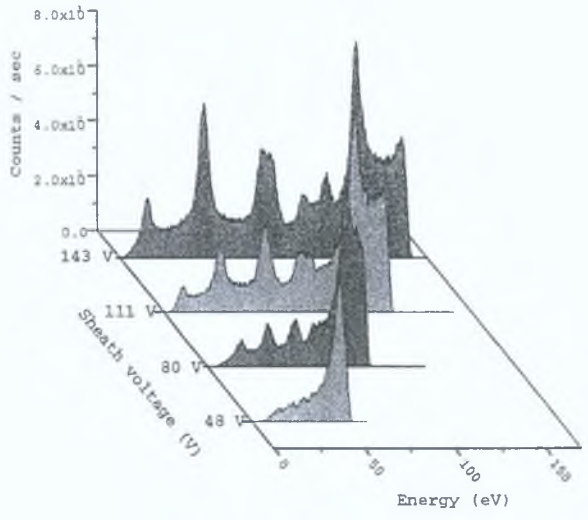

Figure 4.36: *IEDF of mass 4 at 13.56 MHz in 50 % hydrogen 50 % deuterium mixture at 5 Pa for varying sheath voltages*

two different ion species, DH^+ and H_3^+. The H_3^+ ions enter the sheath from the plasma bulk and contribute to the higher energy saddle structure, their IEDF would be similar to that of D_3^+ in figure 4.34. Also a small contribution of the low energy peaks are due to H_3^+ as can also be seen in the D_3^+ IEDF. The rest of the low energy contribution is due to DH^+. Comparing figure 4.37 and 4.34 there is a higher low energy contribution in figure 4.37, this difference corresponds to the HD_2^+ contribution.

Variation of sheath voltage in the 27.12 MHz discharge

Figures 4.38 and 4.39 show the IEDFs, of mass 6 and mass 4 respectively, in a 27.12 MHz discharge at 5 Pa for various sheath voltages. Mass 6 is due to D_3^+ ions, most of the ions enter into the sheath from the plasma and experience the full potential drop appearing as a bi-model structure centered around the time-average sheath potential. Due to the small sheath width at 27.12 MHz the ions can pass the sheath without collision and thus the low energy contribution is negligible. Mass 4 contains the contributions of two ion species, H_2D^+ and D_2^+. The high energy contribution, due to ions entering the sheath from the plasma

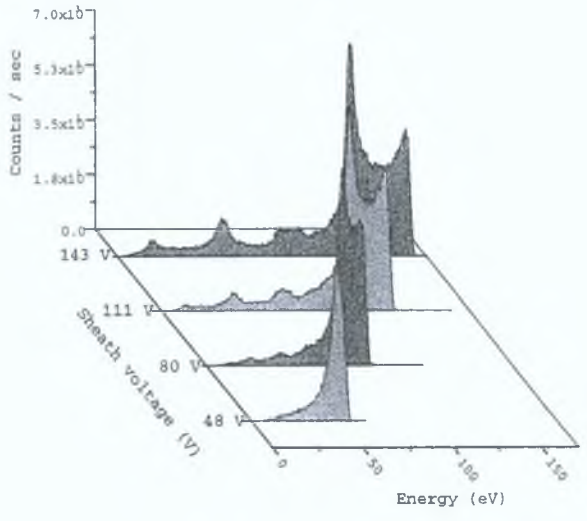

Figure 4.37: *IEDF of mass 3 at 13.56 MHz in 50 % hydrogen 50 % deuterium mixture at 5 Pa for varying sheath voltages*

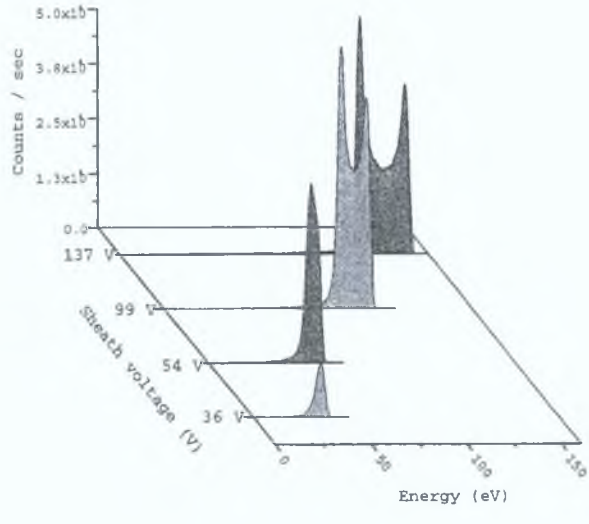

Figure 4.38: *IEDF of mass 6 at 27.12 MHz in 50 % hydrogen 50 % deuterium mixture at 5 Pa for varying sheath voltages*

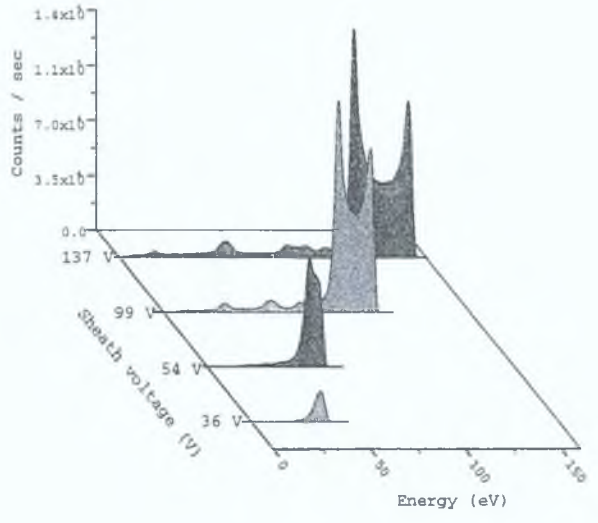

Figure 4.39: *IEDF of mass 4 at 27.12 MHz in 50 % hydrogen 50 % deuterium mixture at 5 Pa for varying sheath voltages*

bulk, is the H_2D^+ contribution and the low energy secondary peaks, due to D_2^+ undergoing charge exchange. The charge exchange peaks are not as pronounced as for the 13.56 MHz discharge. Again, this is due to the smaller sheath width at 27.12 MHz discussed above. The ions can traverse the sheath in a shorter time thus undergoing less collisions.

4.7 Conclusions

Sheath dynamics in a single frequency high voltage plasma boundary sheath were investigated. This involved the comparison of IEDF measurements, using a mass resolved ion energy analyser, with results of a 2D PIC simulation. A calibration method for estimation of absolute fluxes impinging on the electrode surface was developed. The agreement between experiment and simulation is in general very good and the results are understood. All discrepancies are related to differences in the sheath width in the experiment and simulation. Due to the dependence of sheath width on density, this highlights the importance of accurately modelling the entire plasma in the simulation. The plasma density needs to be well defined in the simulation for a good comparison to the experiment. It does not suffice

to have an accurate model of the sheath region in order to investigate the ion dynamics within the sheath. An accurate model of the bulk plasma chemistry is also required. Unfortunately, this is a rather difficult task. With limited accurate cross-section data available it is difficult to accurately model the bulk chemistry. Fast neutrals can be very important for vibrational excitation in the plasma promoting easier ionisation. Fast neutrals created at the electrode surface through ion impact neutralisation are not taken into account in the simulation.

CHAPTER 5

Dual frequency rf sheath results

CCRF discharges operated with two frequencies simultaneously are used in technological applications for independent control of the ion flux and the ion impact energy onto the substrate. To date, very few fundamental investigations on these devices have been performed. Here mass resolved IEDFs are measured in a dual frequency confined capacitively coupled rf discharge system. The calibration method, discussed in the previous chapter, for the estimation of absolute fluxes impinging on the electrode is employed. The plasma is operated at frequencies of 1.94 MHz and 27.12 MHz. As in the investigations of the single frequency sheath IEDFs of hydrogen ions are considered. They are suitable for the investigations at these frequencies, since they are light enough to respond to time variations of both frequencies. The IEDFs reflect the time dependence of both frequencies. Results are compared to a dual frequency particle-in-cell (DF PIC) simulation[1]. A simple analytical model is used to describe the sheath potential of a dual frequency discharge. The model predicts the complex structures of the measured and simulated IEDFs. Heavier Xe^+ ions are investigated as an admixture in the hydrogen discharge. The mass is 44 times heavier than H_3^+ ions and closer to

[1]Dual frequency PIC simulation was developed by M. M. Turner

that of ions in typical processing discharges.

5.1 Dual frequency rf sheath model

For better understanding of the results in this chapter a simple analytical model for a dual frequency rf sheath is developed in this section. The model is based on the corresponding single frequency model of Godyak [34] described in section 1.2.5. A symmetric discharge with sheaths, a and b, is considered with the assumptions of constant ion density throughout the discharge and no electrons in the sheath region.

The dual frequency rf current $I_{rf}(t)$ is given by

$$I_{rf}(t) = I_1 \cos(\omega_1 t) + I_2 \cos(\omega_2 t + \varphi) \tag{5.1}$$

Similar to the single frequency case (section 1.2.5), current continuity and integrating Poisson's equation give the following relation for the width, $s_a(t)$, of sheath a

$$\frac{ds_a(t)}{dt} = -\frac{I_{rf}(t)}{enA} \tag{5.2}$$

Integration results in

$$s_a(t) = s - s_1 \sin(\omega_1 t) - s_2 \sin(\omega_2 t + \varphi) \tag{5.3}$$

with

$$s = s_1 + s_2 \qquad and \qquad s_{1/2} = \frac{I_{1/2}}{enA\omega_{1/2}} \tag{5.4}$$

The voltage drop across sheath a is given by

$$V_a(t) = -\frac{en}{2\varepsilon_0}(s_a(t))^2 = -\frac{en}{2\varepsilon_0}(s - s_1 \sin(\omega_1 t) - s_2 \sin(\omega_2 t + \varphi))^2 \tag{5.5}$$

Similarly the voltage across sheath b is

$$V_b(t) = -\frac{en}{2\varepsilon_0}\left(s + s_1 \sin(\omega_1 t) + s_2 \sin(\omega_2 t + \varphi)\right)^2 \tag{5.6}$$

Neglecting the voltage drop across the plasma bulk we obtain the total voltage drop across the discharge V_{rf} by combining the sheath voltages V_a and V_b

$$V_{rf}(t) = V_a(t) - V_b(t) = \frac{2ens}{\varepsilon_0}\left(s_1 \sin(\omega_1 t) + s_2 \sin(\omega_2 t + \varphi)\right) \tag{5.7}$$

Similar to the single frequency case, there is second harmonic generation for the individual sheath voltages while the total voltage drop across the discharge is free of harmonic generation.

Taking an applied rf voltage V_{rf}

$$V_{rf}(t) = V_1 \sin(\omega_1 t) + V_2 \sin(\omega_2 t + \varphi) \tag{5.8}$$

the sheath voltages a and b are given by:

$$V_a(t) = -\frac{V_1 + V_2}{4}\left(1 - \frac{V_1}{V_1 + V_2}\sin(\omega_1 t) - \frac{V_2}{V_1 + V_2}\sin(\omega_2 t + \varphi)\right)^2 \tag{5.9}$$

and

$$V_b(t) = -\frac{V_1 + V_2}{4}\left(1 + \frac{V_1}{V_1 + V_2}\sin(\omega_1 t) + \frac{V_2}{V_1 + V_2}\sin(\omega_2 t + \varphi)\right)^2 \tag{5.10}$$

Figure 5.1 shows the sheath voltage waveforms determined from equations 5.9 and 5.10. The plots illustrate the non linearity of the individual sheath voltages. Figure 5.2 shows the applied voltages waveform, illustrating the linear nature of the combined sheath voltages.

The relationship between the applied voltage V_{rf} and the time averaged sheath width s is

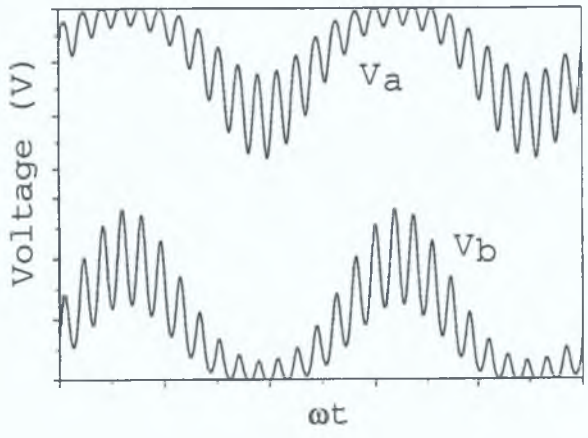

Figure 5.1: *RF dual frequency sheath voltage waveforms, V_a and V_b.*

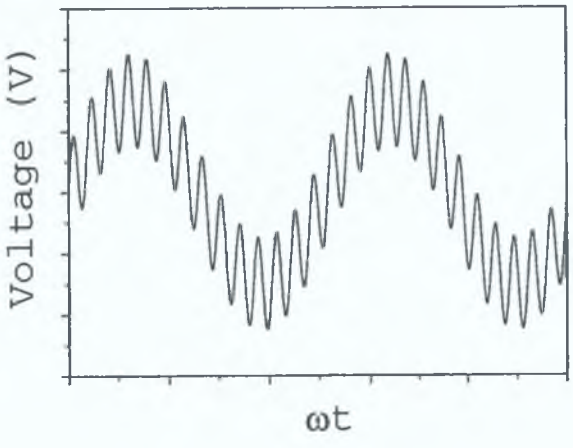

Figure 5.2: *Applied rf dual frequency voltage waveform, V_{rf}.*

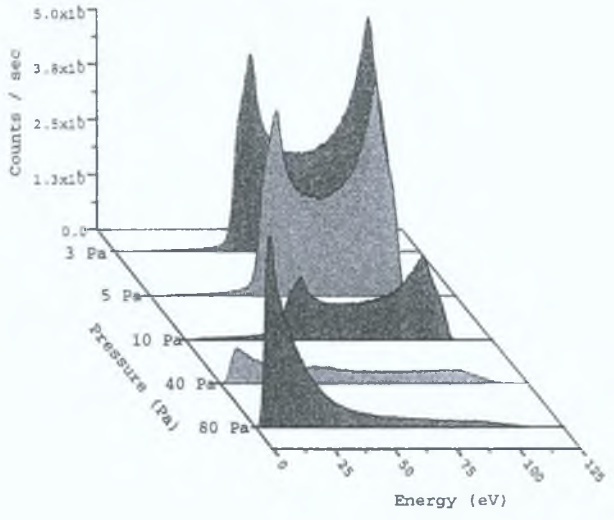

Figure 5.3: H_3^+ *IEDF for 1.94 MHz and 27.12 MHz time-averaged sheath voltages of 37.5 V each, at various pressures in experiment*

$$s = \sqrt{\frac{\varepsilon_0}{2en}(V_1 + V_2)} \tag{5.11}$$

This simple model does not consider the full complexity of dual frequency rf sheath dynamics, but it clearly shows the basic phenomena. More detailed models are available [23]. However, they become extremely complex loosing focus of the basic phenomena.

5.2 Hydrogen dual frequency discharge

Variation of pressure

The 1.94 MHz and 27.12 MHz voltages are both held constant at a time-averaged sheath voltage of 37.5 V each, and the discharge pressure varied. Figure 5.3 shows the H_3^+ IEDFs. The sheath potential waveform is shown in figure 5.1. H_3^+ ions crossing the sheath can almost perfectly follow the 1.94 MHz voltage but, as seen in the previous chapter, they can only slightly respond to the 27.12 MHz voltage. At low 27.12 MHz voltages the ions response to temporal variations in the sheath

potential cannot be resolved. Therefore, the overall voltage ions experience will be a time-varying 1.94 MHz voltage with an additional offset corresponding to the time-averaged 27.12 MHz sheath voltage. This is reflected in the distribution function in figure 5.3. At 3 Pa the sheath is essentially collisionless and the contribution from the plasma bulk can be observed. The distribution is centered around the total time-averaged sheath voltage, $\sim 72\,eV$, the sum of both the 1.94 MHz and 27.12 MHz time-averaged voltages. The broad saddle shaped structure is similar to that of a single frequency discharge. This is the 1.94 MHz component of the sheath voltage where ions can almost perfectly respond to the voltage oscillation. Since the ions respond to a time-averaged 27.12 MHz sheath potential the distribution is at an offset corresponding to this voltage. Subtracting the 27.12 MHz time-averaged sheath voltage from the IEDF leaves the distribution almost at zero. This indicates that the ions can almost perfectly respond to the 1.94 MHz sheath oscillation from zero to maximum. As the pressure increases the effect of collisions becomes more pronounced, the high energy contribution in the IEDF, reduces and the low energy contribution in the IEDF becomes more prominent. At 80 Pa the IEDF approaches an exponential function as described in section 1.2.4 and also observed for the single frequency discharge.

Figure 5.4 shows the H_3^+ IEDFs from the simulation for the same conditions as in figure 5.3. The agreement with the experimental results is quite good. However, there are discrepancies. The higher energy peak of the bi-modal structure in the experiment is more dominant than in the simulation at low pressures. This can be due to more elastic scattering of H_3^+ with the background gas in the simulation, since there is also more low energy contribution in the simulation than in the experiment. The ions in the simulation seem to undergo more collisions while travelling through the sheath. This hints to a larger sheath in the simulation.

Figure 5.5 shows H_2^+ IEDFs for the same conditions as figure 5.3. The two peaks at 55.5 eV and 104 eV correspond to the maximum and minimum sheath potential discussed above. The high energy peak is not as pronounced as in H_3^+ IEDF (figure 5.3). The high energy peak is due to ions entering the sheath when

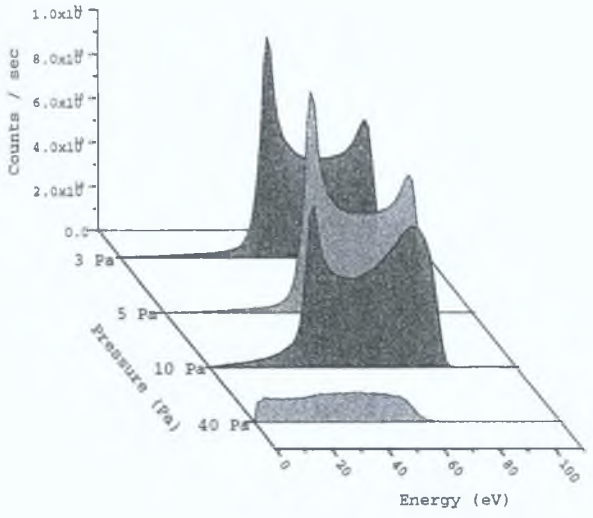

Figure 5.4: *H_3^+ IEDF for 1.94 MHz and 27.12 MHz time-averaged sheath voltages of 37.5 V each, at various pressures in simulation*

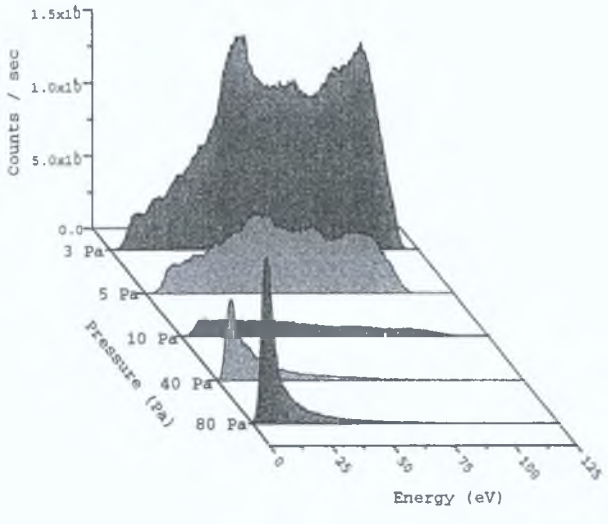

Figure 5.5: *H_2^+ IEDF for 1.94 MHz and 27.12 MHz time-averaged sheath voltages of 37.5 V each, at various pressures in experiment*

the sheath is at its maximum extent. These ions have a longer path from the plasma to the electrode thus undergoing more collisions than ions entering at minimum sheath width. As the pressure increases the ratio of the two peaks in the saddle-shaped structure changes, the high energy peak becomes less dominant indicative of ions undergoing collisions. Structures in between the two main peaks are due to ions entering the sheath at maximum sheath potential and undergoing collisions before reaching the electrode. The peaks of charge exchange collisions are not as pronounced in the IEDFs from the dual frequency plasma compared to the IEDFs from the single frequency plasma in the last chapter. Discrete collision peaks in the IEDF are formed by ions which are created in the field-free region when the sheath is oscillating and accelerated from rest when the electric field rises. In the dual frequency case the time dependent sheath potential that ions experience is dominated by the 1.94 MHz voltage. However, as explained above, at 1.94 MHz H_2^+ ions can almost perfectly follow the oscillating sheath voltage. When they enter into the sheath they are accelerated across the entire sheath potential before the electron front passes them out.

Figure 5.6 shows the H_2^+ IEDFs from the simulation for the same conditions as in figure 5.5. The high energy peak of the bi-modal structure in the simulation is not as dominant in the experiment. This is the same as was observed for the H_3^+ IEDFs (figure 5.4). The low energy contribution is also more dominant in the simulation than in the experiment. Therefore, ions in the simulation seem to undergo more collisions while traversing the sheath than in the experiment. There are more secondary peaks due to symmetric charge exchange in the IEDF from the simulation. The ions do not enter into the sheath and reach the electrode before it retracts. The number of secondary peaks approximately equals the number of rf cycles it takes ions to cross the sheath [38], therefore, ions take longer to cross the sheath in the simulation than in the experiment. Both these discrepancies hint towards a wider sheath in the simulation due to a lower plasma density already observed in the single frequency discharges in chapter 4.

Figure 5.7 and 5.8 show H^+ IEDFs for experiment and simulation, respec-

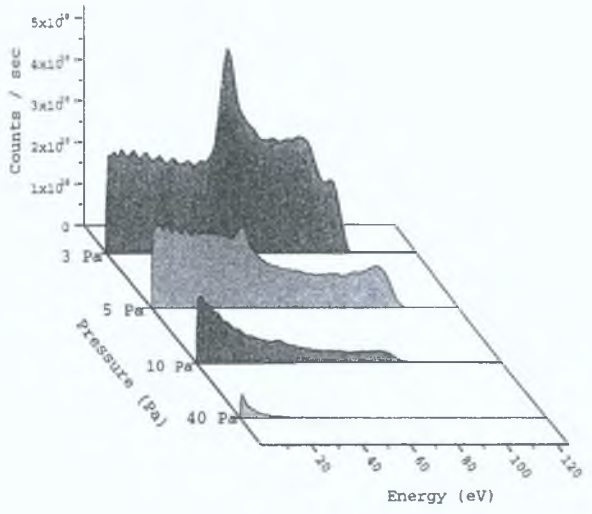

Figure 5.6: *H_2^+ IEDF for 1.94 MHz and 27.12 MHz time-averaged sheath voltages of 37.5 V each, at various pressures in simulation*

tively, under the same condition as in figure 5.3. The H^+ IEDF is very collision dominated and it is quite difficult to distinguish distinct structures. However, as for H_2^+ ions, at low pressures, the high energy saddle shaped structure has a depleted high energy peak due to ions undergoing collisions in the sheath. As was the case for IEDFs of H_3^+ and H_2^+, as the pressure increases, ions move to lower energies taking on an exponential distribution function.

The absolute flux of ions impacting on the electrode, as a function of pressure for fixed 27.12 MHz and 1.94 MHz time-averaged sheath potentials of 37.5 V each, is shown in figure 5.9 for both experiment and simulation. The plot resembles that for a single frequency discharge excited at 27.12 MHz. At high pressures, collisions are more frequent and ohmic heating becomes more efficient, also giving rise to increased plasma density and thus flux onto the electrode [1]. The increase in flux for lower pressures can be due to more efficient stochastic heating [95, 96, 97, 98, 99], also observed for the single frequency discharge at 27.12 MHz (figure 4.20).

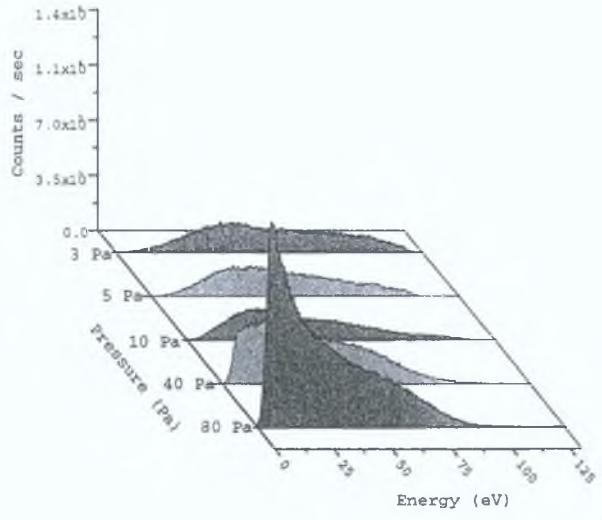

Figure 5.7: *H^+ IEDF for 1.94 MHz and 27.12 MHz time-averaged sheath voltages of 37.5 V each, at various pressures in experiment*

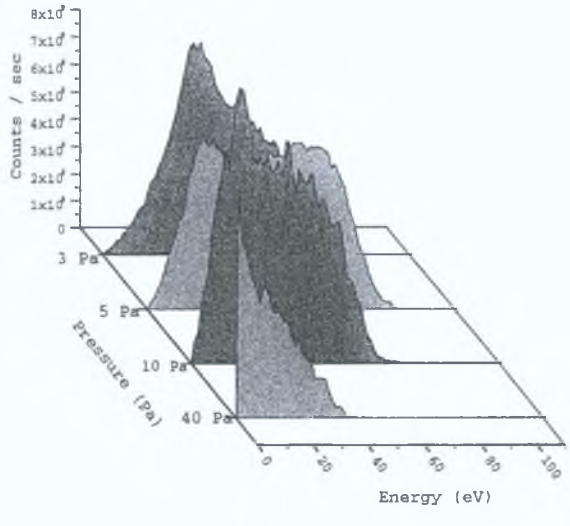

Figure 5.8: *H^+ IEDF for 1.94 MHz and 27.12 MHz time-averaged sheath voltages of 37.5 V each, at various pressures in simulation*

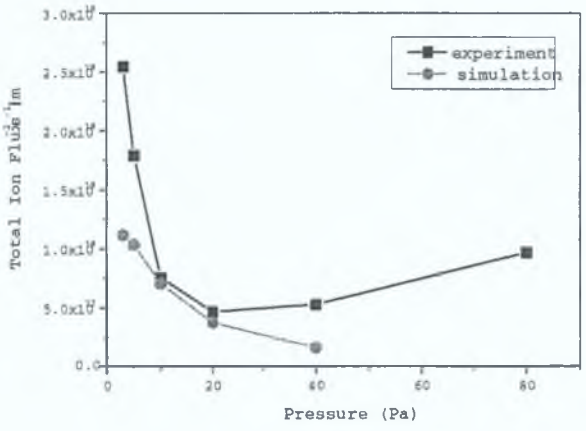

Figure 5.9: *Total ion flux in Hydrogen discharge as a function of pressure for 1.94 MHz and 27.12 MHz time-averaged sheath voltages of 37.5 V each in both experiment and simulation*

Variation of 27.12 MHz voltage

Figure 5.10 shows H_3^+ IEDFs at 5 Pa with 1.94 MHz time-averaged sheath voltage held constant at 37.5 V, the 27.12 MHz sheath voltage is varied. The IEDF resembles the saddle shaped structure of a single frequency sheath (figure 4.21). However, the two peaks in the saddle shaped structure are quite broad compared to the peaks of an IEDF in a single frequency discharge. H_3^+ ions can slightly respond to the 27.12 MHz oscillations, as observed in the last chapter for a single frequency 27.12 MHz discharge. As the 27.12 MHz voltage increases ions respond to time varying oscillations of both 1.94 MHz and 27.12 MHz. The two main peaks in the saddle structure of the IEDF begin to split, forming a four peak structure. Splitting of the two peaks cannot be resolved at low 27.12 MHz voltages. The first peak, lowest energy peak, in the IEDF is due to ions entering the sheath at the minimum sheath potential. The next peak corresponds to a maximum of the 27.12 MHz voltage around the 1.94 MHz voltage minimum. The two high energy peaks are due to ions entering the sheath at extrema of the 27.12 MHz voltage around the 1.94 MHz voltage maximum. As the 27.12 MHz voltage increases, the distribution moves to higher energies but the separation of the centre of the

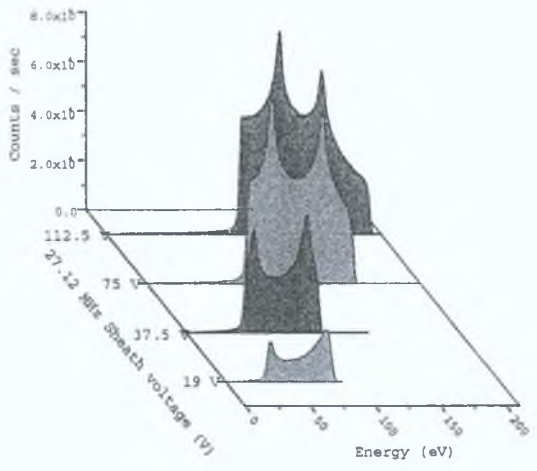

Figure 5.10: *H_3^+ IEDF at 5 Pa and a 1.94 MHz component of the time-averaged sheath potential of 37.5 V, at various 27.12 MHz sheath voltages in experiment*

low and high energy peaks remains constant. This separation is determined by the 1.94 MHz voltage. The two inner peaks, of the four peak structure, are more pronounced since more ions can enter the sheath at these potentials. There is only one phase in which ions can enter into the sheath to gain an energy equivalent to the maximum and minimum sheath potentials. However, to gain an energy equivalent to the maximum of the 27.12 MHz voltage around the minimum of the 1.94 MHz voltage there are several phases in which an ion can enter into the sheath. Similarly, the same applies for the minimum of the 27.12 MHz voltage around the maximum of the 1.94 MHz voltage. Thus the inner peaks are more pronounced since more ions can enter into the sheath at these potentials. The separation of the two high energy peaks is greater than the two low energy peaks.

Examining the non-linear waveform in figure 5.1 it can be observed that the non linearity of the sheath voltage results in more pronounced oscillation around one of the extrema of the 1.94 MHz voltage. From equation 1.44, it was shown that the peak separation is greater for larger voltages. Thus, the separation of the high energy peaks is greater due to the greater oscillation amplitude of the 27.12 MHz around the 1.94 MHz maximum. Figure 5.11 shows the IEDF predicted from

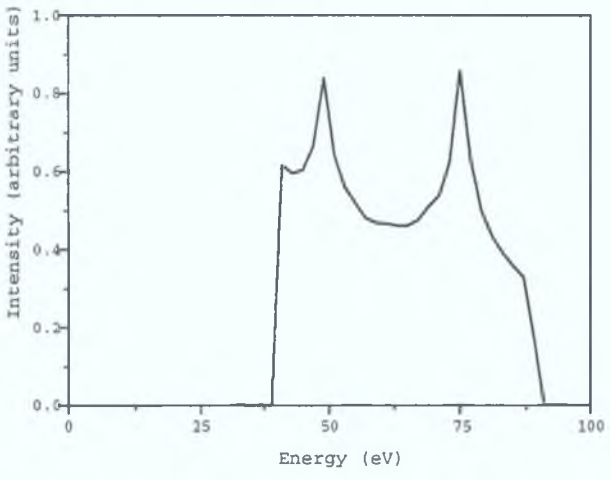

Figure 5.11: *Typical H_3^+ IEDF as determined from the model using equation 5.10*

the phase - energy relationship of the sheath potential. The agreement to the experimental and simulation results is remarkable.

Figure 5.12 shows the H_3^+ IEDF from the simulation for the same conditions as figure 5.10. The agreement is very good. The splitting of the main peaks in the bi-modal structure, due to the time varying 27.12 MHz voltage, is observed.

The frequencies used, 1.94 MHz and 27.12 MHz, are not an exact multiple of each other. Therefore, there is no fixed phase relationship between them. The maxima and minima of the 27.12 MHz are averaged out over all phases of the 1.94 MHz. If the frequencies are an exact multiple, and have a fixed phase relationship, the ions experience several extrema while crossing the sheath. Peaks occur in the IEDF when the derivative of the potential is zero. This would be reflected in the IEDF as a series of peaks or structures between the main peaks.

Figure 5.13 shows H_2^+ IEDFs for varying 27.12 MHz sheath potentials. As the 27.12 MHz voltage increases, the time dependent sheath voltage becomes more dominated by 27.12 MHz rather than 1.94 MHz. Therefore, charge exchange peaks become more prominent. Ions entering into the sheath no longer cross the sheath before the electron front passes them out.

Figure 5.14 shows the H_2^+ IEDFs from the simulation under the same condi-

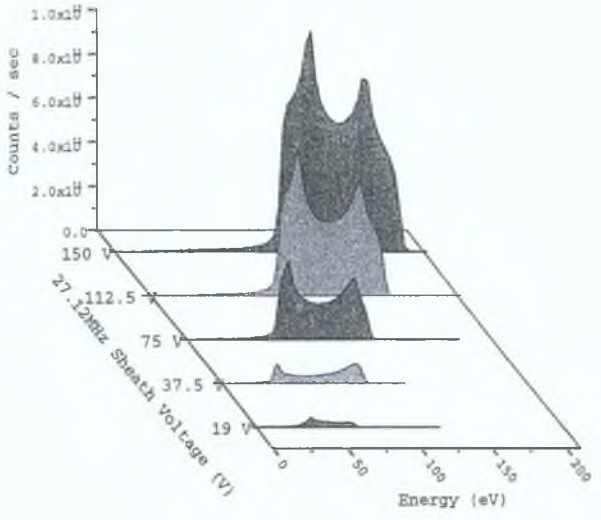

Figure 5.12: *H_3^+ IEDF at 5 Pa and a 1.94 MHz component of the time-averaged sheath potential of 37.5 V, at various 27.12 MHz sheath voltages in simulation*

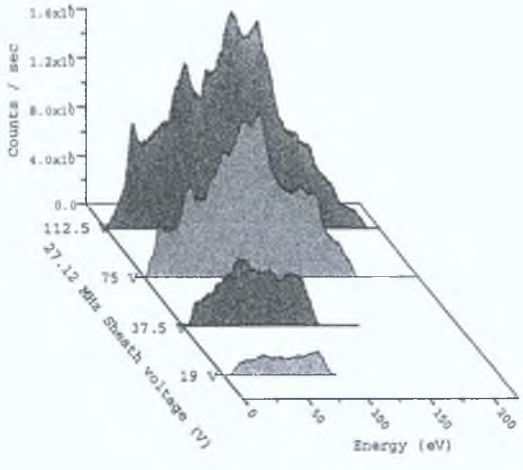

Figure 5.13: *H_2^+ IEDF at 5 Pa and a 1.94 MHz component of the time-averaged sheath potential of 37.5 V, at various 27.12 MHz sheath voltages in experiment*

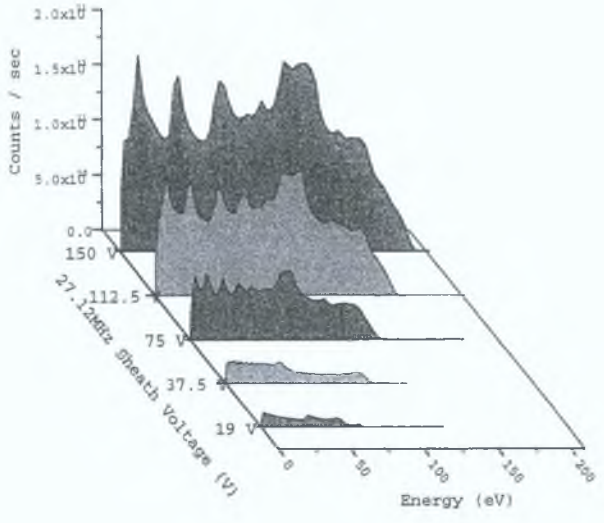

Figure 5.14: *H_2^+ IEDF at 5 Pa and a 1.94 MHz component of the time-averaged sheath potential of 37.5 V, at various 27.12 MHz sheath voltages in simulation*

tions as figure 5.13. The agreement of the high energy part of the distribution with the experiment is very good. However, in the low energy region the secondary peaks in the simulation are more dominant. Comparing the number of secondary peaks reveals that ions in the simulation take more rf cycles to cross the sheath. This again, hints to larger sheaths in the simulation.

Figure 5.15 shows the absolute flux impacting on the electrode for the same sonditions as figure 5.13. As expected increasing the voltage, increases both the plasma density and the mean ion energy, thus causing an increase in the flux. The agreement between experiment and simulation is remarkable, however there are slight discrepancies in the absolute numbers. The flux in the experiment is higher than in simulation. This is in agreement with the earlier observations of a wider sheath in the simulation, caused by a lower density.

Variation of 1.94 MHz voltage

Figure 5.16 shows H_3^+ IEDFs at 5 Pa and a fixed 27.12 MHz time-averaged sheath voltage of 37.5 V. As the 1.94 MHz voltage increases the saddle shaped structure broadens and the centre of the distribution shifts to higher energies. Subtracting

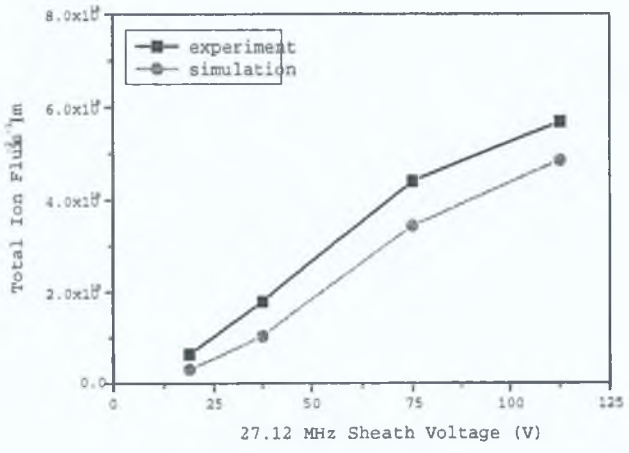

Figure 5.15: *Total ion flux in Hydrogen, at 5 Pa and 1.94 MHz component of the time-averaged sheath potential of 37.5 V, as a function of 27.12 MHz sheath voltage in both experiment and simulation*

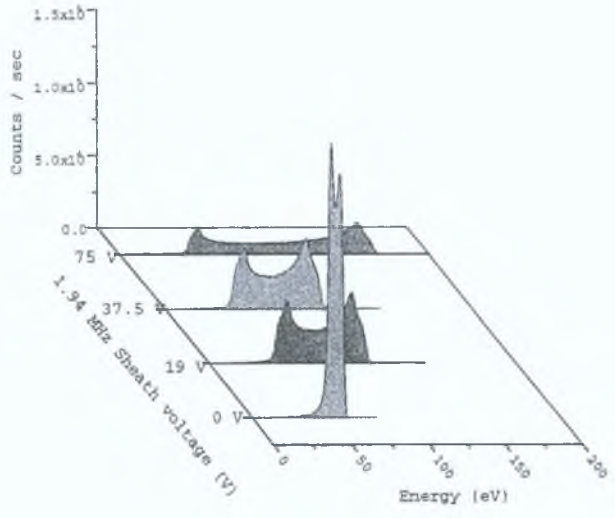

Figure 5.16: *H_3^+ IEDF at 5 Pa and 27.12 MHz component of time averaged sheath potential of 37.5 V, for various 1.94 MHz voltages in experiment*

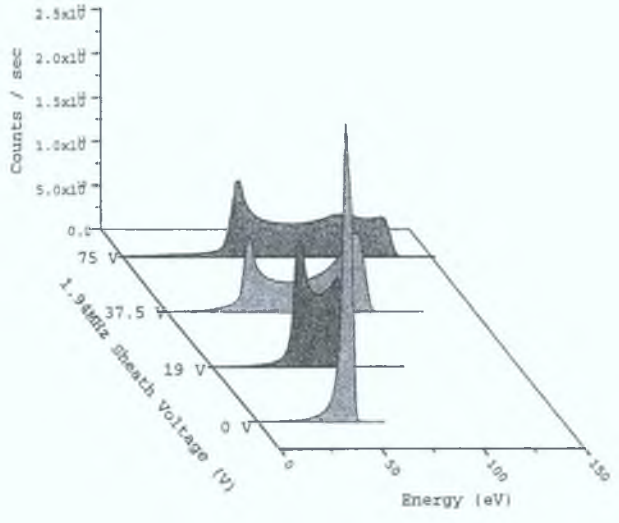

Figure 5.17: *H_3^+ IEDF at 5 Pa and 27.12 MHz component of time averaged sheath potential of 37.5 V, for various 1.94 MHz voltages in simulation*

the time-averaged 27.12 MHz component of the sheath voltage, positions the IEDF almost at zero. This illustrates that ions can almost perfectly respond to the oscillation of the 1.94 MHz voltage between zero and maximum sheath voltage. Figure 5.17 shows the H_3^+ IEDFs from the simulation for the same conditions as in figure 5.16. The structures of the distributions agree well, however, there is quite a difference in the range of the distribution. The distributions in the experiment are much broader. This is in agreement with the previous results showing lower density in the simulations and thus larger sheath width. The larger the sheath width, the smaller the separation since ions take longer to cross the sheath and thus experience more averaging of the sheath potential. The four peak structure of the H_3^+ IEDFs discussed in the previous section is not obvious since the 27.12 MHz sheath voltage is too low for the splitting of the bi-modal peaks to be resolved.

Figure 5.18 and 5.19 show H_2^+ IEDFs, in the experiment and simulation, for the same conditions as figure 5.16. At lower sheath voltages, the secondary peaks in both the experiment and simulation are prominent. However, the number of peaks in the simulation is greater, due to the larger sheath width in the simulation.

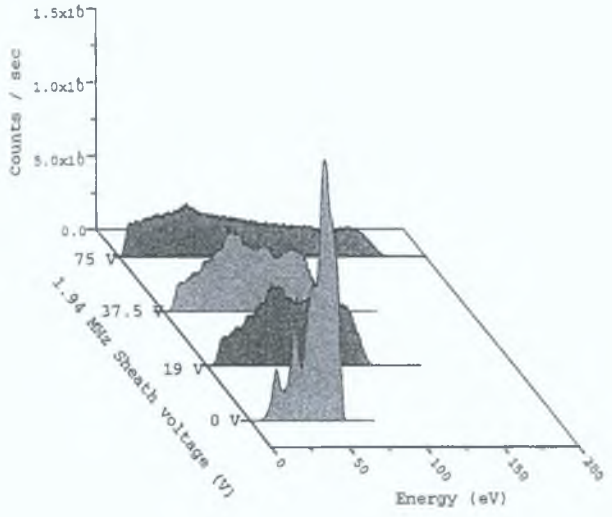

Figure 5.18: *H_2^+ IEDF at 5 Pa and 27.12 MHz component of time averaged sheath potential of 37.5 V, for various 1.94 MHz voltages in experiment*

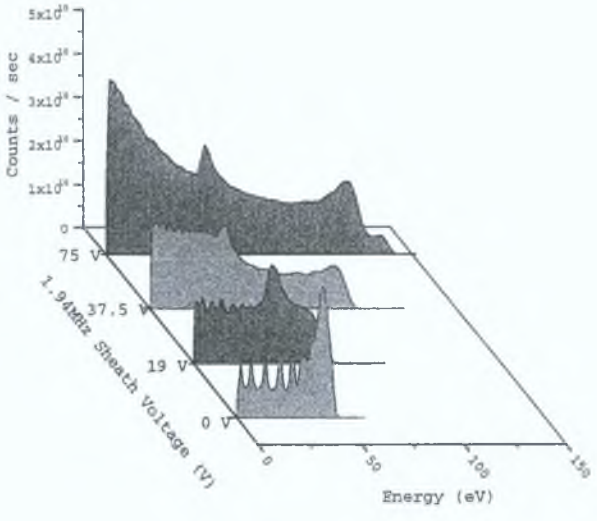

Figure 5.19: *H_2^+ IEDF at 5 Pa and 27.12 MHz component of time averaged sheath potential of 37.5 V, for various 1.94 MHz voltages in simulation*

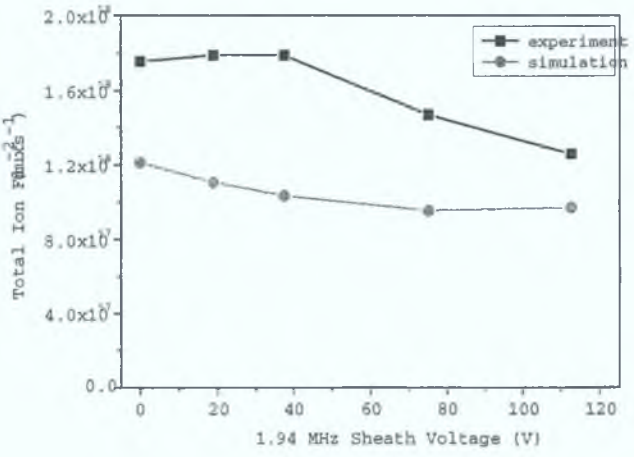

Figure 5.20: *Total ion flux in Hydrogen, at 5 Pa and a 27.12 MHz time averaged sheath potential of 37.5 V, as a function of 1.94 MHz sheath voltage in both experiment and simulation*

As the sheath voltage increases the distribution from the simulation due to ions which have undergone collisions tends towards an exponential function. The larger sheath in the simulations results in more ions undergoing collisions in the sheath.

Figure 5.20 shows the absolute flux impacting on the electrode as a function of 1.94 MHz sheath potential. As the 1.94 MHz voltage increases the sheaths become larger and the plasma volume decreases. As the plasma volume gets smaller there is less ionisation and therefore reduced plasma density. The reduction in flux is obvious in both the experiment and simulation results. The influence of the sheath width to the reduction of the plasma bulk volume starts to become significant at lower voltages in the simulation because the sheath widths are in general larger.

This reduction in plasma density and thus flux is more pronounced in the simulation and begins at lower 1.94 MHz sheath voltages. This is due to the already lower ionisation and density in the simulation. Therefore, even for low 1.94 MHz sheath voltages the sheath are larger and thus the ionisation decreases.

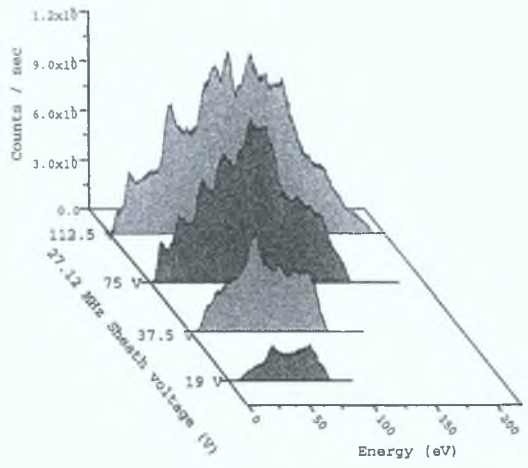

Figure 5.21: *D_2^+ IEDF at 5 Pa and 1.94 MHz component of time-averaged sheath potential of 37.5 V, for various 27.12 MHz sheath voltages*

5.3 Deuterium dual frequency discharge

Figure 5.21 shows the D_2^+ IEDFs, in a dual frequency discharge at 5 Pa, the 1.94 MHz sheath voltage is kept constant at $37.5\,V$ and the 27.12 MHz sheath voltage varied. Compared to H_2^+ IEDF in a pure hydrogen discharge, there are more secondary peaks. It was observed in section 4.5 that the flux in deuterium is lower than in hydrogen discharge. This lower flux in deuterium discharges gives rise to a wider sheath. This in combination with the heavier mass of D_2^+ compared to H_2^+ means that ions take more rf cycles to cross the sheath, resulting in more secondary peaks in the IEDF.

Figure 5.22 shows the D_3^+ IEDFs, at 5 Pa and 27.12 MHz sheath potential of 37.5 V, for various 1.94 MHz voltages. The separation of the two main peaks in the saddle-shaped structure is not as large in deuterium as for H_3^+ in figure 5.16. This is due to both the wider sheath in deuterium discharges, and the heavier mass of D_3^+ compared to H_3^+. The D_3^+ ions cannot respond to the 1.94 MHz sheath oscillations as good as the hydrogen ions therefore they experience more averaging at the extrema. Thus the two peaks are closer together and at higher and lower values than H_3^+ in figure 5.16.

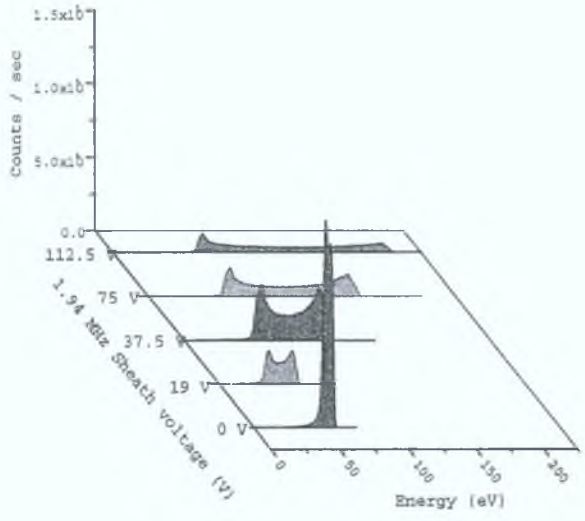

Figure 5.22: *D_3^+ IEDF at 5 Pa and 27.12 MHz component of time-averaged sheath potential of 37.5 V, for various 1.94 MHz sheath voltages*

5.4 Hydrogen and xenon mixtures

Up to now, we have used light ions to investigate the dynamics of the dual frequency sheath. However, dual frequency plasmas are used for independent control of the ion flux and ion energy, in technical applications, with heavier ions. Therefore, the effect on heavier ions is now investigated, in a dual frequency sheath, using Xe^+ ions in a hydrogen plasma with a small admixture of xenon.

The mass of Xe^+ is 44 times heavier than H_3^+. Figure 5.23 and 5.24 show the IEDFs of H_3^+ and Xe^+ ions, respectively, at 5 Pa and 1.94 MHz sheath voltage held at a constant time-averaged value of 37.5 V, for various 27.12 MHz sheath voltages. The structures of H_3^+ IEDFs are similar to those in the pure hydrogen dual frequency discharge. The Xe^+ IEDFs are quite different to the H_3^+ IEDFs, they do not posses the complicated structures characteristic of H_3^+ IEDFs. The distribution is a saddle shaped structure centered around the time-averaged sheath potential. There is no splitting of the peaks in the saddle shaped structure. Xe^+ ions are too heavy to respond to the 27.12 MHz time variations and only slightly respond to the 1.94 MHz oscillations, therefore, the structures of their IEDFs are quite similar to those of a single frequency discharge.

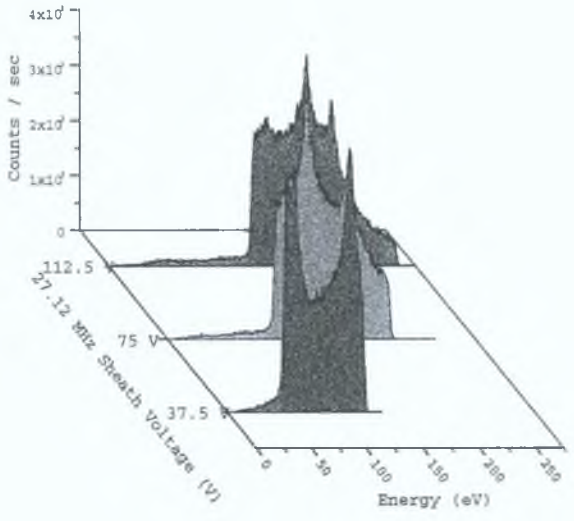

Figure 5.23: *H_3^+ IEDF in Hydrogen admixture Xenon discharge for $V_{1.94MHz} = 37.5\,V$ and 5 Pa at various 27.12 MHz sheath voltages*

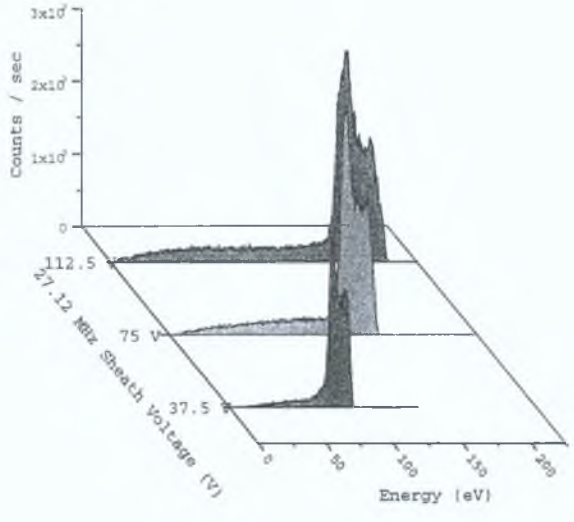

Figure 5.24: *Xe^+ IEDF in Hydrogen admixture Xenon discharge for $V_{1.94MHz} = 37.5\,V$ and 5 Pa at various 27.12 MHz sheath voltages*

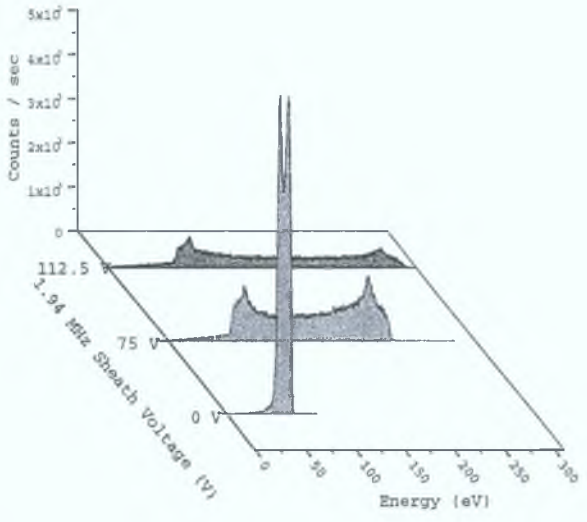

Figure 5.25: H_3^+ *IEDF in Hydrogen admixture Xenon discharge for* $V_{27.12MHz} = 37.5\,V$ *and 5 Pa at various 1.94 MHz sheath voltages*

In figure 5.25 and 5.26 the IEDFs of H_3^+ and Xe^+ , respectively, are shown at 5 Pa with the 27.12 MHz sheath voltage held constant and the 1.94 MHz sheath voltage varied. With increasing 1.94 MHz sheath voltage the peak separation increases and the distribution moves to higher energies. It is obvious that controlling the ion energy is greatly improved with heavier masses.

5.5 Conclusions

The ion dynamics in a dual frequency plasma sheath was investigated. A mass resolved ion energy analyser was used to measure IEDFs at high voltage dual frequency sheaths. The calibration method described in the previous chapter was employed for the determination of absolute fluxes impinging on the electrode surface. As in the previous chapter light hydrogen ions are employed for investigations. A simple analytical model for a dual frequency sheath was developed and it predicts the structures of the measured IEDFs. Results are also compared to a dual frequency particle-in-cell (PIC) simulation. The agreement is good. All discrepancies are due to a larger sheaths in the simulation as a result of a lower plasma density. Reiterating, a simulation needs to accurately model the entire

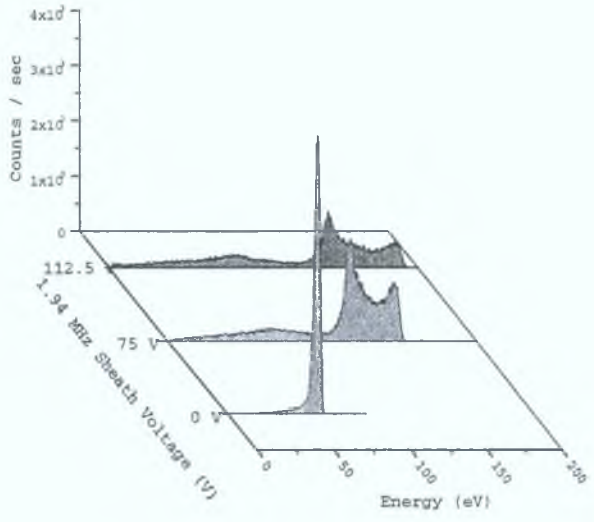

Figure 5.26: *Xe^+ IEDF in Hydrogen admixture Xenon discharge for $V_{27.12MHz} = 37.5V$ and 5 Pa at various 1.94 MHz sheath voltages*

plasma to compare sheath dynamics studies with experiments.

Dual frequency discharges are used in processing applications in order to achieve independent control of ion flux and ion impact energy onto the substrate. The higher frequency due to the larger displacement current is used to control the plasma density and thus ion flux onto the substrate. The lower frequency is used to control the ion bombardment energy on the substrate. Results show that the 27.12 MHz voltage can be used to control the ion flux impinging on the electrode surface. However, the IEDF of H_3^+ ions is broad and complex. The structures of the IEDFs are quite different to those from typical single frequency sheaths. Influences of ions experiencing time varying oscillations of both frequencies can be recognised. This is not a desired distribution of the impact energy onto substrates in processing plasmas.

In typical processing applications at the frequencies used, 1.94 MHz and 27.12 MHz, the discharges typically contain heavier ions. Heavier ions at these frequencies cannot respond to the rf modulation of the sheath potential, but experience a time-averaged potential. The IEDF in this case would be similar to that expected for a dc sheath, a narrow distribution peaked at the time-averaged

sheath potential. To investigate these heavier ions, Xe^+ ions were used in a hydrogen discharge with an admixture of Xe. The IEDFs of Xe^+ions do not posses the complex structures of H_3^+ IEDFs. They are too heavy to respond to the 27.12 MHz time variations and only slightly respond to the 1.94 MHz oscillations. The structures of their IEDFs are relatively narrow and quite similar to those of single frequency discharges, illustrating the basic concept of dual frequency CCRF discharges.

CHAPTER 6

Collapse of the plasma boundary sheath

So far high voltage boundary sheaths have been investigated. There is increasing current interest in using pulsed mode discharges to enable more flexibility and control of technological processes. It has been suggested that suppression of charge build up on substrates is attributed to sheath collapse in the post discharge, and annihilation of negative ion confinement. The collapse of the positive space charge sheath has been investigated in the afterglow of a pulsed inductively coupled rf plasma (ICP)[1]. However, investigations reveal that the sheath potential does not fully collapse in the post discharge.

6.1 Experimental setup

The ICP configuration is shown in figure 6.1. The discharge chamber is a modified GEC reference cell. Several modifications have been made to the original GEC cell in order to improve performance for inductive coupling. A bifilar antenna with 12 cm diameter is used and the stainless steel housing around the antenna

[1]These experiments have been carried out in collaboration with the Institute for Atomic and Plasma Physics at the Ruhr University Bochum, Germany.

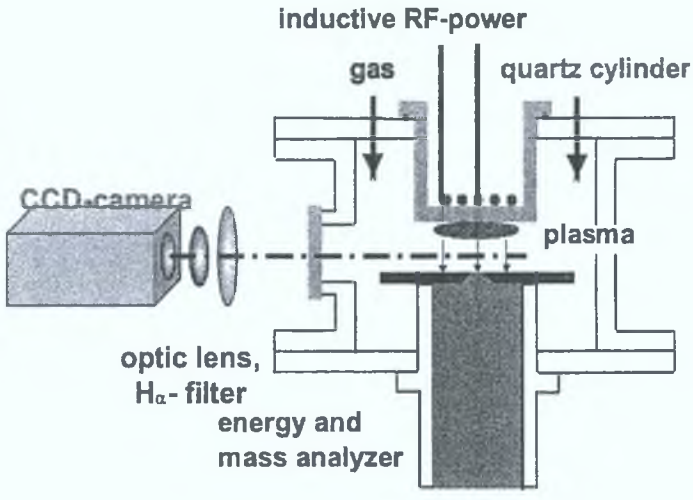

Figure 6.1: *Set-up of inductively coupled plasma*

was replaced by a quartz cylinder. At a distance of 5 cm below the antenna a grounded aluminium electrode limits the discharge region in the vertical direction. Gas is introduced into the chamber through four pipes bent towards the center of the discharge. The vacuum chamber, antenna and grounded electrode are water cooled. A mass resolved ion energy analyser (Balzers Plasma Process Monitor, PPM 422 [101]) is incorporated in the grounded electrode. An extraction orifice at the center of the grounded electrode allows for mass resolved ion energy analysis of the particles impinging on the surface. The PPM consists of an energy analyser and a quadrupole mass spectrometer. The operation principle of the Balzars PPM is similar to that of the Hiden EQP, discussed in section 1.5.

For accurate measurements of IEDFs a similar procedure, as described in chapter 3, based on simulations of ion trajectories and extensive experimental checks has been applied. Charge exchange collisions of H_2^+ ions are exploited for energy calibration.

The ICP is driven with an excitation frequency of 13.56 MHz. The rf power supply can be pulsed at variable frequencies and duty cycles. To perform time resolved measurements the detector of the PPM is connected to a multi channel scaler (MCS). The pulsed rf power supply is synchronised with the MCS card. The

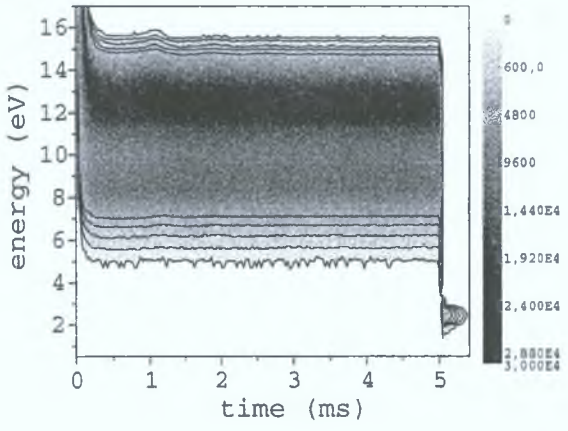

Figure 6.2: *Time resolved H_3^+ IEDFs in a pulsed hydrogen ICP; $f_{pulsing} = 100\,Hz$ (1:1 duty cycle), P = 300 W, p = 10 Pa.*

card (Ortec MCS-pci) has 65536 channels and a maximum temporal resolution of 100 ns.

6.2 Results

Figure 6.2 shows the time resolved H_3^+ IEDF in a pulsed hydrogen discharge with a pulsing frequency of 100 Hz and a 1:1 duty cycle. The rf power in the on phase is 300 W and the gas pressure 10 Pa. At time, $t = 0\,sec$, the discharge ignites capacitively with relatively high ion energies and undergoes a transition to a stable inductive mode within a few hundred micro seconds. The mean ion energy is around 13 eV in the inductive phase. In the afterglow, after switching off the rf power, the ion energy drops rapidly. However the ion energy does not fully relax to zero. A constant ion energy of a few eV is observed for several hundred micro seconds. This effect is discussed in detail in the following.

The H_3^+ IEDF in the afterglow is shown in figure 6.3. The pulsing frequency is 600 Hz. All other parameters are the same as in figure 6.2. After a transient phase between the plasma-on phase and the afterglow, a constant ion energy of

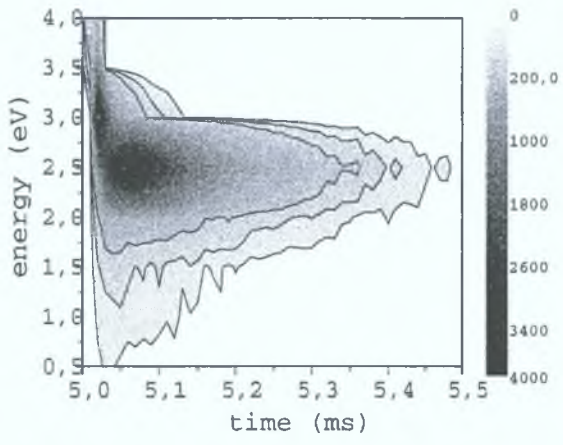

Figure 6.3: *Time resolved H_3^+ IEDFs in the afterglow of a pulsed hydrogen ICP*

about 2.5 eV is observed. This ion energy does not decrease, the plasma density decays faster. The sheath in the afterglow of the discharge does not fully collapse. A sheath with a potential of about 2.5 eV survives in the post discharge when the rf power is turned off. Using equation 1.13, the electron temperature can be determined from the ion energy. An ion energy of about 2.5 eV corresponds to a plasma boundary sheath potential caused by electrons of about 0.5 eV.

The IEDF of He^+ in the afterglow of a helium discharge exhibits different time behaviour. Figure 6.4 clearly shows that the ion energy relaxes to zero - the plasma boundary sheath collapses completely. An explanation of the difference to hydrogen can be an energy transfer from vibrationally excited molecular hydrogen to electrons in the afterglow of the hydrogen discharge. In the plasma on phase vibrationally excited molecules are produced through electron impact. When the power is turned off electrons quickly lose energy through either diffusion or collisions with the background gas. Under the conditions here it can be assumed that the losses are mainly through diffusion. This is observed, in the transient phase in figure 6.2, as a rapid decay in the ion energy to a quasi-stationary value of 2.5 eV. In the post discharge regime, vibrationally excited molecules have a long lifetime, several hundred microseconds [102], compared to the plasma decay.

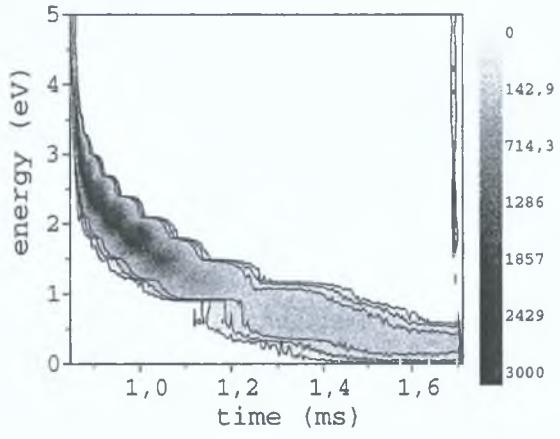

Figure 6.4: *Time resolved He^+ IEDFs in the afterglow of a pulsed helium ICP; $f_{pulsing} = 600\,Hz$ (1:1 duty cycle), $P = 300$ W, $p = 10$ Pa.*

Therefore electrons can gain energy by super elastic collisions with vibrationally excited molecules. In the afterglow the electron temperature is strongly correlated to the vibrational excitation of hydrogen molecules in the plasma on phase. Therefore, the higher the vibrational excitation in the discharge on phase the greater the electron heating in the afterglow. When the discharge is turned on the electron temperature establishes rapidly. However, the vibrationally excited molecules build up on a time scale of several hundred microseconds. Therefore, the vibrational population can be controlled by varying the plasma on time. Figure 6.5 shows a plot of ion energy in the afterglow as a function of plasma on time. As the plasma on time is increased, the vibrational excitation of molecules increases and thus there is more electron heating in the afterglow. At 1 ms, the vibrational temperature of molecules in the discharge has completely built up and reached a steady state. A similar effect of the electron temperature not collapsing to zero in the afterglow has been observed through probe measurements in the afterglow of a pulsed filament discharge by Hopkins [103].

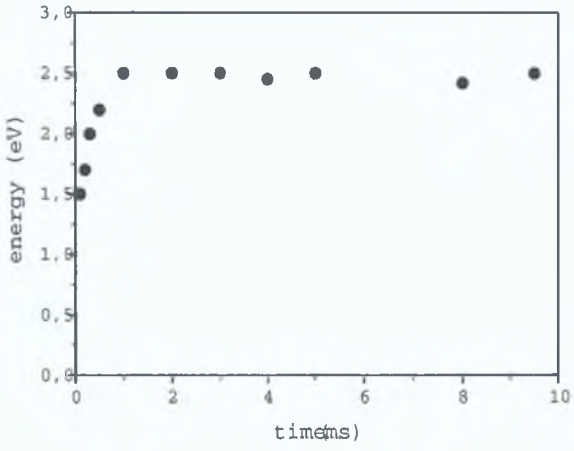

Figure 6.5: H_3^+ *ion energy as a function of plasma on time*

6.3 Conclusions

A non-zero electron temperature in the afterglow has been observed, the plasma boundary sheath does not collapse, charge suppression build up does not take place which could have important consequences for several technological applications using pulsed mode discharges. Further investigations with a combination of various diagnostic techniques, such as Langmuir probe measurements, optical emission spectroscopy [104] and particle-in-cell simulations are in progress. Furthermore investigations in deuterium with different gaps between the energy levels should provide additional information about the heating mechanism.

CHAPTER 7

Conclusions and Summary

The complex nature of multi frequency rf sheaths has been experimentally investigated. The final experimental design consists of a confined symmetric capacitively coupled rf discharge (chapter 2). The plasma can be generated in single and dual frequency operation. The resulting high voltage rf sheath in front of the grounded electrode has been investigated using a mass resolved ion energy analyser (Hiden EQP 2000) incorporated into the electrode.

Apart from the technological importance of hydrogen containing discharges, hydrogen acts as the perfect discharge gas for fundamental investigations for two primary reasons. Firstly, at typical technologically used radio-frequencies (e.g. 13.56 MHz), the relatively light hydrogen ions respond best to the time dependence of the sheath potential, allowing for detailed investigations of the sheath dynamics. Secondly, hydrogen is the simplest molecular gas with the most extensive data set for collisional cross-sections, making it suitable for comparison to simulations.

The sheath dynamics and the sheath chemistry in hydrogen discharges have been experimentally investigated and compared to 2D-PIC simulations (chapter

4). Special emphasis, for direct comparison, has been made in the experiment and the simulation (section 3.3). The geometry of the confined symmetric discharge allows for a perfect adoption of the simulation to the specific experimental conditions. A direct comparison of the experiment to the simulation is, nevertheless, rather challenging because of inherent difficulties in the measurement of ion energy distribution functions (IEDFs). Problems are mainly caused in the extraction of ions from the plasma into the analyser and chromatic aberration of the ion optics inside the analyser. A procedure to minimise chromatic aberration has been found and applied during this work (section 3.2). It is based on simulations of ion trajectories and extensive experimental checks. The energy dependent acceptance angle and the resulting energy dependent transmission function of the Hiden EQP 2000 has also been taken into account in the comparison of results from the experiment and the simulation.

Comparing absolute fluxes obtained from the experiment and the simulation is extremely challenging. In the simulation it requires an accurate description of the entire plasma. An accurate simulation of the plasma boundary sheath alone is not sufficient. Therefore the 2D-PIC code is coupled to a global model taking into account the complex chemistry of the plasma bulk [62]. An absolute calibration of the Hiden EQP 2000 is rather involving. A retarding field analyser can be used for a cross calibration.

In this work a much simpler novel procedure for absolute calibration has been developed and applied (section 4.2). It exploits the splitting of the saddle shape structure in the IEDF of ions traversing the rf sheath collisionless from the plasma bulk. The splitting depends on the sheath width. The sheath width is dependent on the plasma density and the electron temperature, and therefore related to the ion flux. It can be shown that the splitting is directly determined by the ion flux and the time averaged sheath potential, which can also be obtained from the IEDF. In conclusion, under certain conditions the absolute flux can be determined from the measured splitting and the measured time averaged sheath potential. The determined flux is used for absolute calibration of the Hiden EQP 2000.

Comparisons of the experiment and the 2D-PIC simulation have been carried out for absolute fluxes and IEDFs of the three hydrogen ions, H^+, H_2^+ and H_3^+, under parameter variations in hydrogen discharges operated with single frequencies at 13.56 MHz and at 27.12 MHz. The agreement is generally extremely good. Minor discrepancies can be attributed to slightly lower plasma densities and therefore slightly larger sheath widths in the simulation.

H_3^+ ions are predominately created in the plasma bulk while H^+ ions and H_2^+ ions are mainly formed through collisions in the sheath. Therefore, for essentially collisionless sheaths the IEDFs of H_3^+ ions reflect the sheath dynamics. This is obvious in the so called saddle shape structure as previously mentioned in the calibration procedure. As expected, the splitting increases with sheath voltage and decreases with rf frequency. The IEDFs of H_2^+ ions are strongly influenced by symmetric charge-exchange collisions. These collision processes produce secondary peaks in the IEDF. The number of peaks corresponds to the ratio of the ion transit time to the rf period. The mean energy of H^+ ions is also lower than the time averaged sheath potential due to its predominant formation within the sheath.

At high pressures, when the sheath becomes collision dominated, the IEDFs of all ions exhibit the expected exponential decay with energy. A surprising result is that more collision partners, at higher pressure, do not result in more conversion of H_3^+ ions to H_2^+ ions and H^+ ions through collisions in the sheath. The collision cross sections, for the responsible conversion processes, collision induced dissociation and asymmetric charge transfer, decrease towards lower energies. Therefore, higher densities of collision partners at higher pressures, are over-compensated by lower mean ion energies, resulting in smaller conversion cross sections and even less efficient total conversion. Accordingly, more efficient conversion is observed with increasing mean ion energy at higher sheath voltages. In discharges excited at 27.12 MHz less collision effects are observed in comparison to excitation at 13.56 MHz. This can be explained by smaller sheath width at 27.12 MHz caused by higher plasma densities due to more efficient electron heating.

Measurements in deuterium and hydrogen-deuterium mixtures have been carried out to get deeper insight into more complex plasma chemistry and sheath chemistry. The main difference between the pure hydrogen discharge and the pure deuterium discharge is a slightly lower plasma density in deuterium. This can be attributed to higher losses into vibrational states in deuterium due to the smaller spacing of vibrational levels. Measured IEDFs of specific ion masses, in hydrogen-deuterium mixtures, can reveal superpositions of two ion species. Comparing absolute fluxes and the shape of IEDFs to the pure hydrogen and deuterium cases provides information about the dominant species in different regions of the distribution function. This yields additional information about the plasma chemistry and the sheath chemistry.

A simple analytical model for the sheath dynamics in dual frequency rf discharges has been developed. The model is based on the corresponding single frequency model of Godyak [34]. It does not consider the full complexity of the sheath dynamics, but it clearly shows the basic phenomena.

The sheath dynamics of a hydrogen dual-frequency discharge at 1.94 MHz and 27.12 MHz has been investigated by measuring absolute fluxes and IEDFs of hydrogen ions. The measurements generally compare rather well to a dual-frequency-1D-PIC simulation. Discrepancies can be explained by lower plasma densities and therefore larger sheath widths in the simulation. The discrepancies are greater than in the comparison to the 2D-PIC simulation in the single frequency case. Nevertheless, the main effects and trends are the same in experiment and simulation.

Hydrogen ions almost perfectly respond to temporal variations of the sheath potential caused by the low frequency component. This results in quite broad IEDFs. The mean energy is determined by the averaged sheath potential of both frequencies. At low voltages of the high frequency component, the response of ions to high frequency oscillations is small and cannot be resolved. Consequently, the IEDF is mainly determined by the dynamics of the low frequency component and just shifted by the time averaged potential of the high frequency component.

At higher voltages of the high frequency component, effects due to the high frequency dynamics become obvious. The two peaks in the saddle shaped structure, corresponding to the low frequency dynamics, split into two peaks each. A double saddle shaped structure with four peaks is observed. The measurements compare well to the simulation and details of the double saddle shaped structure can be explained and reproduced by the developed simple analytical dual frequency sheath model mentioned above.

The concept of separate control of ion flux and ion energy by the two frequencies can be observed. The ion flux is mainly determined by the high frequency component. The IEDFs are strongly influenced by the low frequency component. However, IEDFs of hydrogen ions following the low frequency dynamics are very broad. This limits control and selectivity in technological processes. Ions in technological processes are, however, typically of relatively high mass. The influence of the dual frequency sheath dynamics on IEDFs of heavy ions has been investigated by small admixtures of xenon in the hydrogen discharge. The IEDFs of xenon ions are much narrower. Xenon ions do not respond to high frequency oscillations but influences of the low frequency dynamics are still observed. The relatively narrow IEDFs of xenon ions confirm the basic concept of dual frequency CCRF discharges allowing for more control and selectivity.

Additional flexibility and control can also be achieved by using pulsed mode plasmas. The collapse of the positive space charge sheath in the post discharge has been investigated in a pulsed inductively coupled hydrogen plasma. However, investigations reveal that the sheath does not fully collapse. Time resolved measurements of IEDFs show a constant ion energy for several hundred micro seconds in the afterglow. The existence of the corresponding sheath potential is explained by electron heating through vibrationally excited molecules in the post discharge.

In conclusion, extensive experimental investigations of high voltage multi frequency plasma boundary sheaths have been carried out and compared to PIC simulations. Details of the sheath dynamics and the sheath chemistry are well

understood. The experiment and the simulations generally agree well. Simulations can now be used for further detailed investigations under conditions which are difficult or impossible experimentally.

Appendix A

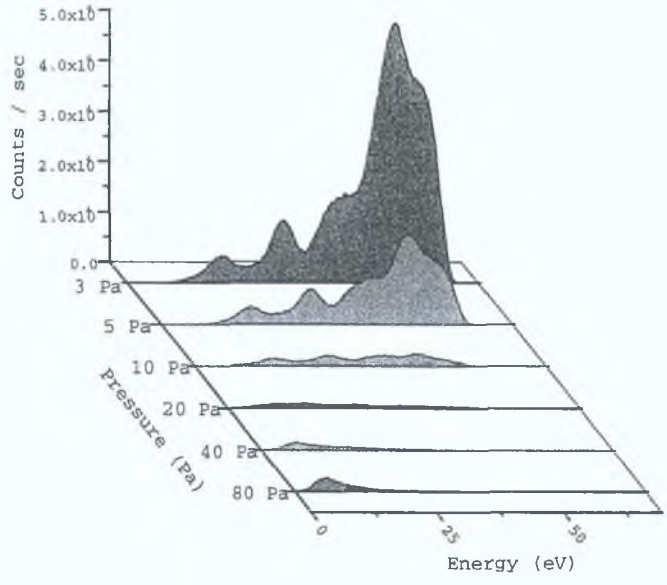

Figure 7.1: *H_2^+ IEDF pressure variation, pure hydrogen 27.12 MHz discharge*

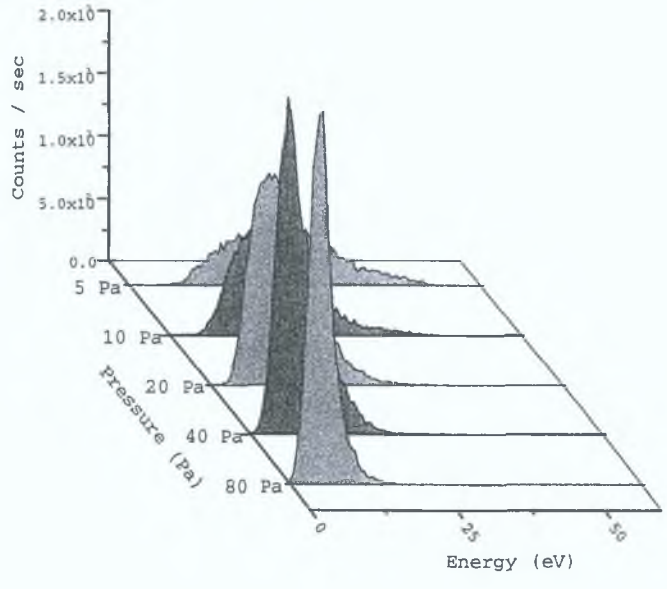

Figure 7.2: *D^+ IEDF pressure variation, pure deuterium 13.56 MHz discharge*

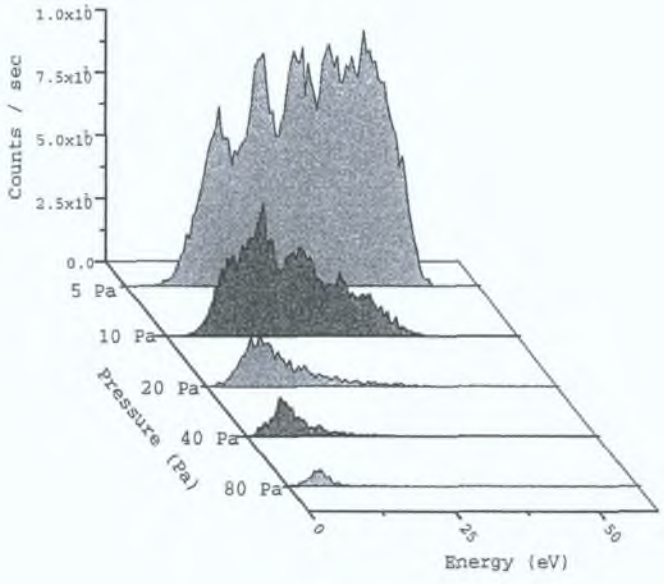

Figure 7.3: *D_2^+ IEDF pressure variation, pure deuterium 13.56 MHz discharge*

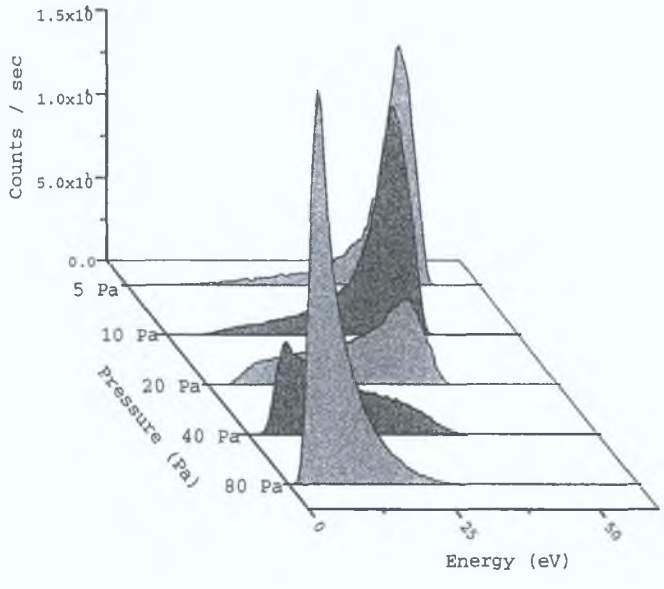

Figure 7.4: *D_3^+ IEDF pressure variation, pure deuterium 13.56 MHz discharge*

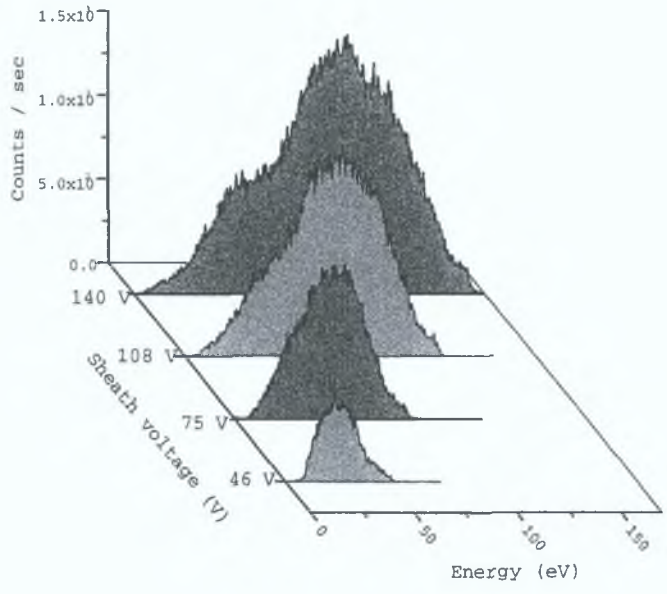

Figure 7.5: *D^+ IEDF voltage variation, pure deuterium 13.56 MHz discharge*

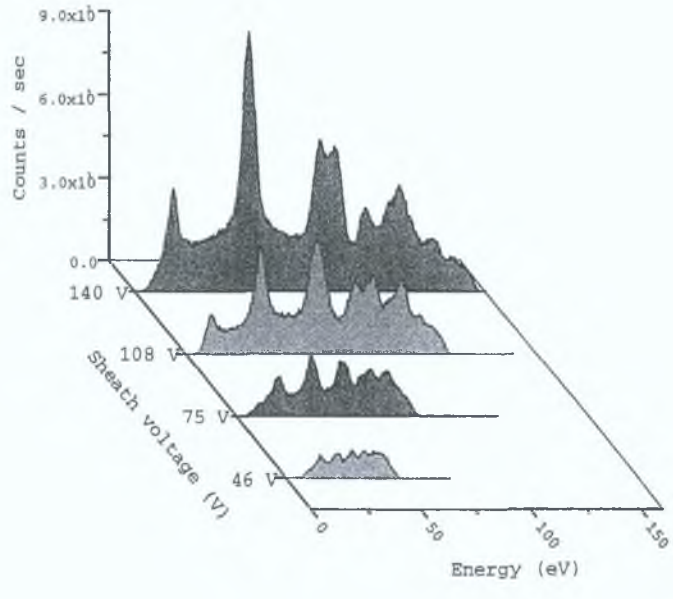

Figure 7.6: *D_2^+ IEDF voltage variation, pure deuterium 13.56 MHz discharge*

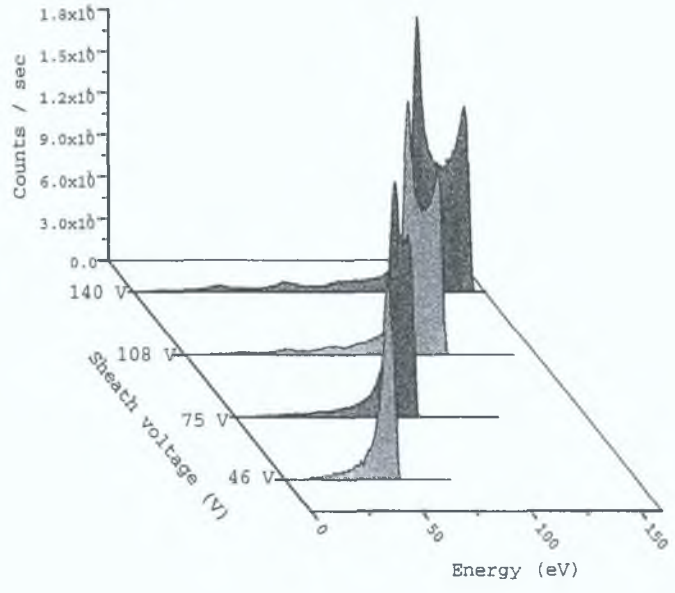

Figure 7.7: *D_3^+ IEDF voltage variation, pure deuterium 13.56 MHz discharge*

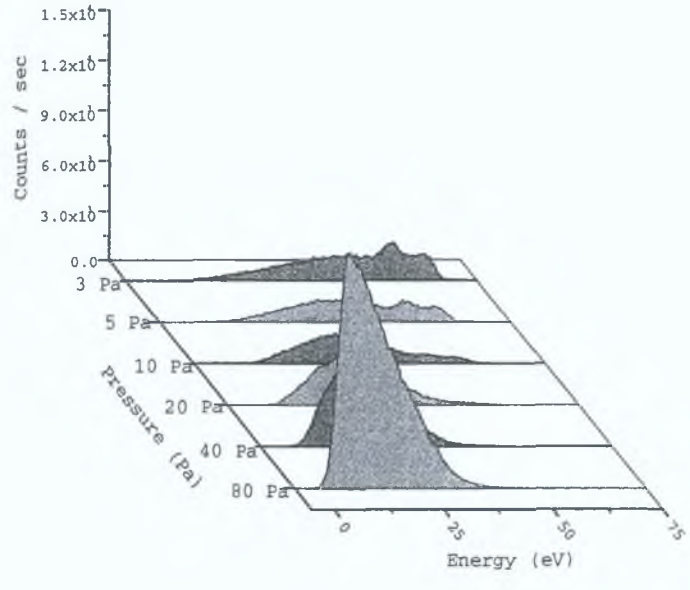

Figure 7.8: *D^+ IEDF pressure variation, pure deuterium 27.12 MHz discharge*

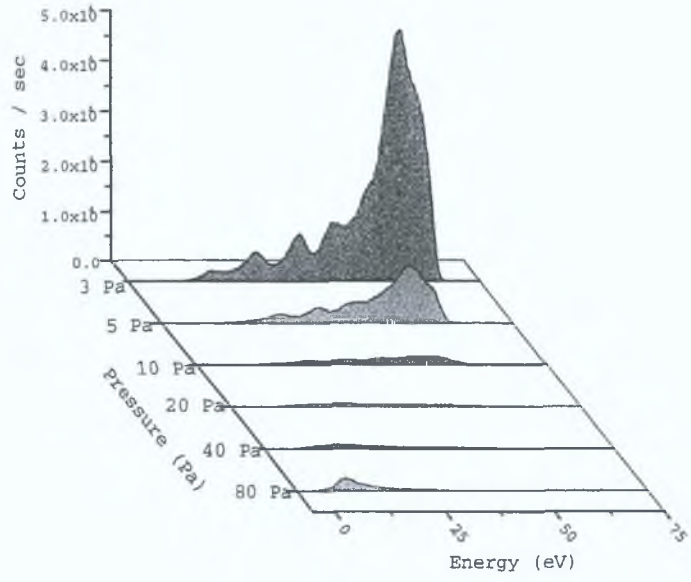

Figure 7.9: *D_2^+ IEDF pressure variation, pure deuterium 27.12 MHz discharge*

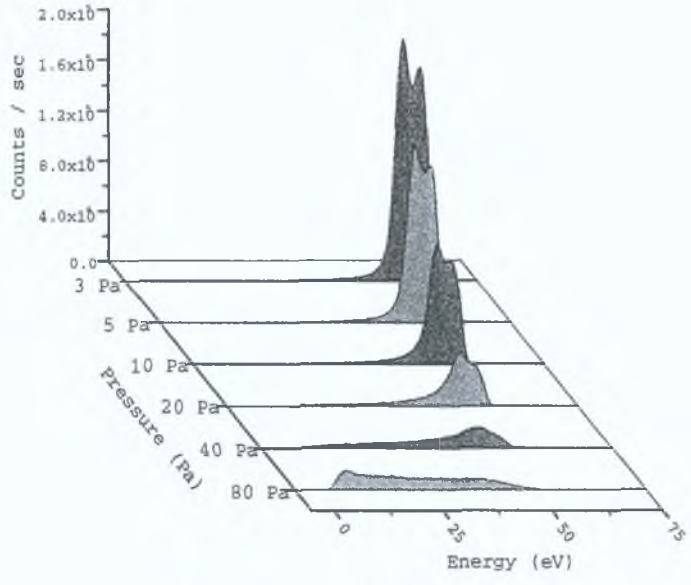

Figure 7.10: *D_3^+ IEDF voltage variation, pure deuterium 27.12 MHz discharge*

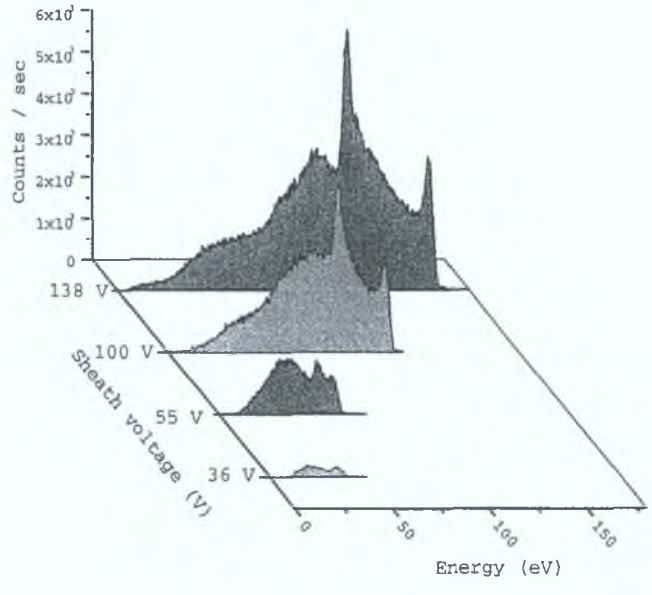

Figure 7.11: *D^+ IEDF voltage variation, pure deuterium 27.12 MHz discharge*

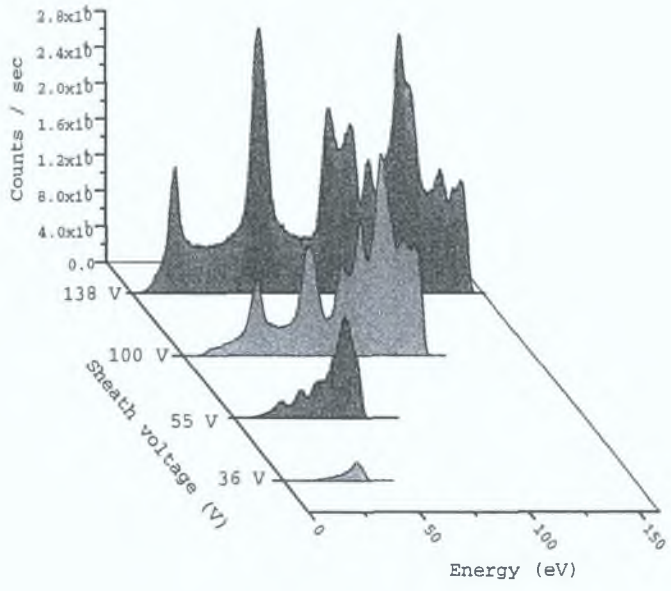

Figure 7.12: *D_2^+ IEDF voltage variation, pure deuterium 27.12 MHz discharge*

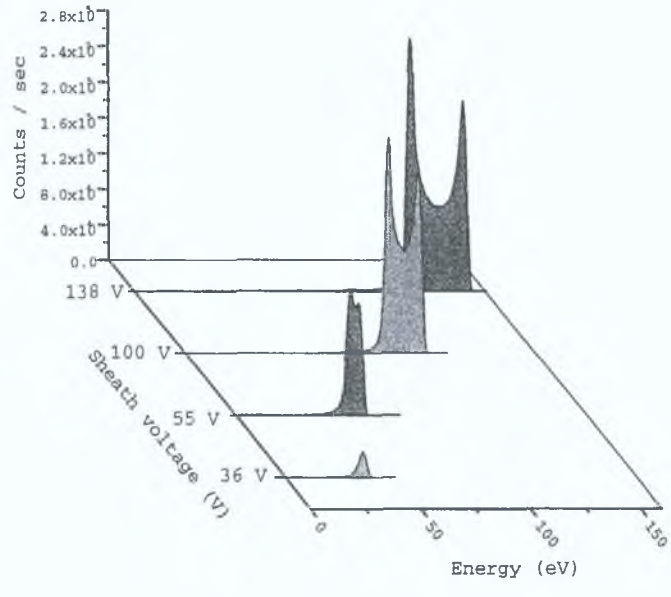

Figure 7.13: *D_3^+ IEDF voltage variation, pure deuterium 27.12 MHz discharge*

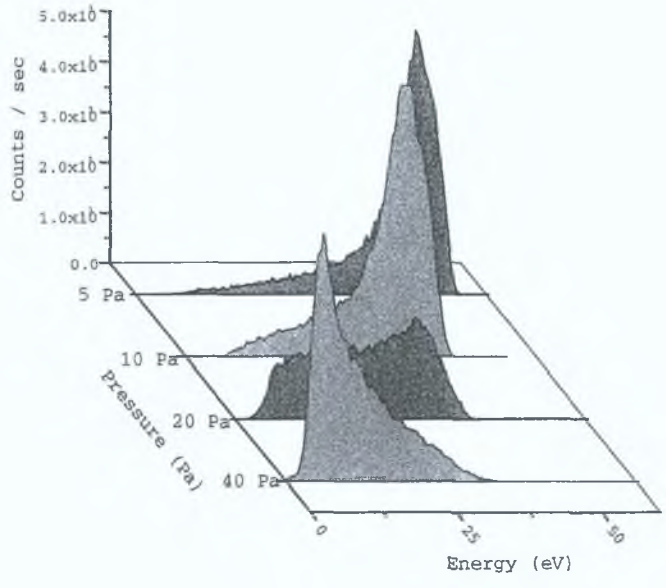

Figure 7.14: M_3^+ *IEDF pressure variation, 50 % hydrogen and 50 % deuterium mixture, 13.56 MHz discharge*

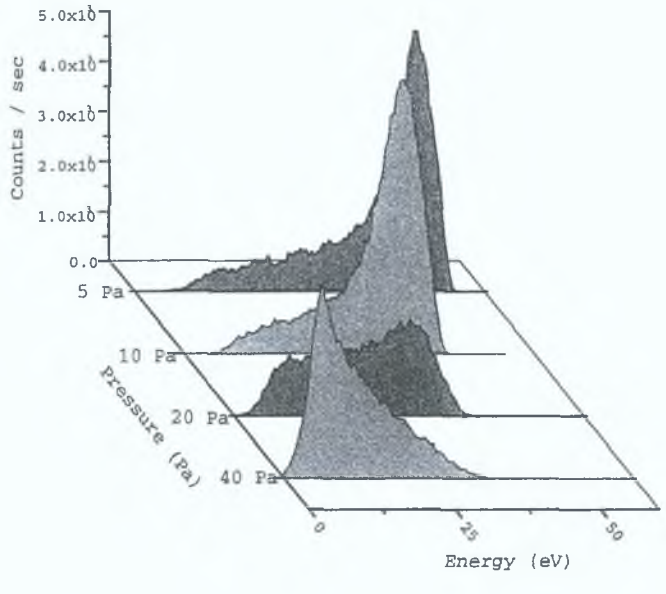

Figure 7.15: M_4^+ *IEDF pressure variation, 50 % hydrogen and 50 % deuterium mixture, 13.56 MHz discharge*

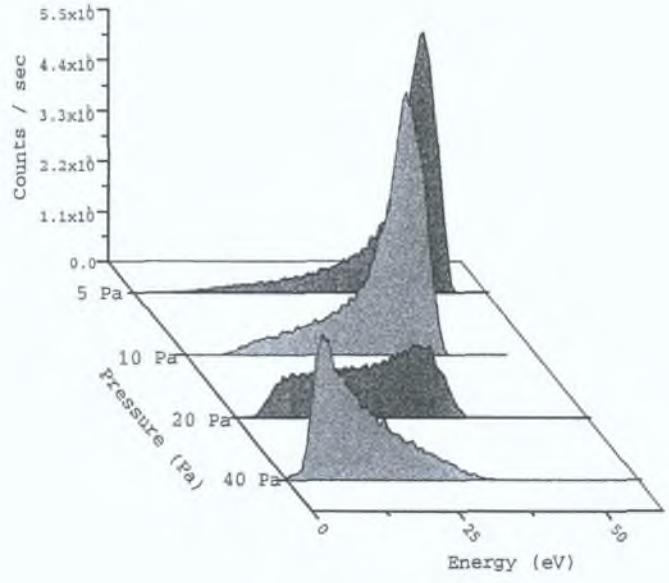

Figure 7.16: *M_5^+ IEDF pressure variation, 50 % hydrogen and 50 % deuterium mixture, 13.56 MHz discharge*

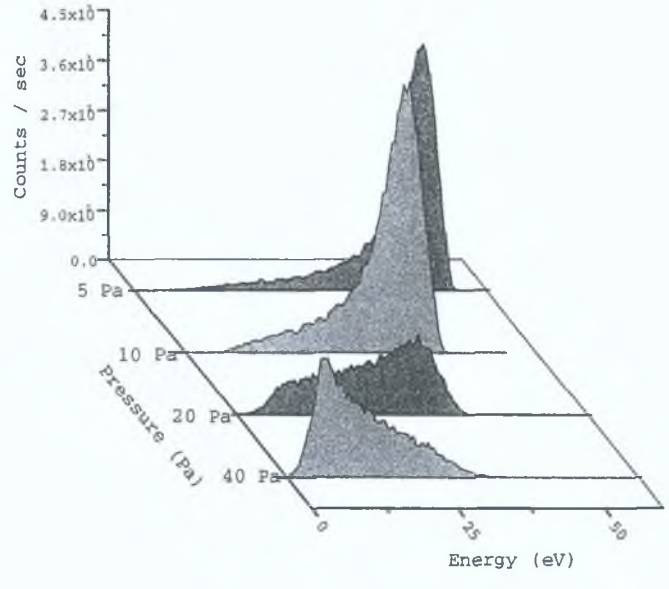

Figure 7.17: *M^+ IEDF pressure variation, 50 % hydrogen and 50 % deuterium mixture, 13.56 MHz discharge*

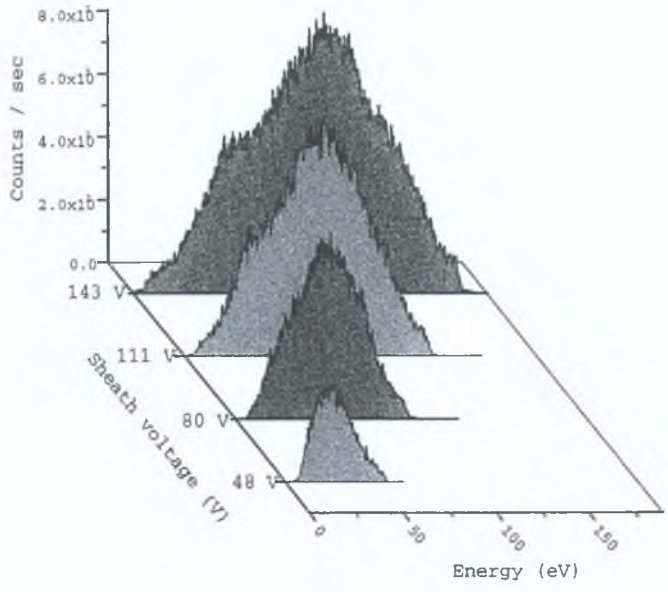

Figure 7.18: *M^+ IEDF voltage variation, 50 % hydrogen and 50 % deuterium mixture, 13.56 MHz discharge*

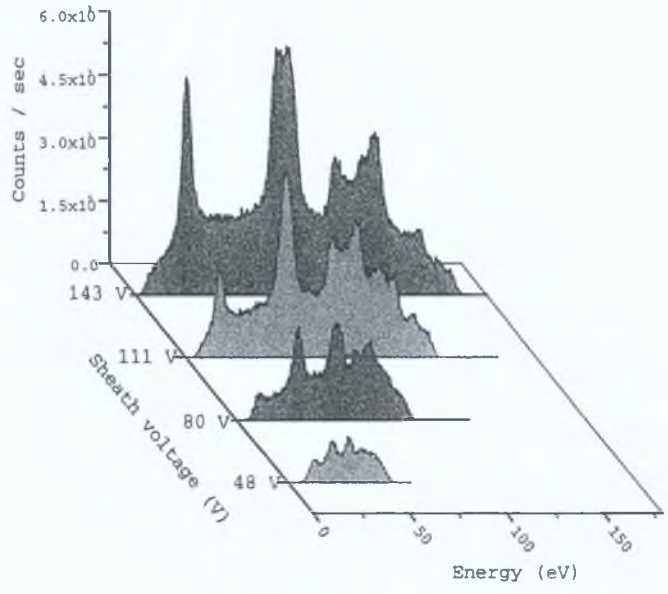

Figure 7.19: *M_2^+ IEDF voltage variation, 50 % hydrogen and 50 % deuterium mixture, 13.56 MHz discharge*

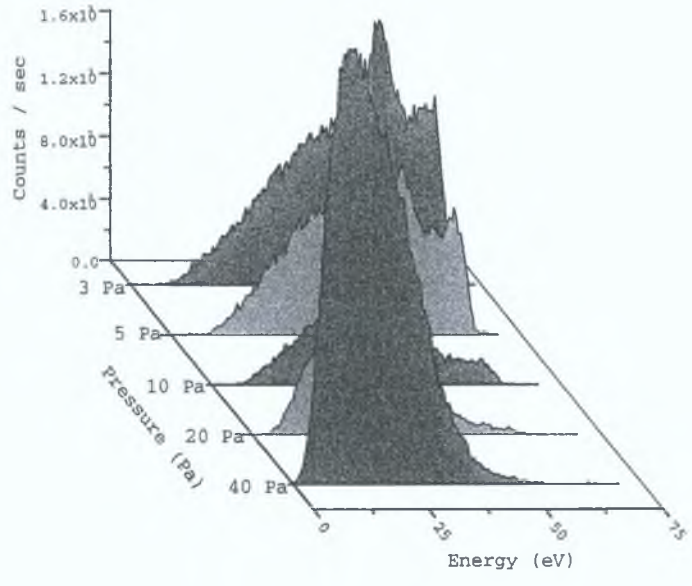

Figure 7.20: *M^+ IEDF voltage variation, 50 % hydrogen and 50 % deuterium mixture, 27.12 MHz discharge*

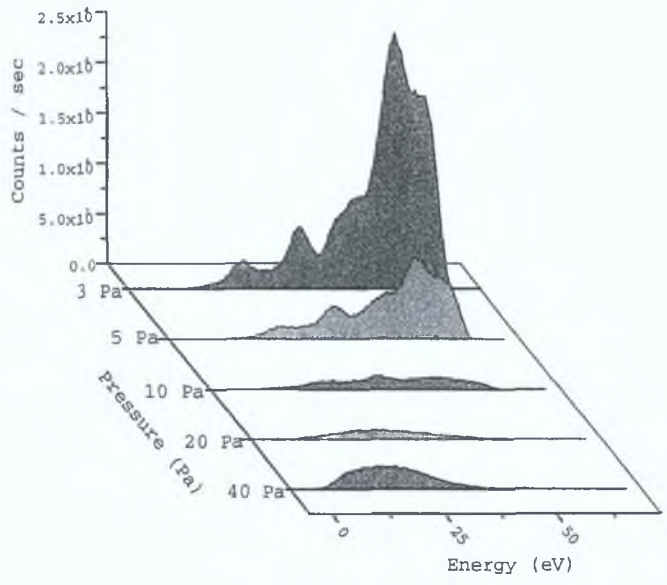

Figure 7.21: *M^+ IEDF voltage variation, 50 % hydrogen and 50 % deuterium mixture, 27.12 MHz discharge*

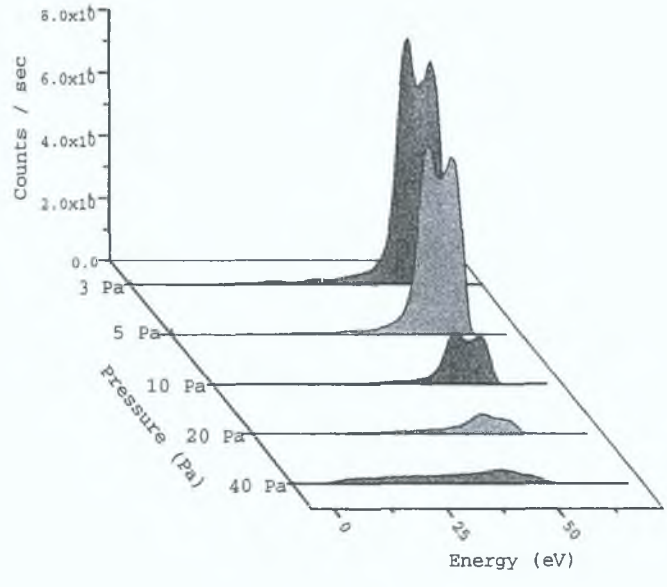

Figure 7.22: *M^+ IEDF voltage variation, 50 % hydrogen and 50 % deuterium mixture, 27.12 MHz discharge*

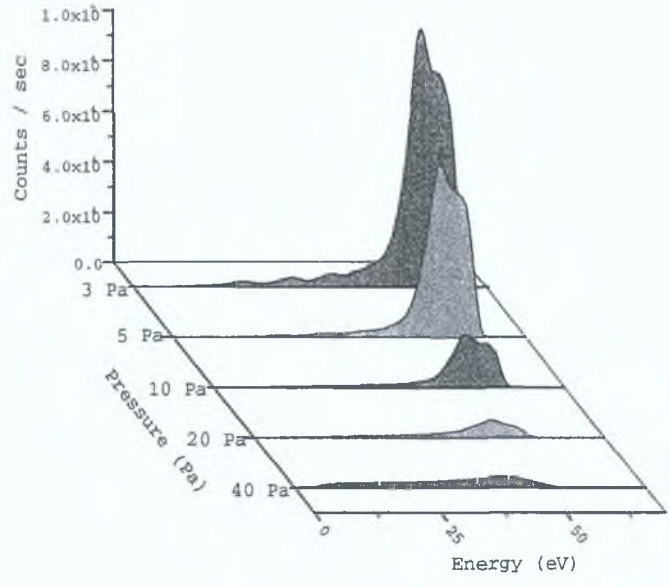

Figure 7.23: *M^+ IEDF voltage variation, 50 % hydrogen and 50 % deuterium mixture, 27.12 MHz discharge*

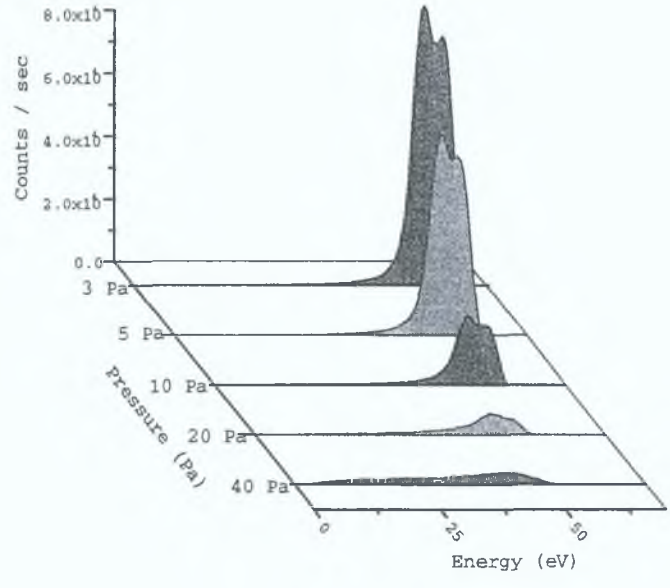

Figure 7.24: *M^+ IEDF voltage variation, 50 % hydrogen and 50 % deuterium mixture, 27.12 MHz discharge*

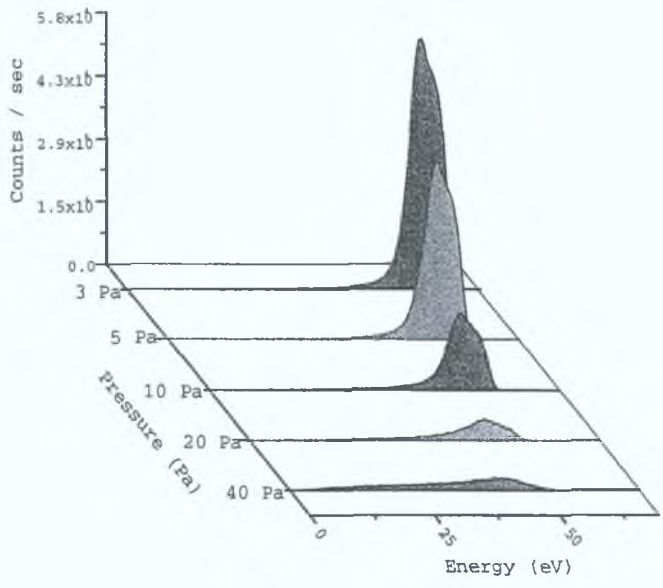

Figure 7.25: *M^+ IEDF voltage variation, 50 % hydrogen and 50 % deuterium mixture, 27.12 MHz discharge*

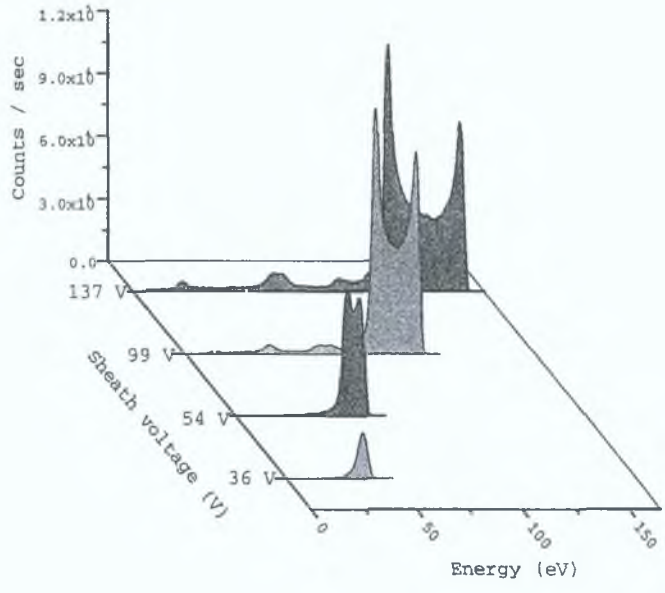

Figure 7.26: *M_3^+ IEDF voltage variation, 50 % hydrogen and 50 % deuterium mixture, 27.12 MHz discharge*

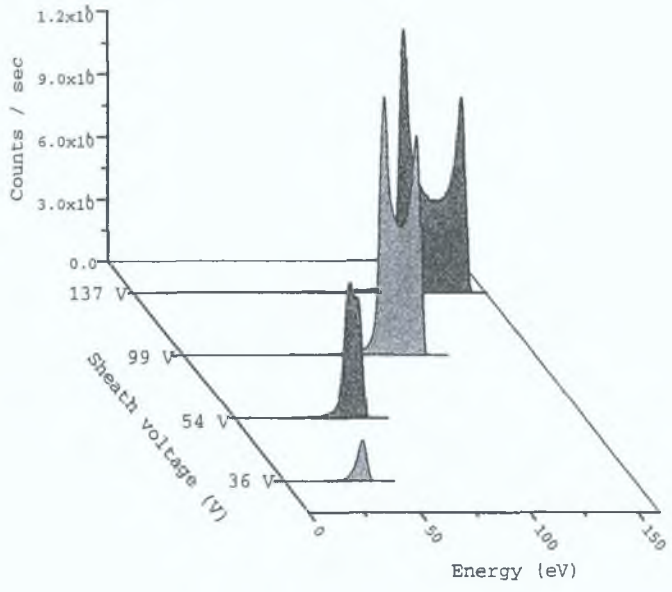

Figure 7.27: *M_5^+ IEDF voltage variation, 50 % hydrogen and 50 % deuterium mixture, 27.12 MHz discharge*

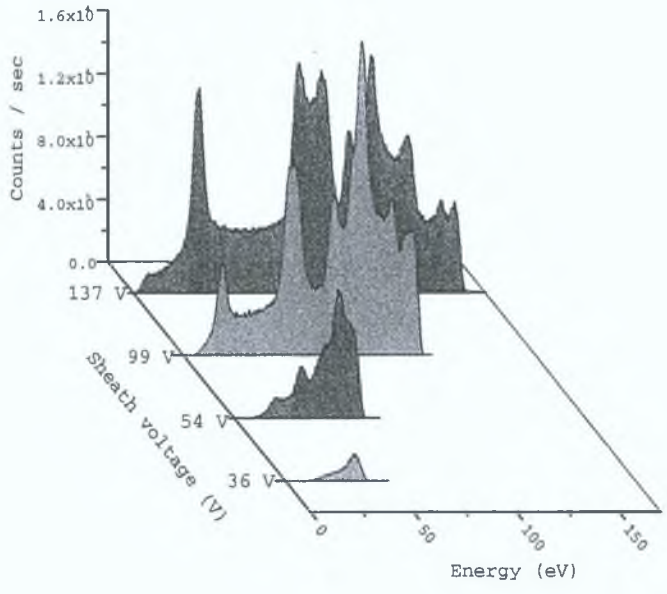

Figure 7.28: *M_2^+ IEDF voltage variation, 50 % hydrogen and 50 % deuterium mixture, 27.12 MHz discharge*

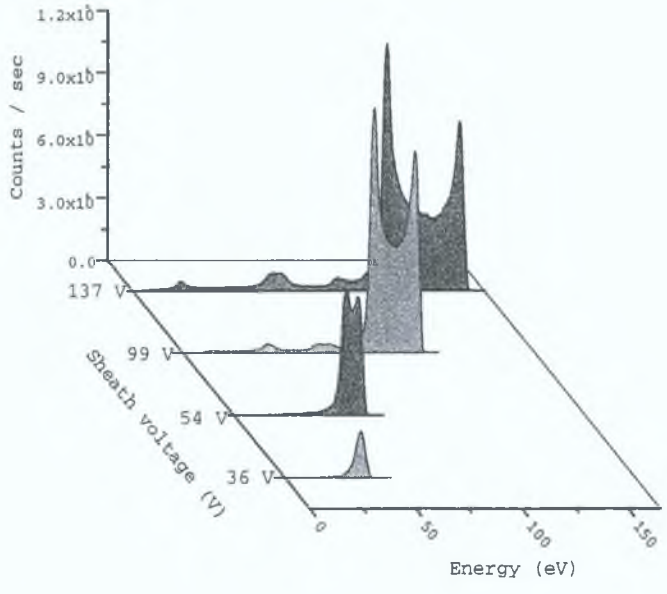

Figure 7.29: *M_3^+ IEDF voltage variation, 50 % hydrogen and 50 % deuterium mixture, 27.12 MHz discharge*

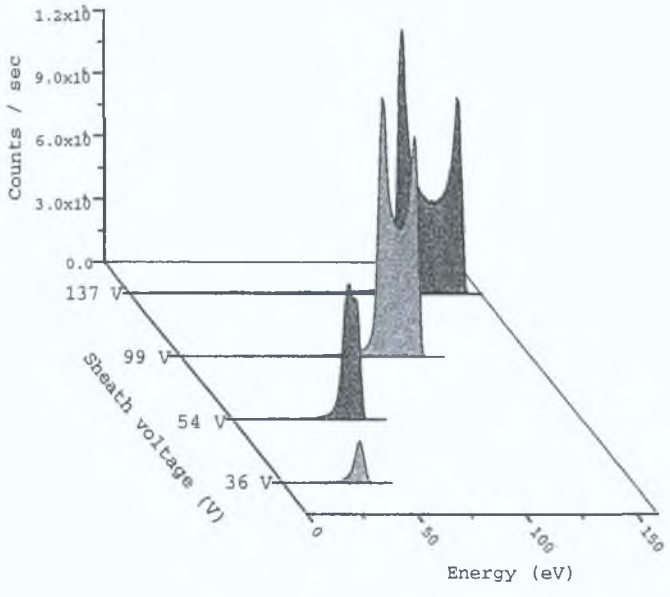

Figure 7.30: *M_5^+ IEDF voltage variation, 50 % hydrogen and 50 % deuterium mixture, 27.12 MHz discharge*

Appendix B

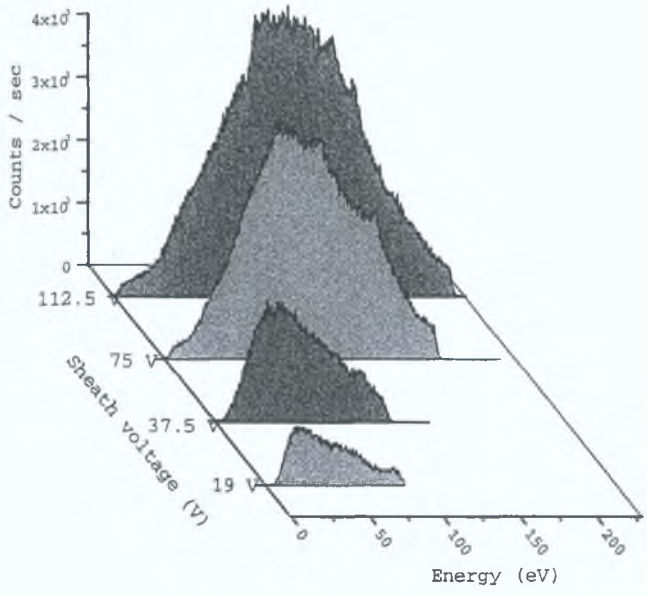

Figure 7.31: *H^+ IEDF in dual frequency hydrogen plasma, pressure variation*

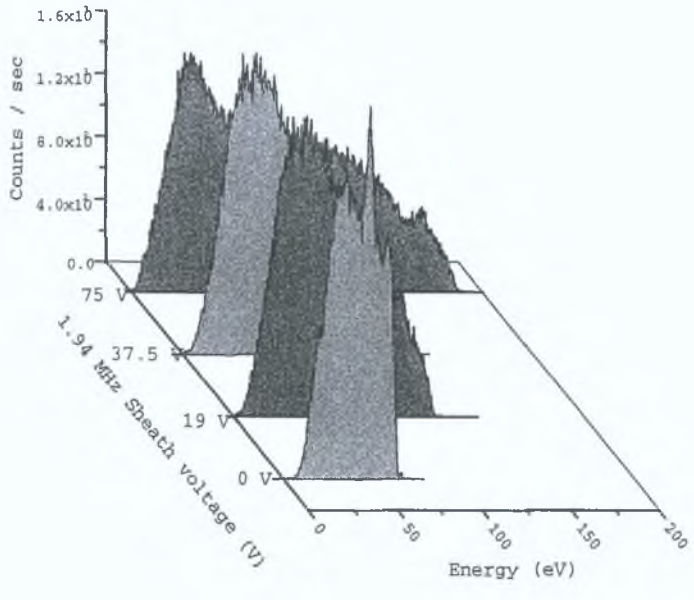

Figure 7.32: *H^+ IEDF in dual frequency hydrogen plasma, 1.94 MHz sheath voltage variation*

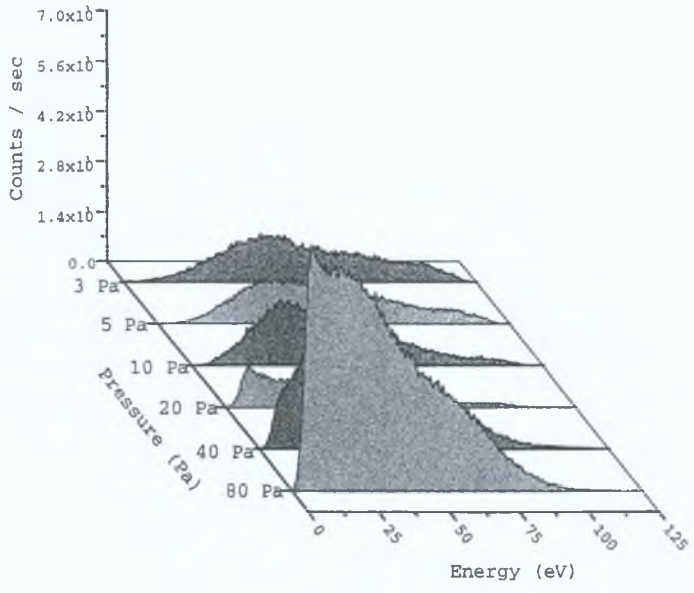

Figure 7.33: *D^+ IEDF in dual frequency deuterium plasma, pressure variation*

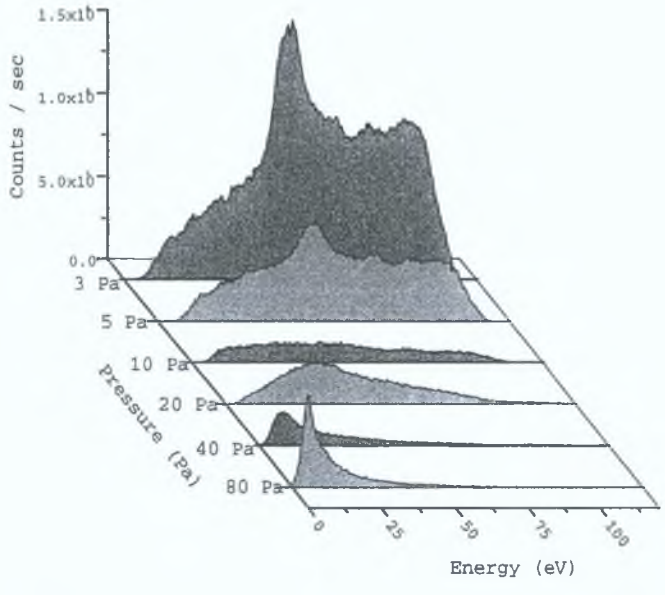

Figure 7.34: *D_2^+ IEDF in dual frequency deuterium plasma, pressure variation*

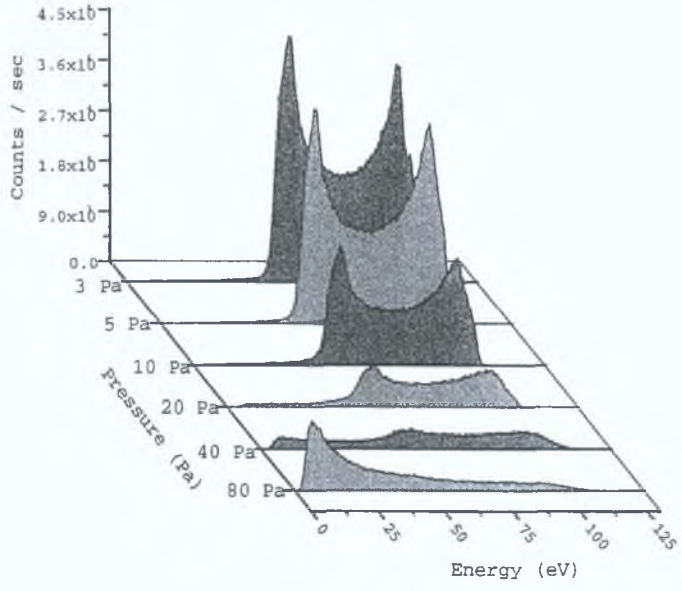

Figure 7.35: *D_3^+ IEDF in dual frequency deuterium plasma, pressure variation*

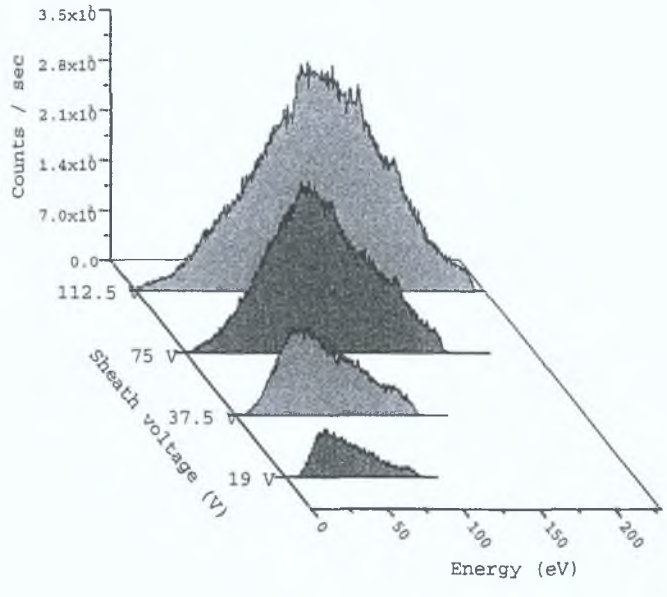

Figure 7.36: *D^+ IEDF in dual frequency deuterium plasma, 27.12 MHz sheath voltage variation*

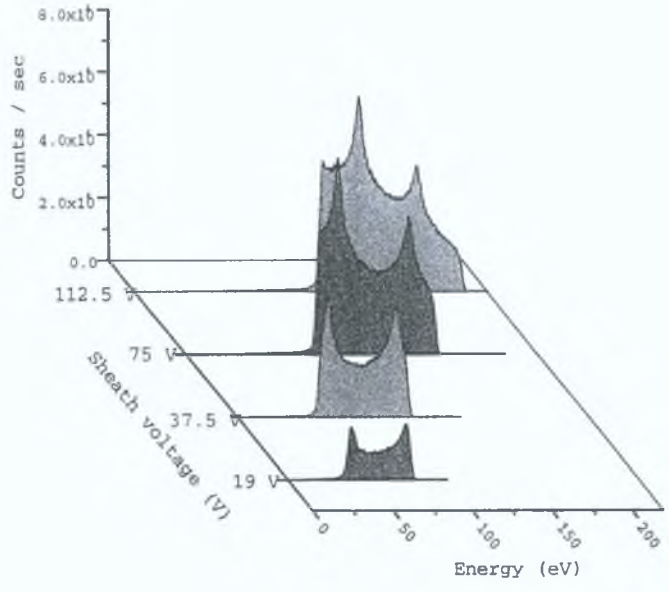

Figure 7.37: *D_3^+ IEDF in dual frequency deuterium plasma, 27.12 MHz sheath voltage variation*

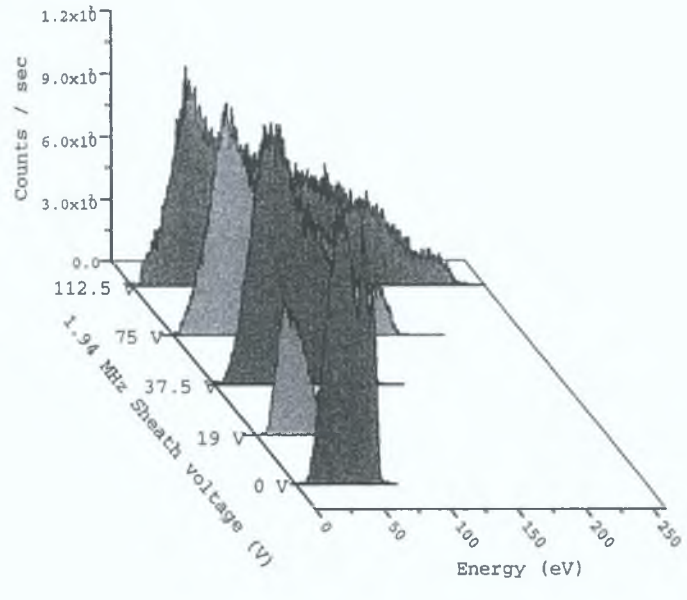

Figure 7.38: *D^+ IEDF in dual frequency deuterium plasma, 1.94 MHz sheath voltage variation*

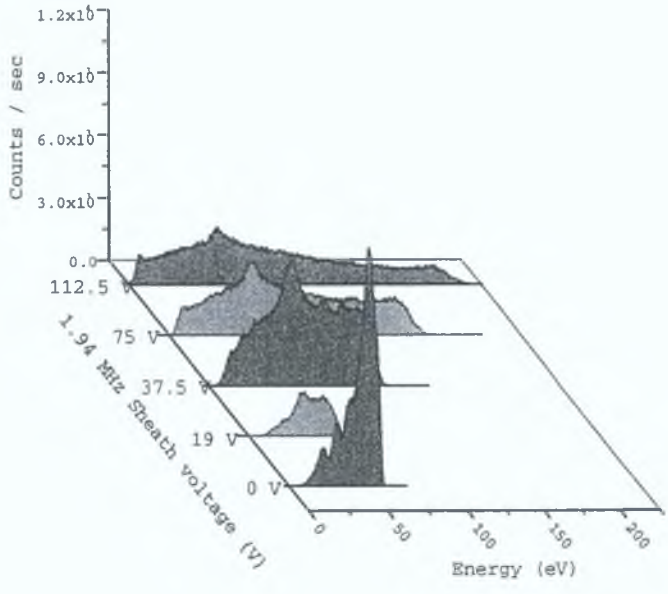

Figure 7.39: D_2^+ *IEDF in dual frequency deuterium plasma, 1.94 MHz sheath voltage variation*

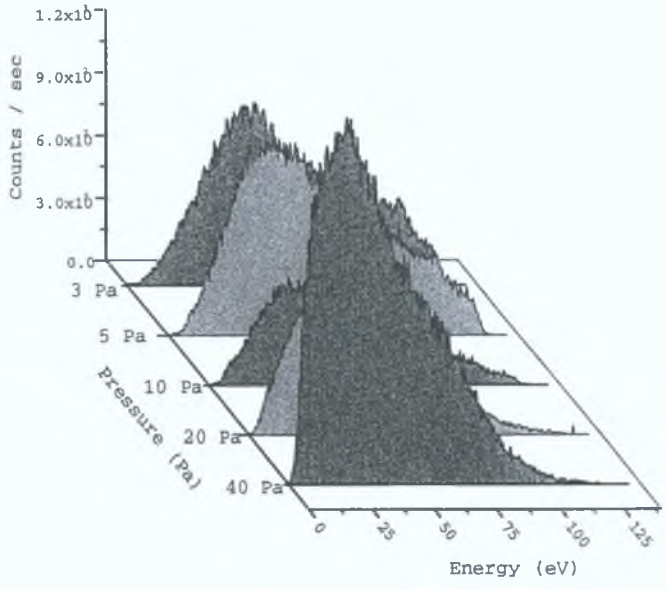

Figure 7.40: *Mass 1, IEDF in 50 % hydrogen - 50 % deuterium dual frequency plasma, pressure variation*

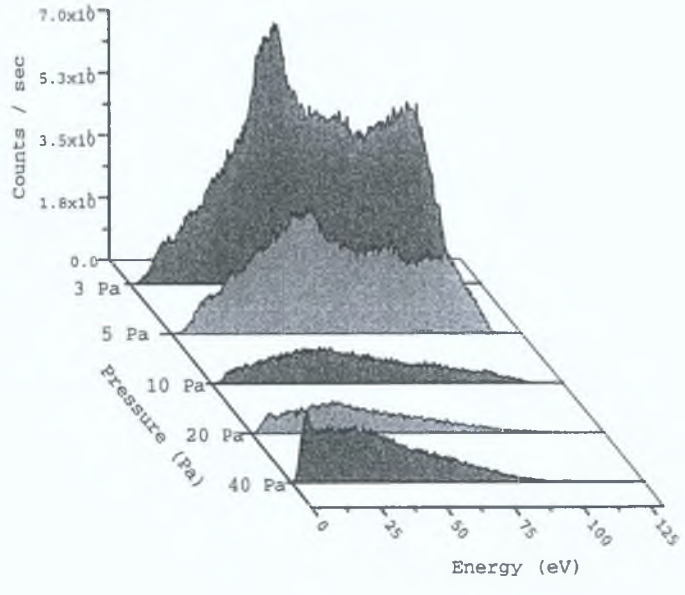

Figure 7.41: *Mass 2, IEDF in 50 % hydrogen - 50 % deuterium dual frequency plasma, pressure variation*

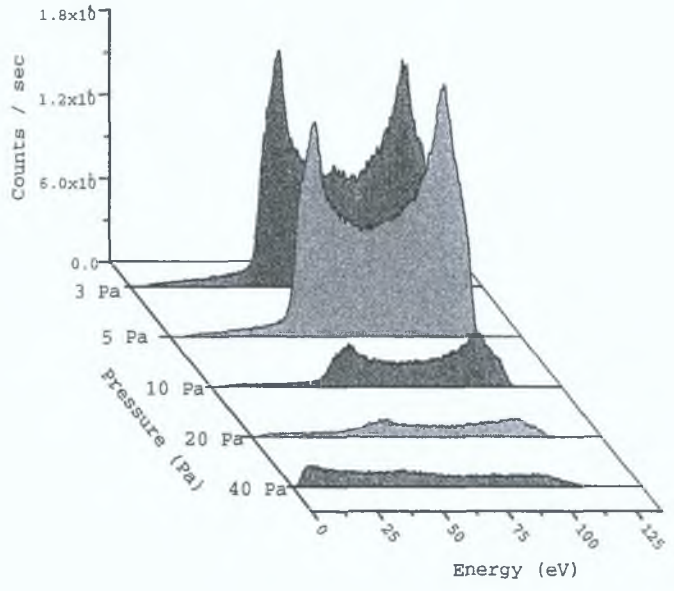

Figure 7.42: *Mass 3, IEDF in 50 % hydrogen - 50 % deuterium dual frequency plasma, pressure variation*

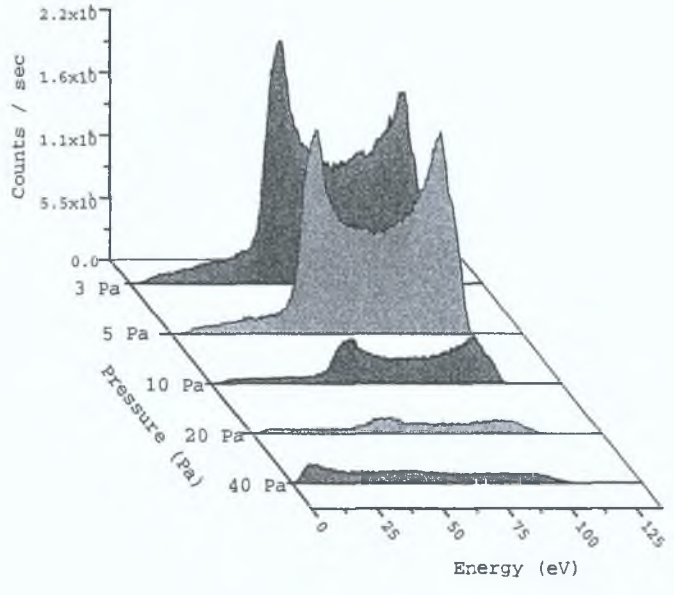

Figure 7.43: *Mass 4, IEDF in 50 % hydrogen - 50 % deuterium dual frequency plasma, pressure variation*

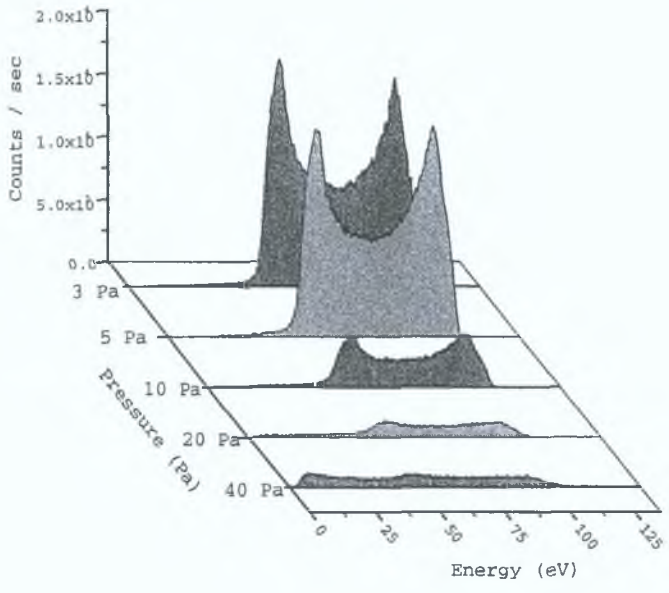

Figure 7.44: *Mass 5, IEDF in 50 % hydrogen - 50 % deuterium dual frequency plasma, pressure variation*

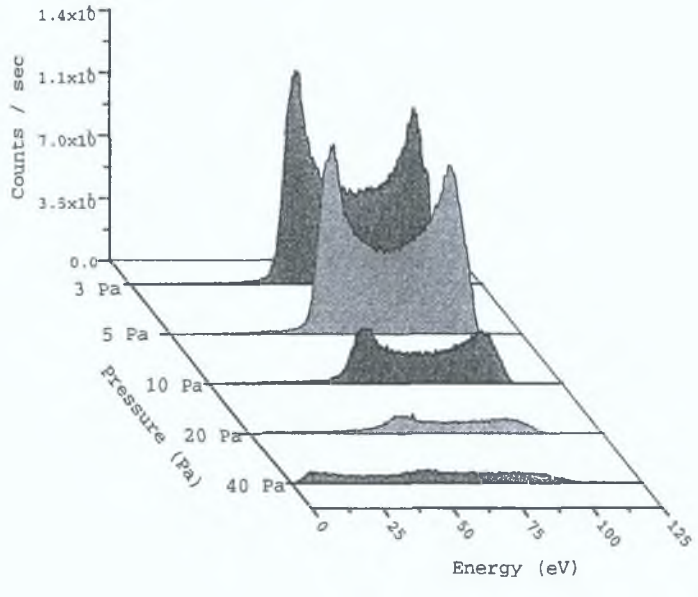

Figure 7.45: *Mass 6, IEDF in 50 % hydrogen - 50 % deuterium dual frequency plasma, pressure variation*

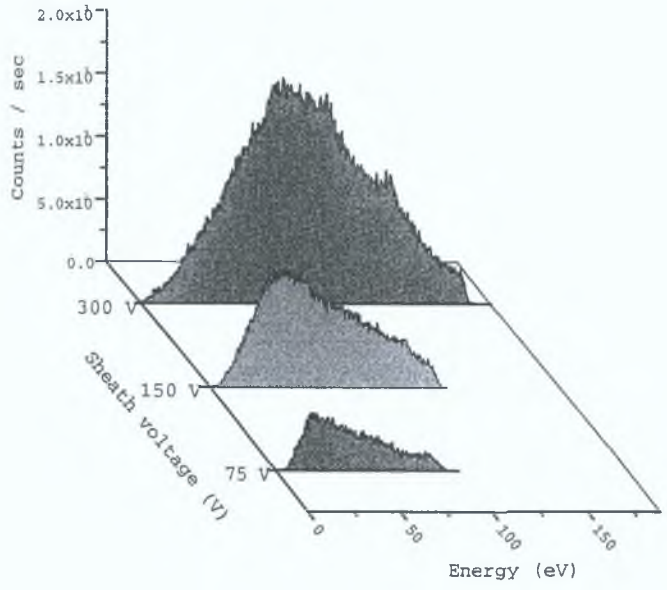

Figure 7.46: *Mass 1, IEDF in 50 % hydrogen - 50 % deuterium dual frequency plasma, 27.12 MHz sheath voltage variation*

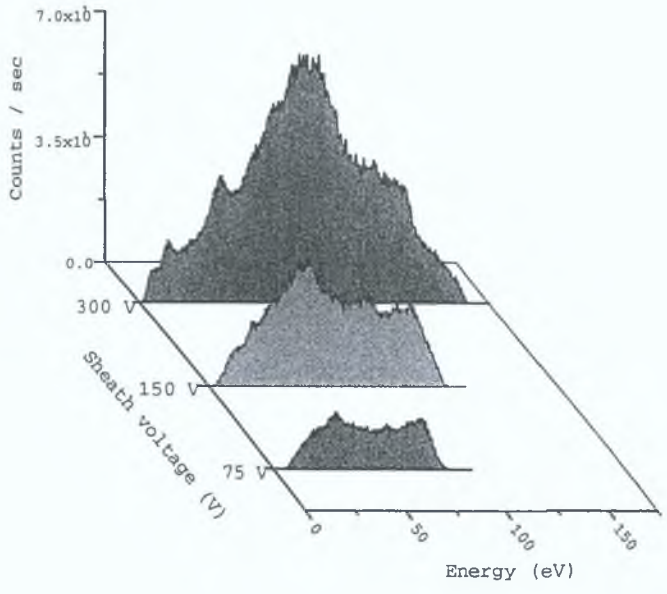

Figure 7.47: *Mass 3, IEDF in 50 % hydrogen - 50 % deuterium dual frequency plasma, 27.12 MHz sheath voltage variation*

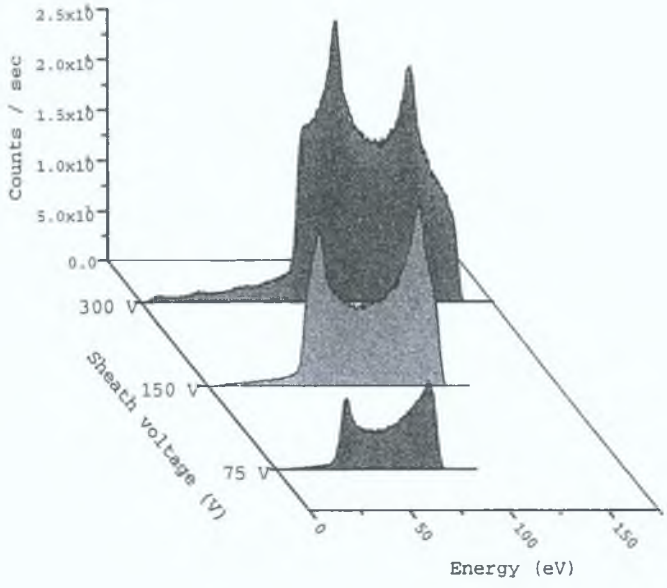

Figure 7.48: *Mass 3, IEDF in 50 % hydrogen - 50 % deuterium dual frequency plasma, 27.12 MHz sheath voltage variation*

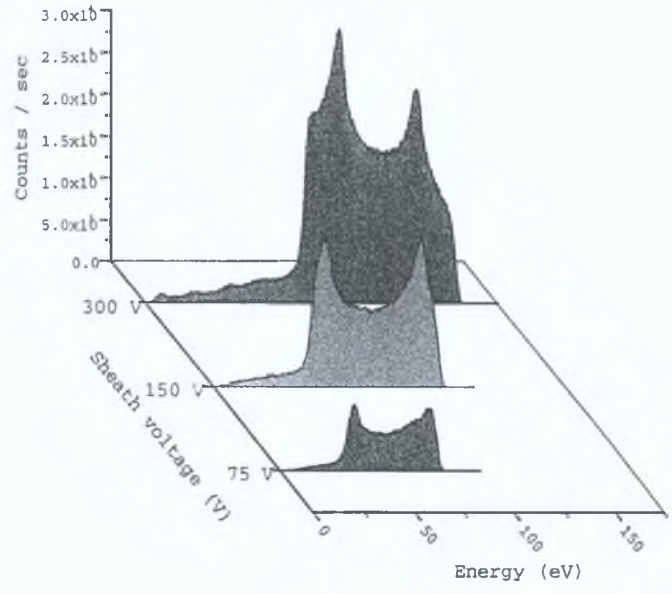

Figure 7.49: *Mass 4, IEDF in 50 % hydrogen - 50 % deuterium dual frequency plasma, 27.12 MHz sheath voltage variation*

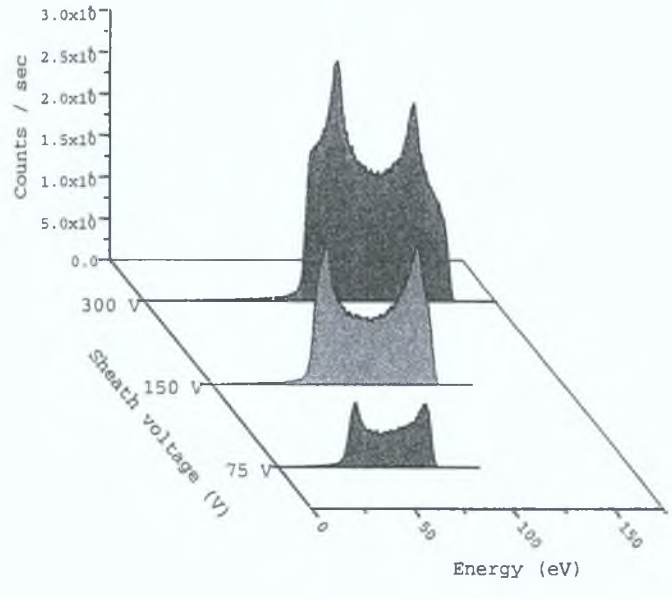

Figure 7.50: *Mass 5, IEDF in 50 % hydrogen - 50 % deuterium dual frequency plasma, 27.12 MHz sheath voltage variation*

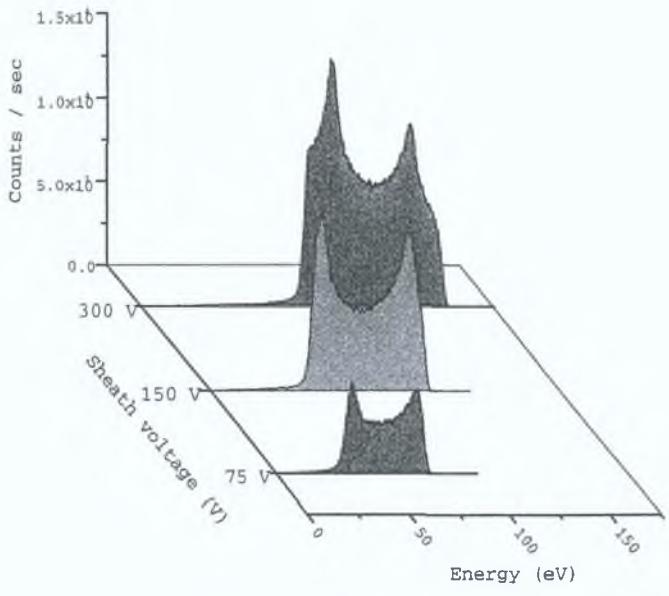

Figure 7.51: *Mass 6, IEDF in 50 % hydrogen - 50 % deuterium dual frequency plasma, 27.12 MHz sheath voltage variation*

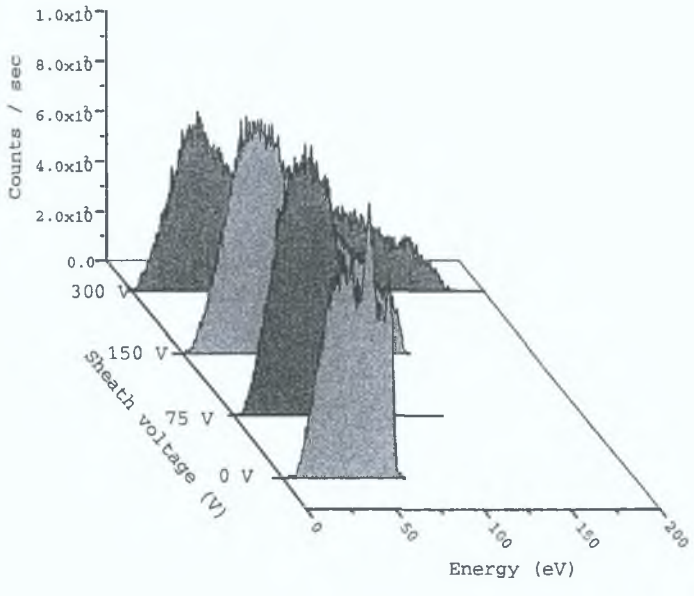

Figure 7.52: *Mass 1, IEDF in 50 % hydrogen - 50 % deuterium dual frequency plasma, 1.94 MHz sheath voltage variation*

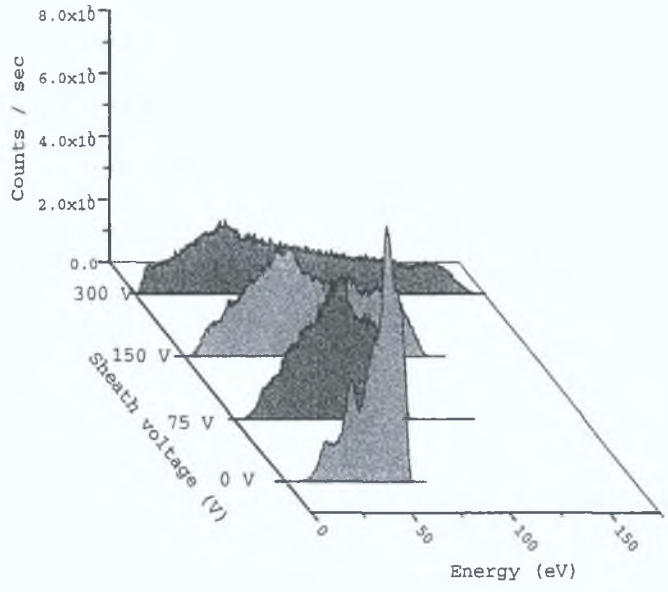

Figure 7.53: *Mass 2, IEDF in 50 % hydrogen - 50 % deuterium dual frequency plasma, 1.94 MHz sheath voltage variation*

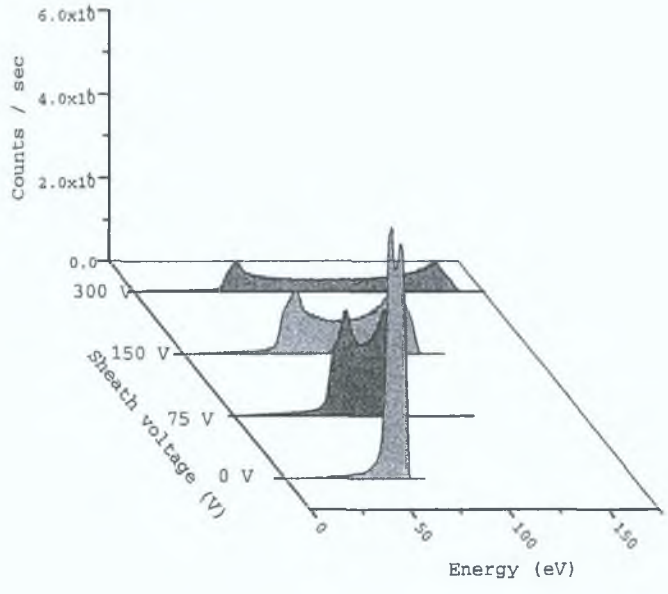

Figure 7.54: *Mass 3, IEDF in 50 % hydrogen - 50 % deuterium dual frequency plasma, 1.94 MHz sheath voltage variation*

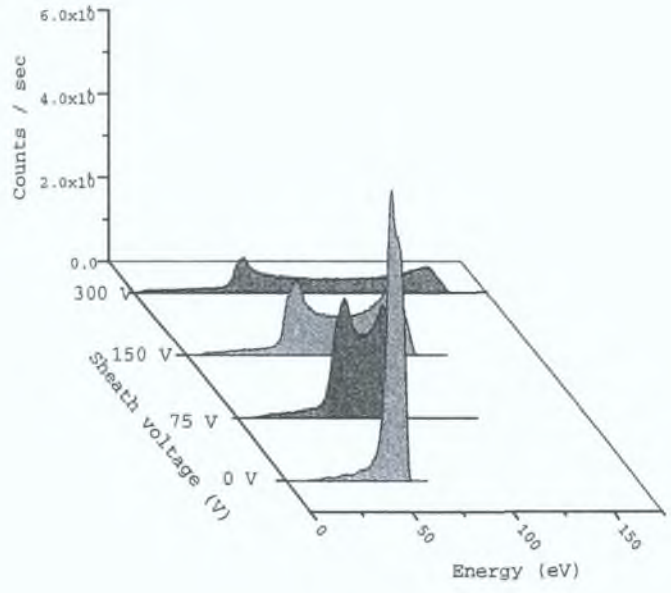

Figure 7.55: *Mass 4, IEDF in 50 % hydrogen - 50 % deuterium dual frequency plasma, 1.94 MHz sheath voltage variation*

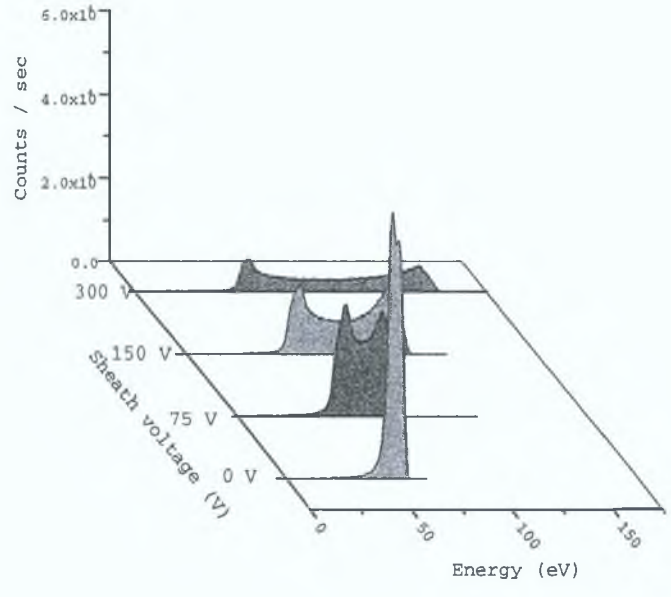

Figure 7.56: *Mass 5, IEDF in 50 % hydrogen - 50 % deuterium dual frequency plasma, 1.94 MHz sheath voltage variation*

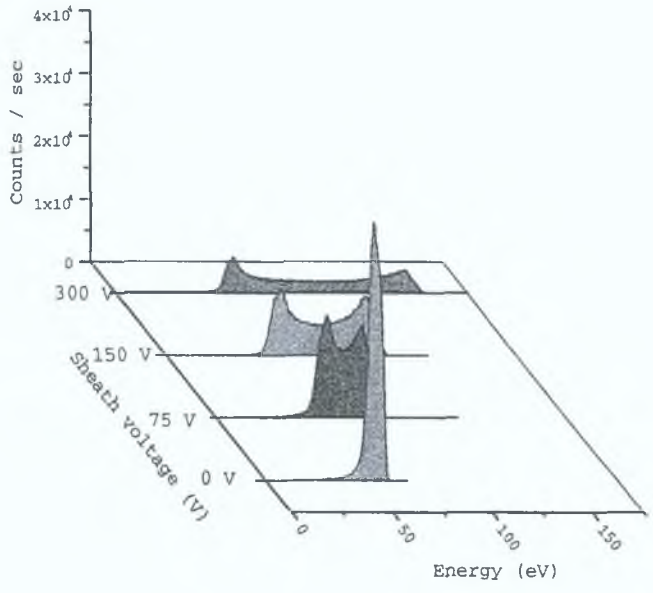

Figure 7.57: *Mass 6, IEDF in 50 % hydrogen - 50 % deuterium dual frequency plasma, 1.94 MHz sheath voltage variation*

Bibliography

[1] M. A. Lieberman and A. J. Lichtenberg, *Principles of Plasma Discharges and Materials Processing*, John Wiley & Sons Inc., New York (1994)

[2] B. Chapman, *Glow Discharge Processes*, John Wiley & Sons Inc., New York (1980)

[3] J. R. Roth. *Industrial Plasma Engineering.* Institute of Physics Publishing, Bristol and Philadelphia (1995)

[4] J. Hopwood, Plasma Sources Sci. Technol., 1 (1992) 109

[5] K. U. Riemann, J. Phys. D: Appl. Phys., 24 (1991) 493

[6] K. U. Riemann, *Theory of the plasma sheath transition*, General Invited Lecture at XXIV ICPIG Warschau 1999, J. Tech. Physics 41 1, Special Issue, 89 (2000)

[7] W. J. Goedheer, Plasma Sources Sci. Technol., 94 (2000) 507

[8] H Conrads and M. Schmidt, Plasma Sources Sci. Technol., 9 (2000) 441

[9] Y. P. Raizer, M. N. Shneider and N. A. Yatsenko, *Radio-Frequency Capacitive Discharges*, CRC Press Inc. (1995)

[10] K. Kohler, J. W. Coburn, D. E. Horne, and E. Kay, J. Appl. Phys., 57 1 (1985) 59

[11] V. A. Godyak, R. B. Piejak, and B. M. Alexandrovich, IEEE Trans. Plasma Sci., 42 4 (1990) 2299

[12] J. Hopwood, Plasma Sources Sci. Tech., 3 (1994) 460

[13] M. M. Turner and M. A. Lieberman, Plasma Sources Sci. Technol., 8 (1999) 313

[14] U. Kortshagen, N. D. Gibson and J. E. Lawler, J. Phys. D: Appl. Phys., 29 (1996) 1224

[15] I. M. El-Fayoumi, I. R. Jones, and M. M. Turner, J. Phys. D: Appl. Phys., 31 (1998) 3082

[16] V. A. Kadetov, *Diagnostic and modelling on an inductively coupled radio frequency discharge in hydrogen*, PhD thesis, Ruhr-Universität Bochum, Germany (2004)

[17] J. H. Keller, Plasma Sources Sci. Technol., 5 (1996) 166

[18] P. C. Boyle, A. R. Ellingboe, and M. M Turner, J. Phys. D: Appl. Phys., 37 5 (2004) 697

[19] H. H. Goto, H-D. Lowe, and T. Ohmi, J. Vac. Sci. Technol. A, 10 5 (1992) 3048

[20] H. H. Goto, H. D. Lowe, and T. Ohmi, IEEE Trans. Semi. Man., 6 1 (1993) 58

[21] T. Kitajima, Y. Takeo, and T. Makabe, J. Vac. Sci. Technol. A, 17 5 (1999) 2510

[22] T. Kitajima, Y. Takeo, Z. Lj. Petrovic, and T. Makabe, Appl. Phys. Lett., 77 4 (2000) 489

[23] J. Robiche, P. C. Boyle, M. M. Turner, and A. R. Ellingboe, J. Phys. D: Appl. Phys., 36 15 (2003)

[24] Surendra and D. B. Graves, Appl. Phys. Lett., 59 (1991) 2091

[25] M. A. Lieberman, IEEE Trans. Plasma Sci., 16 6 (1988) 638-644

[26] T. Panagopoulos and D. J. Economou, J. Appl. Phys., 85 (1999) 7

[27] V. A. Godyak, Phys. Rev. A, 42 (1990) 4

[28] N. Xiang and F. L. Waelbroeck, J. Appl. Phys., 95 (2004) 3

[29] M. Fivaz, S. Brunner, W. Schwarzenbach, A. A. Howling and ch. Hollenstein, Plasma Sources Sci. Technol., 4 (1995) 373

[30] Ute. Flender and K. Wiesemann, J. hys. D: Appl. Phys., 27 (1994) 509

[31] D. Bohm, In A. Guthry and R. K. Wakerling, *The Characteristics of Electrical Discharges in Magnetic Fields, chapter 3*, 77-86. MacGraw-Hill, New York (1949)

[32] W. D. Davis and T. A. Vanderslice, Phys. Rev., 131 1 (1963) 219

[33] C. V. Budtz-Jorgensen, PhD Thesis, Aarhus University, Denmark, Studies of Electrical Plasma Discharges

[34] V. A. Godyak, *Soviet Radio Frequency Discharge Research*, Delphic Associates, Inc., Falls Churcg, VA (1986)

[35] U. Czarnetzki, D. Luggenhölscher, and H.F. Döbele, Plasma Sources Sci. Technol., 8 (1999) 230

[36] U. Czarnetzki, D. Luggenhölscher, and H.F. Döbele, Appl. Phys. A, 72 (2001) 509

[37] E. Kawamura, V. Vahedi, M. A. Lieberman and C. K. Birdsall, Plasma Sources Sci. Technol., 8 R45-R64 (1999)

[38] C. Wild and P. Koidl, J. Appl. Phys., 69 9 (1991) 2909

[39] M. J. Kushner, J. Appl. Phys., 58 11 (1985) 4024

[40] R. T. Farouki, S. Hamaguchi and M. Dalvie, Phys. Rev. A, 45 (1992) 5913

[41] P. Benoit-Cattin and L C. Bernard, J. Appl. Phys., 39 12 (1968) 5723

[42] C. Wild and P. Koidl, Appl. Phys. Lett., 54 6 (1989) 505

[43] A.V. Phelps, J. Phys. Chem. Ref. Data, 19 (1990) 653

[44] T. Simko, V. Martisovits, J. Bretagne and G. Gousset, Phys. Rev. E, 56 (1997) 5

[45] D. Field, D. F. Klemperer, P. W. May and Y. P. Song, J. Appl. Phys., 70 1 (1991) 82

[46] P. Kae-Nune, J. Perrin, J. Guillon and J. Jolly, Plasma Souces Sci. and Tech., 4 (1995) 250

[47] H. Sugai and H. Toyoda, J. Vac. Sci. Technol., 10 4 (1992) 1193

[48] M. Zeuner and J. Meichsner, J. Appl. Phys., 80 2 (1996) 611

[49] J. K. Olthoff, R.J. Van Brunt and S. B. Radovanov, J. Appl. Phys., 72 10 (1992) 4566

[50] J. K. Olthoff, R.J. Van Brunt and S. B. Radovanov, J. A. Rees and R. Surowiec, J. Appl. Phys., 75 1 (1994) 115

[51] M. Zeuner, H. Neumann and J. Meichsner, Jpn. J. Appl. Phys., 36 1 7B (1997) 4711

[52] M. Zeuner, J. Meichsner and J. A. Rees, J. Appl. Phys., 79 12 (1996) 9379

[53] L. J. Overzet, Y. Lin and L. Luo, J. Appl. Phys., 72 12 (1992) 5579

[54] Hiden Analytical Ltd., 420 Europa Boulevard, Gemini business Park, Warrington. WA5 5UN, England. http://www.hiden.co.uk

[55] E. Stoffels, W. W. Stoffels, D. Vender, M. haverlag, G. M. W. Kroesen and F. J. De Hoog, Contrib. Plasma Phys., 35 4-5 (1995) 331

[56] W. W. Stoffels, E. Stoffels and K. Tachibana, Jpn. J. Appl. Phys. 36 1 7B (1997) 4638

[57] H. Wollnik, *Optics of Charged Particles*, Academic Press, San Diego, U.S.A. (1987)

[58] P. H. Dawson, *Quadrupole Mass Spectrometry and its Applications*, Elsevier Scientific Publishing Company (1976)

[59] M. J. Vasile and H. F. Dylla, *Mass Spectrometry of Plasmas in Plasma Diagnostics*, O. Auciello and D. Flamm (1989)

[60] R. Zorat, J. Goss, D. Boilson and D. Vender, Plasma Sources Sci. Technol., 9 2 (2000) 161

[61] R. Zorat and D. Vender, J. Phys. D: Appl. Phys., 33 14 (2000) 1728

[62] R. Zorat, *Numerical modelling of low temperature radio-frequency hydrogen plasmas*. PhD thesis, Dublin City University, Ireland (2003)

[63] C. Lee, D. B. Graves, M. A. Lieberman and D. W. Hess, J. Electrochem. Soc., 141 6 (1994) 1547

[64] C. Lee and M. A. Lieberman, J. Vac. Sci. Technol. A, 13 2 (1995) 368

[65] C. Lee, M. A. Lieberman, A. J. Lichtenberg, F. Bose, H. Baltes and R. Patrick, J. Vac. Sci. Technol A, 15 1 (1997) 113

[66] J. P. Boeuf, Phys. Rev. A, 36 6 (1987) 2782

[67] R. A. Stewart, P. Vitello and D. B. Graves, J. Vac. Sci. Technol. B, 12 1 (1994) 478

[68] M. M. Meyyappan and J. P. Kreskovsky, J. Appl. Phys., 68 4 (1990) 1506

[69] D Vender and R W Boswell, IEEE Trans on Plasma Science, 18 4 (1990) 725

[70] C K Birdsall and A B Langdon, Plasma Physics via Computer Simulations, Adam Hilger, Bristol (1991)

[71] R W Hockney and J W Eastwood, Computer Simulation Using Particles Adam Hilger, Bristol (1988)

[72] C K Birdsall, IEEE Trans Plasma Sci , 19 2 (1991) 65

[73] V Vahedi, G DiPeso, C K Birdsall, M A Lieberman and T D Rognlien, Plasma Sources Sci Technol , 2 (1993) 261-272

[74] V Vahedi, C K Birdsall, M A Lieberman, G DiPeso, and T D Rognlien Plasma Sources Sci Technol , 2 (1993) 273-278

[75] V Vahedi and M Surendra, *Comput Phys Commun* , 87 (1995) 179-198

[76] Courtesy of Victor Law

[77] E A G Hamers, W G J H M van Sark, J Bezemer, W J Goedheer, and van der Weg, Int J Mass Spectrom Ion Processes 173 (1998) 91

[78] E A G Hamers, *Plasma deposition of hydrogenated amorphous silicon,* PhD thesis University Utrecht, Netherlands (1998)

[79] D W O Heddle, *Electrostatic Lens Systems,* IOP Publishing (1991)

[80] D A Dahl, J E Delmore, and A D Appelhans, Rev Sci Instrum , 61 (1990) 607

[81] J W Coburn and E Kay, J Vac Sci Technol , 8 (1971) 738

[82] J W Coburn and E Kay, J Appl Phys , 43 (1972) 4965

[83] J Liu, G L Huppert and H H Sawin, J Appl Phys , 68 8 (1990)

[84] J Janes and C Huth, J Vac Sci Technol , 10 6 (1992) 3522

[85] R T C Tsui, Phys Rev , 168 1 (1968) 168

[86] Y Wang and J K Olthoff, J Appl Phys , 85 9 (1999) 6358

[87] M Zeuner, H Neumann and J Meichsner, J Appl Phys , 81 7 (1997) 2985

[88] B E Thompson, K D Allen, A D Richards and H H Sawin, J Appl Phys , 59 6 (1996) 1890

[89] W Schwarzenbach, G, Cunge and J P Booth, J Appl Phys , 85 11 (1999) 7562

[90] R J M M Snijkers, M J M van Sambeek, M B Hoppenbrouwers, G M W Kroessen and F J de Hoog, J Appl Phys , 79 12 (1996) 8982

[91] C M Deegan, J P Goss, D Vender and M B Hopkins, Appl Phys Letts , 74 4 (1999) 1969

[92] C M Deegan, *Characterisation of the heating mechanisms in a capacitively coupled argon rf discharge* PhD Thesis, Dublin City University (1999)

[93] T Gans, V Schulz-von der Gathen, and H F Dobele, Contrib Plasma Phys , 42 (2002) 596

[94] T Gans, V Schulz-von der Gathen, and H F Dobele, Europhys Lett , 66 (2004) 232

[95] M A Lieberman and V A Godyak, IEEE Trans Plasma Sci , 26 (1998) 955

[96] M Surendra and D B Graves, Phys Rev Lett , 66 (1991) 1469

[97] M M Turner, Phys Rev Lett , 75 (1995) 1312

[98] G Gozadinos, M M Turner and D Vender, Phys Rev Lett , 87 (2001) 13

[99] G Gozadinos, D Vender, M M Turner, and M A Lieberman, Plasma Sources Sci Technol , 10 (2001) 117

[100] G Gozadinos, *Collisionless heating and particles dynamics in radio-frequency capacitive plasma sheaths*, PhD thesis, Dublin City University, Ireland (2001)

[101] Balzers Instruments, Postfach 1000 FL-9496 Balzers, Liechtenstein http //www balzers com

[102] T Mosbach, H -M Katsch, and H F Dobele, Phys Rev Lett , 85 (2000) 3420

[103] M B Hopkins and W G Graham, J Appl Phys , 69 6 (1991) 3461

[104] U Fantz, B Heger, Plasma Phys Control Fusion, 40 (1998) 2023